Minimal Models of Quantum Chaotic Many-Body Systems



Amos Chan

University College

University of Oxford

A thesis submitted for the degree of

Doctor of Philosophy in Theoretical Physics

Trinity Term 2019

© Copyright by Amos Chan, 2019.

All rights reserved.

Abstract

Phenomena in quantum chaotic systems such as spectral fluctuations are known to be described remarkably well by the random matrix theory (RMT) in small energy intervals and over large time scales. However, in exchange for analytical tractability, RMT has been constructed to leave out an important element of realistic physical systems – the notion of locality. Since quantum information propagates at a finite speed in a spatially-extended quantum chaotic system, there exists time scales before which RMT is effective. How do we describe the non-equilibrium quantum dynamics at intermediate timescales which are much longer than the local relaxation time but too short for RMT to apply? What are the signatures of many-body quantum chaotic systems beyond the description of RMT? In this thesis, we address these questions by analysing minimal models that incorporate a notion of locality and at the same time retain some analytical tractability of RMT.

More specifically, we study Floquet quantum circuits that are random in space but *periodic* in time. These circuits consist of local and random quantum gates that act on a q-state 'spin' at each site. After a brief review of classical chaos, quantum chaos, and quantum circuits in Chapter 1, we present three main results. In Chapter 2, we formulate a diagrammatical approach for computing ensemble averages of observables over random unitary circuits, and derive exact results on spectral statistics and dynamical observables for a Floquet circuit in the large-q limit. In Chapter 3, we further investigate the spectral statistics in spatially-extended many-body quantum chaotic systems by computing the spectral form factor $K(t)$ analytically and numerically. We show that $K(t)$ follows the RMT description at times longer than the Thouless time t_{Th} and identify the scaling of t_{Th} at the large-q limit of a Floquet circuit. In Chapter 4, we discuss eigenstate correlations for spatially-extended many-body quantum chaotic systems, in terms of the statistical properties of matrix elements of local observables. While the eigenstate thermalization hypothesis (ETH) is known to give an excellent description of these quantities, the phenomenon of scrambling and the butterfly effect imply structure beyond ETH. We determine analytically and verify numerically the universal form of this structure at long distances and small eigenvalue separations for Floquet systems.

Acknowledgements

First and foremost, I would like to thank my supervisor, John Chalker, for mentoring me to become a better physicist. In the past four years, John has been a constant source of deep insights and inspirations; has guided me to approach a problem using ingenious simplifications; has taught me to not lose sight of the big picture; and has been extremely understanding, patient, and generous with his time for me. I am and will always be immensely grateful to John. I am indebted to my collaborator, Andrea De Luca, who is contagiously passionate about physics, resourceful in attacking problems, and always pushing me to challenge myself. I will remember our joyful moments in our offices for years to come. Thank you for being a great mentor and a great friend. I wholeheartedly thank Adam Nahum, Rahul Nankishore, Siddharth Parameswaran, Sthitadhi Roy, Steven Simon, Thorsten Wahl for providing their encouragement, kind words and generous support.

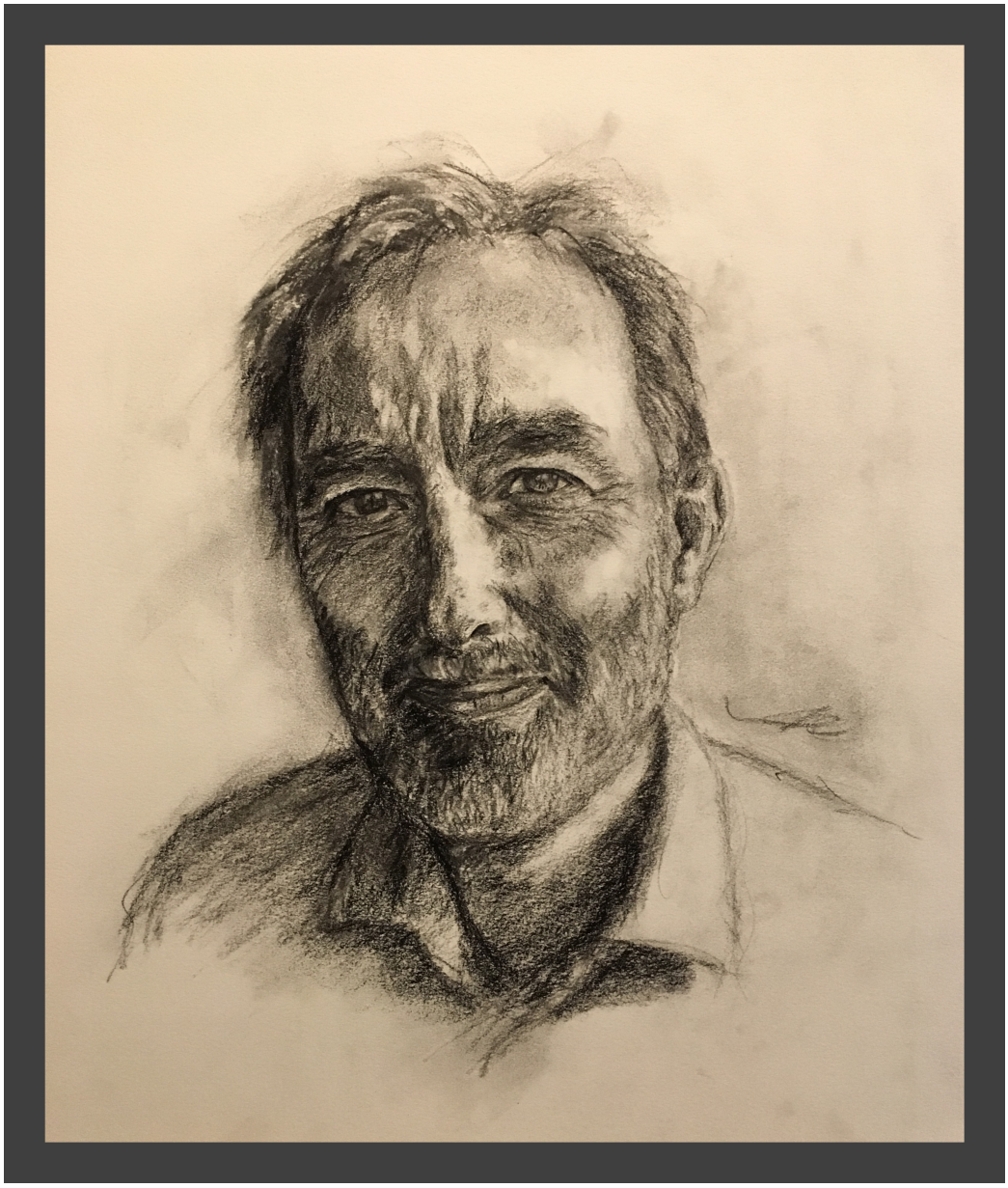
I am especially grateful to my collaborators for their guidance, including Joey Li, Adam Nahum, Rahul Nankishore, Michael Pretko, Sthitadhi Roy, Graeme Smith and Thorsten Wahl. I have also benefited from and am thankful to many of my colleagues in the department, including Tunrayo Adeleke-Larodo, Roberto Bondesan, Callum Brodie, Mario Collura, Michael Hardman, George Johnson, Tianhan Liu and Eric Vernier. I thank Jack Kemp and Abishek Kulshreshtha for being my officemates in Oxford. I give special thanks to Inwook, Wen-Yah, William for being my undergraduate Physics buddies and lifelong friends.

I thank my flatmates Andi, Arseni, Brad, Catherine, Femi and John for giving me a lovely second home in Oxford and for tolerating the smell of chickens daily. I am grateful to the friends I have met at Asylum Welcome, including Anya, Ben, Caritas, Dalí, Helen, Helena, Johnny, Jonny, Nabil, Nicole, Shazia and Trevor, for giving me a strong sense of community in Oxford. I also would like to thank my good friends Anant, Charlotte, Deborah, John, Kenix, Pui San, Shinae, Vicki and Yee Rou, who have always been there to support me. I am truly grateful to Araceli Keelan, who has time and time again offered her help whenever it is needed.

Lastly, I would like to thank Jane and Thomas for being my dearest cousins. I thank Daniel, my parents and grandparents for their unconditional love and support. I am abundantly blessed to be a part of your family.

He giveth more grace when the burdens grow greater.

— Annie Johnson Flint



John Chalker



Andrea De Luca



My parents



My grandmother

To my parents and grandparents.

Contents

Abstract iii

Acknowledgements iv

1 Introduction **1**

1.1 Classical chaos 2

1.1.1 Thermalization in classical systems 2

1.1.2 Classical chaos 4

1.1.3 Integrability 4

1.2 Quantum Chaos 5

1.2.1 Introduction 5

1.2.2 Quantum chaos in microscopic billiards 7

1.2.2.1 Experimental results 7

1.2.2.2 Quantum theory of conductance 7

1.2.3 Random Matrix Theory 9

1.2.3.1 Introduction 9

1.2.3.2 Coulomb gas 11

1.2.3.3 Wigner's surmise 12

1.2.4 Spectral statistics 13

1.2.4.1 Nearest neighbouring level spacing 14

1.2.4.2 Spectral form factor 15

1.2.5 Eigenstate thermalization hypothesis 17

1.2.5.1 Thermalization in quantum systems 17
1.2.5.2 Statement of the hypothesis 19
1.2.6 Operator spreading 20
1.2.6.1 Lieb-Robinson Bound 20
1.2.6.2 Out-of-time-order commutator 21
1.2.7 Entanglement entropy 22
1.3 Quantum circuits 24
1.3.1 Random unitary circuits 26
1.3.2 Floquet random unitary circuits 27
1.4 Summary of results 29

2 Solution of a minimal model of many-body quantum chaotic systems 31

2.1 Introduction 31
2.2 Summary of results 32
2.2.1 Spectral form factor 33
2.2.2 Dynamics 34
2.2.2.1 Local relaxation 34
2.2.2.2 Entanglement spreading 35
2.2.2.3 Out-of-time-order correlator 36
2.3 Ensemble averaging 37
2.4 Diagrammatic evaluation of results 42
2.4.1 Spectral form factor 43
2.4.2 Relaxation of local observables 44
2.4.3 Purity and Rényi entropies 45
2.4.4 Out-of-time-order correlator 48
2.5 Discussion and outlook 48

3 Spectral statistics of quantum chaotic many-body systems 52

3.1 Introduction 52

3.2 Mapping to the classical Potts model 54

3.3 Numerical results 57

3.4 Discussion and outlook 60

4 Eigenstate correlation, thermalization and the butterfly effect 63

4.1 Introduction 63

4.2 ETH and relaxation 64

4.3 Generic form of four-point correlators 66

4.4 Numerical results 68

4.5 Discussion and outlook 72

5 Summary and outlook 76

A Appendices of Chapter 2 79

A.1 Recursive formula for $V_{c_1,c_2,\ldots,c_u}$ 79

A.2 Enumeration of leading order diagrams 79

A.2.1 Method of contraction-addition 80

A.2.2 Domain wall approach 82

A.3 Spectral form factor 85

A.4 Relaxation of local observables 86

A.5 2nd Rényi entropy 87

A.5.1 Block representation of quantum purity 87

A.5.2 Evaluation of quantum purity 89

A.6 3rd and higher Rényi Entropies 91

A.7 Evaluation for OTOC 93

B Appendices of Chapter 3 **96**

B.1 Spectral form factor for the Floquet random unitary circuit. 96

B.2 Numerical results for $K(t)$ and $\langle r \rangle$ for the many-body localized phase at $q = 2$ 96

C Appendices of Chapter 4 **99**

C.1 Computation of $G(\omega_1, \omega_2, \omega_3)$ under the standard hypothesis of ETH for the matrix elements of $\hat{X}$ and $\hat{Y}$ 99

C.2 Factorization of $G(\omega_1, \omega_2, \omega_3)$ 100

Chapter 1

Introduction

One of the fundamental problems in quantum statistical mechanics is to understand how an isolated many-body quantum system evolves towards equilibrium under unitary time evolution. Consider the quantum quench protocol, where a quantum many-body system is initialized as the ground state of an initial Hamiltonian H_i, and evolves unitarily in time with a final Hamiltonian H_f after a sudden change of the parameters of H_i [**?**, **?**, **?**]. A system thermalizes strongly (weakly) if (the long-time average of) the expectation value of an local observable agrees with the microcanonical expectation value at late time. That is to say that every sufficiently small subsystem is effectively in the thermal Gibbs state at late time [**?**, **?**, **?**]. Because such thermal states are specified completely by the values of a handful of conserved quantities like the total energy, we say that a system 'forgets' the memory of the initial state as it thermalizes. Why and how does thermalization occur? This is the central question of this thesis. Importantly, such a question is not merely theoretical. Recent advances in experiments, e.g. ultracold atomic gases in optical lattices, have provided highly-tunable, well-isolated quantum systems to study non-equilibrium quantum dynamics [**?**]. In this chapter, we review some basic concepts in classical and quantum chaos, and introduce our minimal models of spatially-extended

quantum chaotic many-body systems. In Sec. 1.1, we describe thermalization and ergodicity in classical systems, classical chaos and integrability. In Sec. 1.2, we discuss how certain quantum mechanical phenomena, like the conductance fluctuations in microscopic billiards, can be described with the dynamics of classical chaotic systems using the semi-classical approximation. After a brief review of the random matrix theory, we focus on several signatures of quantum chaos in spectral statistics, eigenstate correlations, operator spreading and entanglement entropy growth. In Sec. 1.3, we introduce a specific class of quantum circuits called random unitary circuits, which are discrete time unitary evolution operators consisting of random and local quantum gates. We argue that they are powerful models to investigate non-equilibrium quantum dyanmics, because they incorporate a notion of locality and retain some of the analytical tractability from the random matrix theory. Finally, in Sec. 1.4, we summarise the results of of this thesis, which are based on [**?**, **?**, **?**]. The exposition below largely follows [**?**, **?**, **?**, **?**, **?**, **?**, **?**, **?**, **?**].

1.1 Classical chaos

1.1.1 Thermalization in classical systems

Why can an equilibrated classical system of 10^{23} particles be described by thermodynamics with just a few macroscopic variables? How does such a system equilibrate and forget its initial state? To phrase the question more concretely, consider a system of N particles parametrised with positions $\{x_1, \ldots, x_N\}$ and momenta $\{p_1, \ldots, p_N\}$. The state of the system can then be specified as a point $\Gamma = \{x_1, \ldots, x_N, p_1, \ldots p_N\}$ in a $2N$-dimensional space known as the phase space. Statistical mechanics relies on the assumption that the time average $\langle O \rangle_t$ of an

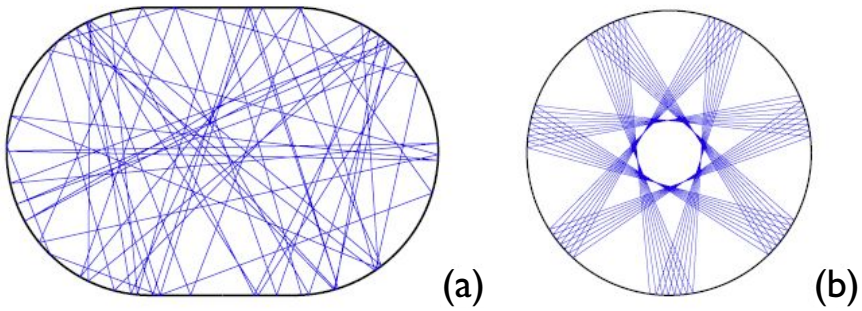


Figure 1.1: Trajectories of a particle in (a) a chaotic Bunimovich stadium and (b) an integrable circular stadium. Figures taken from [**?**].

observable O can be computed as an average over the microcanonical ensemble, i.e.

$$\langle O \rangle_t = \frac{\int_S d\Gamma \, O(\Gamma)}{\int_S d\Gamma} \, , \tag{1.1}$$

where the integral is integrated over a surface S of constant energy, and the right hand side depends solely on the system's energy[1]. In this context, our initial question concerning thermalization becomes the question of why Eq. (1.1) holds.

The above question is often answered with the ergodic hypothesis, which says that, over a long period of time, the time spent by the system in some region of the phase space is proportional to the volume of this region, i.e. all accessible points in phase space are equally probable over a long period of time. For an ergodic system, since the path, along which the time average $\langle O \rangle_t$ is integrated, covers the entire subregion S in the phase space, $\langle O \rangle_t$ is equal to the ensemble average over S in the phase space. In other words, (1.1) holds if the system is ergodic. The ergodic hypothesis is proven rigorously for a few systems, including the Sinai Billiards [**?**, **?**, **?**] (a particle in square cavity with circular potential barriers in the centre) and the Bunimovich Stadium [**?**] (a particle in a cavity with a geometry illustrated in Fig. 1.1a).

[1]If other macroscopic variables are conserved, the surface S needs to be modified to take account of these constraints accordingly.

1.1.2 Classical chaos

A concept closely related to thermalization is chaos. A system is chaotic if the system exhibits strong sensitivity to its initial condition, known as the butterfly effect: Two slightly different initial states quickly diverge under time evolution. For concreteness, suppose we have a single particle system evolving in time t with position coordinate $x(t)$. The butterfly effect can be characterized as the derivative of the system's trajectory $x(t)$ with respect to its initial condition x_0,

$$\left|\frac{\partial x(t)}{\partial x_0}\right| \sim e^{\lambda t}\,, \tag{1.2}$$

where $\lambda > 0$ is called the Lyapunov exponent, and is used to characterise the rate of diveregence. An example of a classical chaotic system is the Bunimovich Stadium in Fig. 1.1a. It is apparent that a generic trajectory of a single particle covers the entire stadium. Furthermore, two close-by trajectories diverge exponentially, and become uncorrelated after a few bounces against the walls.

Although classical thermalization and chaos are not exactly equivalent, when the number of degrees of freedom of a given system is large, we expect the system to be ergodic if and only if it is chaotic. Since we will always be dealing with a large number of degrees of freedom, we will not focus on the distinctions between the two notions, and we will assume that they are synonymous.

1.1.3 Integrability

Thermalization and chaotic behaviours are generic in physical systems, except for special classes of systems including the integrable systems. A system with N degrees of freedom is called integrable if there exists at least N independent conserved quantities. An example of a classical integrable system is a single particle traversing a circular stadium as in Fig. 1.1b. This system has two degrees of freedom, the

particle's horizontal and vertical positions, and also two conserved quantities, the energy and the angular momentum. It is apparent that a generic trajectory forms a clear pattern, and its long time average does not cover the entire stadium. The distance between two close-by trajectories increase merely linearly in time. A many-body system is often considered chaotic and thermalizing if it does not have an extensive number of conserved quantities. In the next section, we will explore the quantum analogue of these concepts and discuss the existing diagnostics for quantum chaotic and integrable systems.

1.2 Quantum Chaos

1.2.1 Introduction

It is difficult to apply the classical definition of chaos to quantum systems. Although an effective phase space can be constructed in quantum mechanics (e.g. the Wigner-Weyl quantization [**?**]), the notion of trajectories is not well-defined, since the positions and momenta of particles cannot be simultaneously defined due to the uncertainty principle. To circumvent this problem, one may attempt to generalize the butterfly effect by looking for a vanishing overlap between the time-evolved initial state $|\psi(t)\rangle$ and a time-evolved perturbed state $|\psi'(t)\rangle$. However, unitarity of time evolution operator guarantees that the overlap remains constant in time, since $\langle\psi'|\, U^\dagger(t)U(t)\,|\psi\rangle = \langle\psi'|\psi\rangle$. So the overlap between time-evolved quantum states also cannot characterize quantum chaos. Instead, signatures of quantum chaos can be found in transport properties, spectral statistics, eigenstate correlations, entanglement entropy growth, operator spreading etc., which will be the subjects of the rest of this chapter.

Before reviewing the signatures of quantum chaotic systems, it is important to mention another possible outcome of time evolution of generic many-body quantum

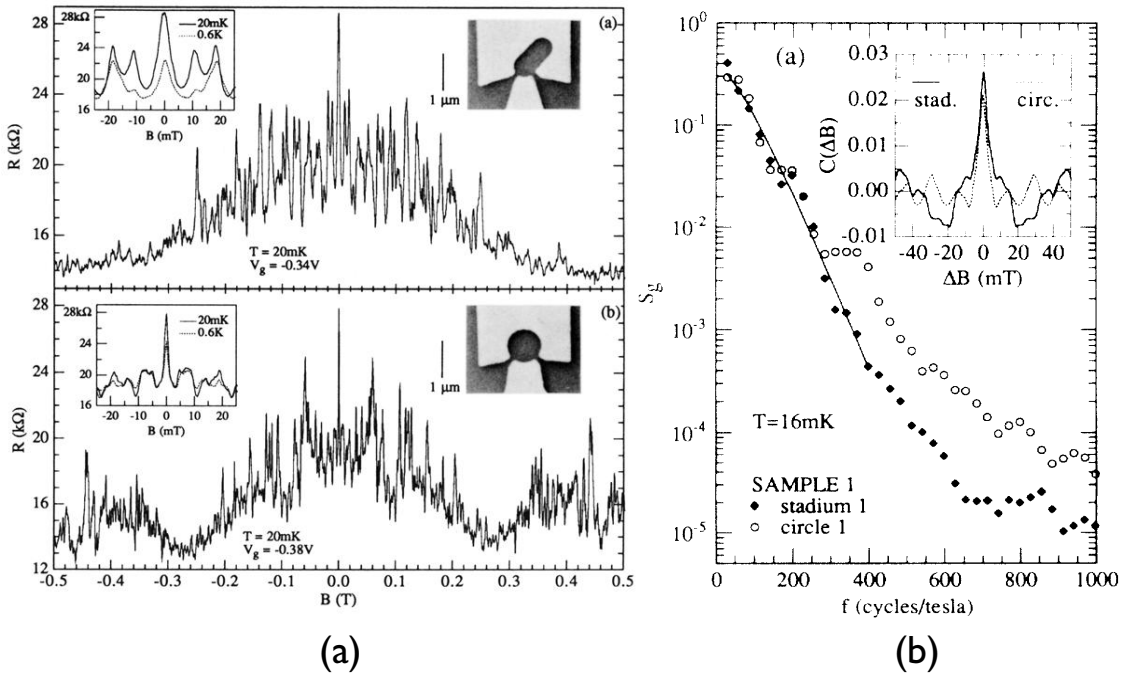


Figure 1.2: (a): [?] studied two quantum dots with geometries specified in the right inset of (a). The main panel shows the resistence R against the strength of the magnetic field B. The left inset shows the behaviour of R close to $B = 0$. (b): The inset shows the autocorrelation $C(\Delta B)$ against ΔB, and the main panel shows the power spectra S_g against the frequency f, the empty (filled) circle corresponds to the circular (Bunimovich stadium) geometry. There are clear differences between the behaviour of S_g of the two quantum dots for frequency above 250 cycles per tesla.

systems, namely many-body localization (MBL). MBL systems display localization and avoid thermalization due to strong quenched disorder, which makes energy exchange processes between different parts of the system "off-resonant" [?, ?]. A desciption of MBL systems explaining their dynamical properties has been formulated using an extensive number of emergent quasi-local integrals of motion [?, ?], which bear a resemblence to concepts in integrability. In this thesis, we will contrast the signatures of quantum chaotic systems and MBL systems, but we will not focus on the details of MBL. We refer interested readers to [?, ?] for further details of MBL.

1.2.2 Quantum chaos in microscopic billiards

1.2.2.1 Experimental results

In this section, we explain how certain phenomena in quantum chaotic systems can be described by the dynamics of classical chaotic billiards using the semi-classical approximation. Experimental advances have allowed a microscopic quantum billiard to be realized as a quantum dot, where a two-dimensional electron gas is confined in a submicron planar area,so that the motions of electrons are ballistic (rather than diffusive). In [**?**], the authors experimentally studied two quantum dots with the Bunimovich stadium and circular geometries, as shown in the right insets of Fig. 1.2a (c.f. Fig. 1.1). The resistance R is plotted against the strength of the perpendicular magnetic field B in Fig. 1.2a. To investigate the strong oscillations of R in B, the authors investigate the fluctuations in conductance $g = 1/R$ around its mean in Fig. 1.2b inset, by considering the autocorrelation function

$$C(\Delta B) \equiv \langle \delta g(B + \Delta B) \delta g(B) \rangle_B \,, \tag{1.3}$$

where $\langle \dots \rangle_B$ denotes an average over B, and $\delta g(B) \equiv g(B) - \langle g \rangle_B$. The Fourier transform of $C(\Delta B)$, called the power spectrum S_g, is plotted in Fig. 1.2b, and the plot shows two distinct types of behaviour, which is determined by whether the corresponding classical billiard with the quantum dot geometry is chaotic.

1.2.2.2 Quantum theory of conductance

Why can the quantum mechanical phenomenon of conductance fluctuations in quantum dots be explained by classical billiard dynamics? To answer this question, recall that the conductance g is determined by the transition rate of an electron travelling through the quantum dot from lead 1 to lead 2 (Fig. 1.3), as described by

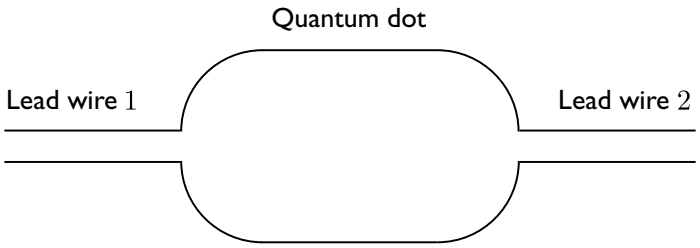


Figure 1.3: An illustration of a quantum dot in the geometry of a Bunimovich stadium with two lead wires .

the Landauer formula [**?**]

$$g = \frac{2e^2}{h} \sum_{m,n} |t_{mn}|^2 \qquad \text{with} \qquad t_{mn} \approx \sum_{\gamma(m,n)} w_\gamma \exp\left(\frac{i}{\hbar} S_\gamma\right) , \tag{1.4}$$

with electronic charge e and Planck constant h. t_{mn} is the transmission amplitude from an incident electron in mode m in lead 1 to an outgoing electron in mode n in lead 2. γ labels a path, and w_γ is a factor that characterizes how the path γ deviates from its original one if there is a small change to the initial condition. The Feynman's path integral approach allows t_{mn} to be expressed as a sum of exponential factors over inifinite number of possible paths $\gamma(n, m)$. After a substitution of Eq. (1.4) into Eq. (1.3), $C(\Delta B)$ becomes a sum over the phase [**?**],

$$\exp\left\{\frac{i}{\hbar}\left[S_a(B+\Delta B) - S_b(B+\Delta B) + S_c(B) - S_d(B)\right]\right\} , \tag{1.5}$$

where the paths $\{a, b, c, d\}$ satisfy the constraints $a \neq b$ and $c \neq d$ because the mean value of the conductance has been removed in Eq. (1.3). In the semi-classical limit where $\hbar \to 0$, the exponent is highly oscillating, and $C(\Delta B)$ is dominated by the terms where path a is identical to path d, and where path b is identical to path c. Due to the change in magnetic field ΔB, the phase differences in Eq. (1.5) will induce a phase factor proportional to the area enclosed by trajectories $a = d$ and $b = c$

according to

$$S_\gamma(B + \Delta B) - S_\gamma(B) = \frac{\hbar \Delta B}{\Phi_0} \Theta_\gamma \ , \tag{1.6}$$

where $\Phi_0 \equiv hc/e$ is the flux quantum and Θ_γ is the area enclosed by the trajectory γ. It turns out that the power spectrum S_g of conductance fluctuations can be written as a convolution of the distribution of the area Θ enclosed by an incident trajectory in the quantum dot. For chaotic classical billiards, the area distribution of $P(\Theta) \propto \exp(-|\Theta|)$ can be shown to be decaying exponentially. In summary, by using the semi-classical approximation, we have related the quantum mechanical phenomenon of conductance fluctuations to the dynamics of classical billiards.

1.2.3 Random Matrix Theory

1.2.3.1 Introduction

To understand the dynamics of a generic quantum system, we need information about its highly-excited states, which is notoriously difficult to compute. Wigner's idea was that, instead of computing the exact energy levels of a single physical system, one should compute the spectral statistics of many such systems [**?**]. Furthermore, suppose one looks at a narrow energy window of a system's spectrum such that the density of states is constant, the Hamiltonian in a *non-fine-tuned* basis looks like a random matrix. These ideas lead to the study of the random matrix theory (RMT), which was first developed by Wishart [**?**], Wigner [**?**, **?**, **?**], Dyson [**?**] and many others [**?**]. Historically, RMT has a wide range of applications, including in the energy levels of heavy nuclei [**?**], the theory of small metal particles [**?**], chaotic systems [**?**, **?**], and of universal conductance fluctuation in disordered conductors [**?**, **?**].

Wigner and Dyson studied a random matrix ensemble of $N \times N$ Hermitian matrices H defined by a probability distribution of the form

$$P(H) \propto \exp[-\beta \text{ Tr } V(H)] \,, \tag{1.7}$$

where $V(H)$ is some function of matrix H and β is a constant. The ensemble is called Gaussian if $V(H) \propto H^2$. A Gaussian ensemble is chosen such that the ensemble is invariant under the rotation of basis, and has independently-distributed matrix elements [**?**, **?**].

For the Gaussian ensembles, there are three universality classes known as the Gaussian Unitary Ensemble (GUE), Gaussian Orthogonal Ensemble (GOE) and Gaussian Symplectic Ensemble (GSE) [**?**]. Respectively, these ensembles have real, complex and real quaternion matrix elements, and are invariant under the transformation $H \rightarrow UHU^{-1}$, where U are orthogonal, unitary and symplectic matrices. Physically, GUE describes systems with broken time-reversal symmetry, e.g. in the presence of an external magnetic field or magnetic impurities. GOE describes time-reversal invariant systems of particles with integer spin. GSE describes time-reversal invariant systems of particles with half odd integer spin, e.g. spin systems with spin-orbit interaction. For reasons that will become clear in Sec. 1.2.3.2, it is convenient to label these three ensembles by $\beta = 1, 2$ and 4 respectively. Each ensemble has a bounded spectrum and a density of states with a semi-circle shape [**?**]. As a consequence, the mean values of observables computed in these ensembles are not physical. However, their fluctuations can be shown to be independent of the global forms of the spectra, and are used to model experimental data with great success [**?**, **?**, **?**, **?**].

Dyson introduced three additional ensembles called the circular unitary ensemble (CUE), circular orthogonal ensemble (CUE) and the circular symplectic ensemble

(CSE). These ensembles contain unitary matrices rather than Hermitian matrices in the Gaussian ensembles, and they are invariant under the corresponding symmetry transformations to their Gaussian analogues. Due to unitarity, the eigenphase spectrum of a circular ensemble lives in a unit circle in the complex plane. These ensembles have flat densities of states, and are also shown to have the same local fluctuations as their Gaussian analogues. Unitary ensembles are central to the construction of physically interesting yet analytical solvable models of quantum chaos [**?**, **?**, **?**], which we will discuss in details in Sec. 1.3. In this thesis, we will focus mainly on CUE.

1.2.3.2 Coulomb gas

Here we write the probability distribution $P(H)$ in terms of its eigenvalues and eigenvectors [**?**]. Let $\{E_n\}$ and U be the set of eigenvalues and the unitary matrix of eigenvectors, so that $H = U\,\mathrm{Diag}(E_1, E_2, \dots)\,U^\dagger$. Using the cyclicity of the trace, we have $P(H) \propto \prod_n \exp[-\beta\ V(E_n)]$. In other words, the distribution Eq. (1.7) is independent of the eigenvectors, due to its invariance under rotation of basis. The corresponding measure includes a Jacobian J that only depends on the eigenvalues [**?**],

$$d\mu(H) = J(\{E_n\})\ d\mu(U) \prod_i dE_i, \qquad J(\{E_n\}) = \prod_{i<j} |E_i - E_j|^\beta\,, \tag{1.8}$$

where $\beta = 1, 2, 4$ for the three Gaussian ensembles introduced in Sec. 1.2.3.1. The probability distribution $P(\{E_n\})$ of the eigenvalues is then

$$P(\{E_n\}) \propto \prod_{i<j} |E_i - E_j|^\beta \prod_k \exp[-\beta V(E_k)]\,. \tag{1.9}$$

This probability distribution can be written in the form [**?**, **?**]

$$P(\{E_n\}) \propto \exp(-\beta\,\mathcal{H}), \qquad \mathcal{H} = -\sum_{i<j} \ln|E_i - E_j| + \sum_i V(E_i)\,, \tag{1.10}$$

which is a partition function of classical particles with logarithmic pair potential and a confinement potential $V(E_k)$. For the Gaussian ensembles, the confinement potential $V(E_i) \propto \sum_i E_i^2$ is a harmonic potential. The above form of partition function holds as long as the ensembles' invariance under rotation of basis is preserved. The microscopic details of the ensemble enter via $V(E_i)$ and do not affect correlation between the eigenvalues as classical particles on scales much smaller than the width of the density of states. Therefore, RMT is universal in the sense that correlation between eigenvalues at the scale of mean level spacing is independent of the microscopic details of the ensemble.

1.2.3.3 Wigner's surmise

The statistics of energy levels in RMT, known as the Wigner-Dyson statistics, can be illustrated using an ensemble of 2×2 Hamiltonians with Gaussian-distributed random entries [?, ?, ?, ?, ?].

$$H = \begin{bmatrix} \epsilon_1 & V/\sqrt{2} \\ V^*/\sqrt{2} & \epsilon_2 \end{bmatrix} . \tag{1.11}$$

For simplicity, we can consider the GOE for time-reversal systems, where $V = V^*$ is real. The energy levels of the two-level systems are obtained by diagonalization as

$$E_{1,2} = \frac{1}{2}\left(\epsilon_1 + \epsilon_2 \pm \sqrt{(\epsilon_1 - \epsilon_2)^2 + 2|V|^2}\right) . \tag{1.12}$$

The level statistics can be probed by computing $P(\omega = E_1 - E_2)$,

$$P(\omega) = \frac{1}{(2\pi)^{3/2}\sigma^3} \int d\epsilon_1 d\epsilon_2 dV \, \delta\left(\sqrt{(\epsilon_1 - \epsilon_2)^2 + 2V^2} - \omega\right) \exp\left(-\frac{\epsilon_1^2 + \epsilon_2^2 + V^2}{2\sigma^2}\right) . \tag{1.13}$$

After the change of variable $\epsilon_2 = \epsilon_1 + \sqrt{2}\xi$, we can integrate over ϵ_1. Furthermore, we can evaluate the rest of the integrals using cylindrical coordinates with $V =$

$r\cos\theta,\ \xi = r\sin\theta$, and obtain

$$P(\omega) = \frac{\omega}{2\sigma^2}\exp\left(-\frac{\omega^2}{4\sigma^2}\right) . \tag{1.14}$$

This result can be generalized to other ensembles as

$$P(\omega) = a_\beta\,\omega^\beta \exp\left(-b_\beta\,\omega^2\right) . \tag{1.15}$$

where a_β and b_β are obtained by normalizing $P(\omega)$ and fixing the mean level spacing. This result shows that there is a β-dependent level repulsion since $P(\omega) \to 0$ as $\omega \to 0$, and that there is a Gaussian falloff at large ω. For general $N \times N$ Gaussian ensembles, the level statistics $P(\omega)$ do not have a closed analytical form, but they are qualitatively described by the Wigner Surmise in Eq. (1.15).

1.2.4 Spectral statistics

One of the long-standing diagnostics of quantum chaos is to compute the spectral statistics of a given system. Bohigas, Giannoni and Schmit (BGS) considered a single particle in an infinite two-dimensional potential well in the setting of a Sinai billiard [**?**]. In a sufficiently narrow energy window at high energy, they found that the spectral fluctuation properties of the system exhibit the Wigner-Dyson distribution of the GOE. Generalizing this observation, they propose the BGS conjecture: a quantum system whose corresponding classical analogue is chaotic, has level statistics described by RMT. This conjecture makes an important connection between quantum chaos and RMT, and extends Wigner's intuition that, in a non-fine-tuned basis in a small energy window, the Hamiltonian of a generic complex system looks essentially like a random matrix.

On the other hand, Berry and Tabor [**?**] conjecture that quantum systems, whose corresponding classical analogue is integrable, have energy eigenvalues that behave

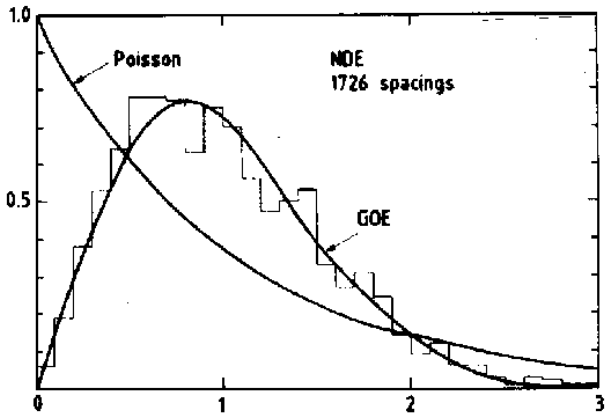


Figure 1.4: The distribution of nearest neighbouring level spacing (normalized with the mean level spacing) of nuclear energy levels [**?**]. The two solid lines are the corresponding distributions for a spectrum that exhibits Poisson statistics and for a spectrum of GOE.

like a sequence of independent random variables, which obey the Poisson statistics. The intuition is that, at high energy, nearby energy levels are effectively uncorrelated and their corresponding eigenstates have sets of conserved quantities with different values. In the following subsections, we will introduce two quantities that to probe the level statistics of a given system.

1.2.4.1 Nearest neighbouring level spacing

Given a quantum chaotic system, one can compute its energy levels and the gaps between nearest neighbouring levels. Far from the edges of the spectrum, the distribution of these gaps[2] coincides with the Wigner-Dyson distribution obtained from RMT (e.g. Fig. 1.4). In particular, the distribution exhibits the phenomenon of level repulsion: no nearest neighbouring levels have zero gap. The Wigner-Dyson distribution does not have a closed form but it is well approximated by the Wigner surmise in Eq. (1.15). Examples of chaotic systems which exhibit the Wigner-Dyson distribution include heavy nuclei [**?**], a single particle in a cavity [**?**], a hydrogen atom

[2]Additionally, in order to remove the distirbution's dependence on the local level density, the eigenlevels have to be "unfolded" (using a cumulative distribution function) such that the level density of the unfolded eigenlevels is flat by construction.

in a magnetic field [?] and various lattice models [?, ?, ?]. For quantum integrable and MBL systems, the levels in the middle of the spectrum are uncorrelated and distributed according the Poisson distribution. The probability of finding energy gap of size ω is

$$P_{\text{int}}(\omega) \propto \exp(-c\,\omega) \ , \tag{1.16}$$

for some constant c. Note that there is a finite probability density of finding two neighbouring levels with zero gap. It is also useful to represent these distributions of level spacings $\{\delta_n \equiv E_{n+1} - E_n\}$ with a single parameter, r, defined as the average of

$$r_n = \frac{\min\{\delta_n, \delta_{n+1}\}}{\max\{\delta_n, \delta_{n+1}\}} \ , \tag{1.17}$$

over n which labels each pair of nearest neighbouring levels in the spectrum [?]. For a spectrum that exhibits Poisson statistics, $r = 2\ln 2 - 1 \approx 0.386$, while for a random matrix ensemble, say, GUE or CUE, we have $r \approx 0.603$.

1.2.4.2 Spectral form factor

Although the distribution of nearest neighbouring level spacings is an important diagnostic of quantum chaos, it only probes the scale of the mean level spacing which, for a many-body system, is exponentially small in the system's size, and therefore it only probes an exponentially long time scale. This provides one reason to introduce the spectral form factor (SFF). Suppose $\rho(E)$ is the density of energy levels of a given system at energy E. Consider the two-level correlation function $R(E, \omega) = \langle \rho(E)\rho(E+\omega) \rangle$, which is the probability of finding two levels at energies E and $E + \omega$. The Fourier transform of the two-level correlation function is known as the SFF,

$$K(t) = \sum_{i,j} \left\langle e^{i(E_i - E_j)t} \right\rangle \ , \tag{1.18}$$

where E_i is the (quasi-)energy of the i-th eigenstate of the (time-periodic) system, and $\langle\cdot\rangle$ is either the average over an ensemble or over multiple time intervals[3].

To orient ourselves, we will review some results on the SFF for quantum chaotic and integrable systems. Since this thesis will focus on quantum chaotic models that are Floquet (that is, time-periodic) and without symmetries, the following discussion will focus on the corresponding ensemble of random matrices, the CUE. The SFF averaged over the CUE for integer t is[4]

$$K(t)_{\text{CUE}} = \begin{cases} N^2 & \text{for } t = 0 \\ t & \text{for } t < t_{\text{H}} \text{ and } t \neq 0 \\ N & \text{for } t \geq t_{\text{H}} \end{cases}, \tag{1.19}$$

where N is the Hilbert space size and also the size of the random matrices in the CUE. $t_{\text{H}} = N$ is the Heisenberg time. For $t < t_{\text{H}}$, $K(t)$ increases linearly in t. For $t \geq t_{\text{H}}$, the summand becomes δ_{ij} since $E_i - E_j$ is of the order $\mathcal{O}(\Delta = 2\pi/N)$, and so off-diagonal terms average to zero. For quantum integrable and MBL systems, the energy levels in the middle of the spectrum are distributed according to the Poisson distribution (i.e. uncorrelated), so the summand is δ_{ij} in (1.18) for all $t \neq 0$. Therefore, we have

$$K(t)_{\text{int}} = \begin{cases} N^2 & \text{for } t = 0 \\ N & \text{for } t \neq 0 \end{cases}. \tag{1.20}$$

Not only does the SFF probe time scales beyond the inverse of mean level spacing, it also provides a stark contrast between the quantum chaotic and integrable systems as demonstrated above. Since we only need to sum over two sets of eigenvalues in Eq. (1.18), SFF is also arguably an easier observable to compute than the eigenstate

[3]SFF is defined with an average because $\sum_{ij} e^{i(E_i - E_j)t}$ is not self-averaging [**?**]

[4]One would obtain a qualitatively similar result for the SFF averaged over the GUE if one replaces semi-circle law with a flat density of states.

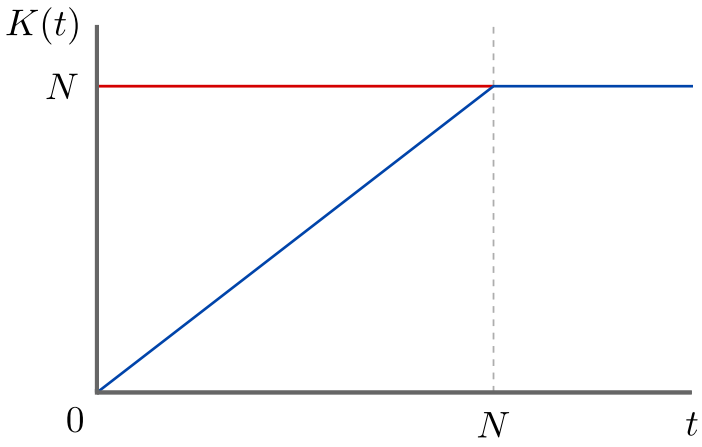


Figure 1.5: Schematic plot of $K(t)$ vs t for a quantum chaotic system, which is modelled by the CUE in RMT (blue) and for a quantum integrable system, which has a spectrum that exhibits the Poisson statistics (red).

correlations, the out-of-time-order commutator and the entanglement entropy, which will be reviewed next.

1.2.5 Eigenstate thermalization hypothesis

1.2.5.1 Thermalization in quantum systems

We begin by setting out the question concerning thermalization in quantum systems, i.e. concerning the validity of the quantum analogue of Eq. (1.1). Consider a Hamiltonian $\hat{H}$ describing an isolated quantum system with eigenstates $|i\rangle$ and eigenvalues E_i, so that $\hat{H}\,|i\rangle = E_i\,|i\rangle$. An initial state $|\psi_I\rangle = \sum_i c_i\,|i\rangle$ evolves in time as $|\psi(t)\rangle = \sum_i c_i\,e^{-iE_it}\,|i\rangle$, where $c_i = \langle i|\psi_I\rangle$. The long-time average of an observable $\hat{O}$ is

$$\langle O(t)\rangle_t \equiv \langle\langle\psi(t)|\,\hat{O}\,|\psi(t)\rangle\rangle_t = \left\langle \sum_{i,j} c_i^* c_j e^{i(E_i-E_j)t} O_{ij} \right\rangle_t = \sum_i |c_i|^2 O_{ii}\,, \tag{1.21}$$

where the $i \neq j$ off-diagonal terms in the sum vanish as long as there is no degeneracy. On the other hand, the observable $\hat{O}$ averaged over the microcanonical ensemble is

$$\langle O \rangle_{\text{micro},E} = \frac{1}{\mathcal{N}} \sum_{E' \in [E, E+\Delta E]} \langle E' | \hat{O} | E' \rangle \ , \tag{1.22}$$

where $\mathcal{N}$ is the number of eigenvalues in the window of $[E, E + \Delta E]$, and ΔE is chosen such that there are exponentially large number of states within the energy window. We say that the quantum system (weakly) thermalizes if

$$\langle O(t) \rangle_t \approx \langle O \rangle_{\text{micro},E} \ , \tag{1.23}$$

and that the system strongly thermalizes if

$$O(t) \approx \langle O \rangle_{\text{micro},E} \qquad t > t_{\text{R}} \ . \tag{1.24}$$

That is, if the expectation value of $\hat{O}$ is close to the one given by the microcanonical ensemble at any time after a relaxation time t_{R}[5]. We ask under what circumstances Eq. (1.23) and (1.24) are true. It turns out that Eq. (1.24) and therefore Eq. (1.23) hold for systems that satisfy the eigenstate thermalization hypothesis (ETH) [**?**, **?**, **?**]. Loosely speaking, ETH states that all eigenstates of the system are equilibrium thermal states, i.e. the averages computed in single eigenstates coincide with the averages computed in a system that is in contact with a heat bath. One way to interpret such a scenario is that a subregion of the isolated system can be considered to be a subsystem, while the complementary system behaves like a heat bath. If different parts of the system exchange energy efficiently, states with spatially inhomogenous energy density can evolve towards thermal states with uniform energy density.

[5]The relaxation time is the time it takes for an observable to reach the microcanonical ensemble result. This time scale generally depends on the initial state, the observable and the microscopic details of the Hamiltonian.

1.2.5.2 Statement of the hypothesis

Consider a system described by a Hamiltonian $\hat{H}$ with eigenstates $|i\rangle$ and eigenvalues E_i, such that $\hat{H}\,|i\rangle = E_i\,|i\rangle$. Formally, ETH states that the matrix elements of observables $\hat{O}$ in the basis of eigenstates are

$$O_{ij} = \langle O\rangle_{\mathrm{micro},\bar{E}}\,\delta_{ij} + e^{-S(\bar{E})/2} f_O(\bar{E},\omega)\,R_{ij}\,, \tag{1.25}$$

where $O_{ij} \equiv \langle i|\hat{O}|j\rangle$; $\bar{E} \equiv (E_i + E_j)/2$; $\omega \equiv E_i - E_j$; $S(E)$ is the thermodynamic entropy at energy E; $f_O(\bar{E},\omega)$ is a smooth function on $\bar{E}$ and ω; and R_{ij} is a random variable with zero mean and unit variance. While there is not a complete understanding of the set of observables which satisfies ETH for a thermalizing system, ETH has been numerically verified for n-body observables with $n \ll L$ for several one-dimensional lattice models of size L. Furthermore, it has been argued that ETH holds for observables with supports up to half the system size[**?**]. Numerical evidences have been reported in models of hard-core bosons and interacting spin chains [**?**, **?**, **?**], spinful and spinless fermions [**?**, **?**], soft-core bosons [**?**, **?**, **?**] and the traverse field Ising model in two dimensions [**?**].

We will focus on two consequences of ETH. Firstly, as long as the energy fluctuation

$$\delta E = \sqrt{\langle\psi_I|\,\hat{H}^2\,|\psi_I\rangle - \langle\psi_I|\,\hat{H}\,|\psi_I\rangle^2} \tag{1.26}$$

is sub-extensive (which is generally expected for local Hamiltonian), Eq. (1.23) holds, regardless of the distribution of c_i. This is because one can perturbatively expand O_{ii} in Eq. 1.21 around $\langle O\rangle_{\mathrm{micro},\bar{E}}$ with the deviation controlled by δE. Secondly, ETH implies the strong thermalization, Eq. 1.24, because the fluctuation of the expectation value of $\hat{O}$ over time, $\sigma_O^2 = \langle O(t)^2\rangle_t - \langle O(t)\rangle_t^2$, is bounded by the absolute magnitude of the observable's off-diagonal entries, i.e. $\exp[-S(\bar{E})]$.

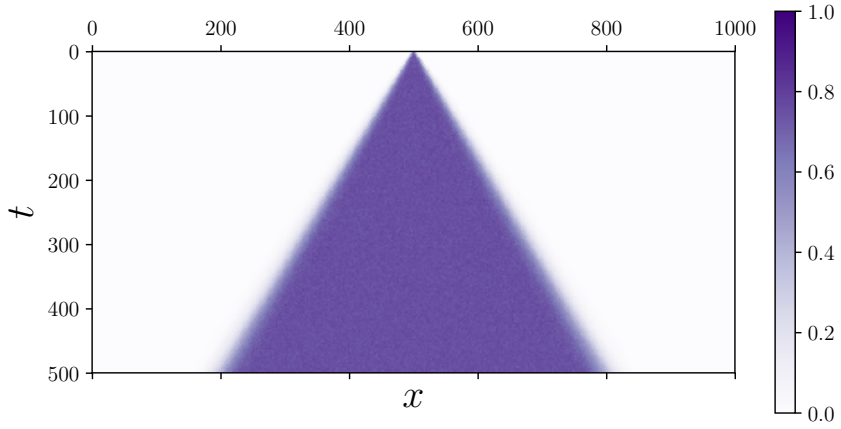


Figure 1.6: The out-of-time-order commutator computed for the one-dimensional random unitary circuits defined in Sec. 1.3.1 with the brick-wall geometry. The front, defined by the boundary between regions of $\mathcal{C}(x,t) = \mathcal{O}(1)$ and $\mathcal{O}(0)$, provides a characteristic velocity called the butterfly velocity v_{b}. Furthermore, the front is shown to broaden diffusively as $t^{1/2}$ by using a mapping to classical statistical mechanical problems [**?**, **?**].

1.2.6 Operator spreading

1.2.6.1 Lieb-Robinson Bound

For a spatially-extended physical system, locality implies the existence of an upper bound to the speed at which quantum information can spread, known as the Lieb-Robinson (LR) bound [**?**]. Let $\hat{O}$ be an observable with finite support. $\hat{O}$ evolves in time under a Hamiltonian $\hat{H}$ as $\hat{O}(t) = e^{i\hat{H}t}\hat{O}e^{-i\hat{H}t}$. Lieb and Robinson proved that for a local and translational-invariant $\hat{H}$ and for observables $\hat{A}$ and $\hat{B}$,

$$\left|\left|[\hat{A}(t), \hat{B}(0)]\right|\right| \leq c \exp\{-a[d(X,Y) - v_{\mathrm{LB}}|t|]\} \,, \tag{1.27}$$

where $||\cdot||$ is the operator norm; $[\cdot,\cdot]$ is the commutator; X and Y are the supports of operator $\hat{A}$ and $\hat{B}$; $d(X,Y)$ denotes a notion of distance between the supports X and Y; c is a constant that depends on the norms of $\hat{A}$ and $\hat{B}$; a is a positive constant; and v_{LR} is the LR velocity. Eq. (1.27) states that the support of the operator outside

of the lightcone defined by $v_{\rm LR}$ is suppressed exponentially by the LR bound. The LR bound has been generalized to systems with exponentially decaying interactions [**?**], systems without translation invariance [**?**, **?**, **?**, **?**] etc. Next, we will describe how quantum chaos can be probed by how quantum information spreads within the finite speed set by the LR bound.

1.2.6.2 Out-of-time-order commutator

Although a naive generalization of the butterfly effect as overlap of quantum states is not fruitful (Sec. 1.2.1), one can alternatively characterize quantum chaos by focusing on physical observables. To this end, we may attempt to generalize the classical butterfly effect characterized in Eq. 1.2 to the quantum case by using the Poisson bracket $\{\cdot,\cdot\}_{\rm Poisson}$, and promoting it to a commutator $[\cdot,\cdot]$ via the canonical quantization,

$$\frac{\partial x(t)}{\partial x_0} = \{x(t), p_0\}_{\rm Poisson} \quad \longrightarrow \quad -i\,[\hat{x}(t), \hat{p}]\ , \tag{1.28}$$

where we are using the convention $\hbar = 1$. However, the expectation value of this quantity with respect to some density matrix is vanishing since this observable can take different signs. A natural remedy is to consider its norm square, $|[\hat{x}(t), \hat{p}]|^2$, which is an example of an out-of-time-order (OTO) commutator. The OTO commutator first appears in the context of superconductivity [**?**], and has recently received a lot of attention in the high energy physics community [**?**, **?**, **?**].

Generally, we define the OTO commutator for local Hermitian operators $\hat{O}(x) = \mathbb{1} \otimes \cdots \otimes \mathbb{1} \otimes \hat{O}_x \otimes \mathbb{1} \otimes \cdots \otimes \mathbb{1}$ at site x as

$$\mathcal{C}(x-y,t) = \frac{1}{2}\,\mathrm{Tr}\,\rho_\infty |[\hat{O}(x,t), \hat{O}(y)]|^2 = 1 - \mathrm{Tr}\,\rho_\infty \hat{O}(x,t)\hat{O}(y)\hat{O}(x,t)\hat{O}(y)\ , \tag{1.29}$$

where $\hat{O}(x,t) \equiv e^{i\hat{H}t}\,\hat{O}(x)\,e^{-i\hat{H}t}$, ρ_∞ is the infinite-temperature density matrix, and we take $\hat{O}(x)$ to square to identity. The second term in right hand side of Eq. (1.29)

is known as the out-of-time correlator, which we abbreviate in this thesis as OTOC. The OTO commutator can be intuitively understood as a quantity that probes how the operator $\hat{O}$ spreads from spacetime coordinate $(y, 0)$ to (x, t): $\mathcal{C}(x - y, t)$ is close to identity (zero) if there is (not) a support of $\hat{O}(x, t)$ at site y (see Fig. 1.6 for an example). For models of quantum chaotic systems, the computation of the OTO commutator shows that a local operator spreads with a ballistic light cone (e.g. Fig. 1.6) [**?**, **?**, **?**, **?**], and the OTO commutator approaches its long-time limit with an exponential decay [**?**, **?**, **?**]. On the other hand, for MBL systems, a local operator spreads with a logarithmic light cone [**?**], and the OTO commutator approaches its long-time limit as a power law [**?**, **?**].

Despite the above motivations for using the OTO commutator, there are apparent tensions in the analogy between the OTO commutator and the classical notion of the butterfly effect. For instance, $\left|\frac{\partial x(t)}{\partial x_0}\right|$ increases exponentially, while the OTO commutator as defined in Eq. (1.29) is known to saturate at a time linear in x. We will not address such questions in this thesis, and we refer the readers to [**?**, **?**] for further investigations.

1.2.7 Entanglement entropy

A bipartite system is a system whose Hilbert space can be written as a direct product of two Hilbert spaces,

$$\mathcal{H}_{AB} = \mathcal{H}_A \otimes \mathcal{H}_B \ . \tag{1.30}$$

The reduced density matrix of a subsystem A is defined using the partial trace,

$$\hat{\rho}_A = \mathrm{tr}_B \, \hat{\rho} \ . \tag{1.31}$$

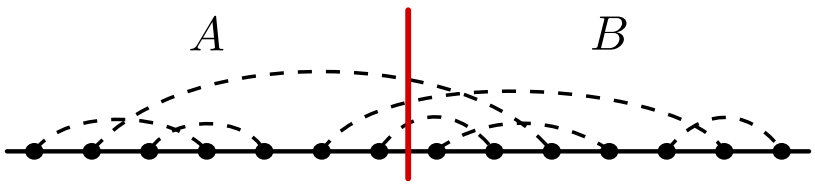


Figure 1.7: Consider a quantum state of a direct product of bell pairs. The entanglement entropy of this state quantifies the number of bell pairs that straddle across the partition between subsystems A and B (red).

The α-th Renyi entropy is defined using the equation

$$e^{(1-\alpha)S_\alpha} = \mathrm{tr}_A\, \hat{\rho}_A^\alpha \ , \tag{1.32}$$

and the entanglement purity $\mathcal{P}$ is defined as Eq. (1.32) in the case of $\alpha = 2$, that is, $\mathcal{P} = e^{-S_2}$. In the limit of $\alpha \to 1$, the Renyi entropy coincides with the von Neumann entropy,

$$S_{\mathrm{vN}} = \mathrm{tr}_A\, \hat{\rho}_A \log \hat{\rho}_A \ . \tag{1.33}$$

This thesis will focus on a d-dimensional, L^d-site quantum spin chain with local Hilbert space dimension q. A and B are chosen to be two complementary subregions of space, often as complementary halves of the chain. To get an intuition of what entanglement entropy characterizes, consider a 2-qubit example, where A and B contain the first and the second bit respectively. Denote a basis state as $|ij\rangle \equiv |i\rangle_A \otimes |j\rangle_B$. Suppose the system is in the pure state, $|\psi\rangle = \frac{1}{\sqrt{2}}(|00\rangle + |11\rangle)$. It is easy to compute $\hat{\rho}_A = \frac{1}{2}\mathbb{1}$ and $S_{\mathrm{vN}} = \log 2$. Since this is the maximum value of S_{vN}, we say $\hat{\rho}_A$ is maximally mixed and $|\psi\rangle$ is maximally entangled. This example illustrates a general interpretation of S_α (Fig. 1.7): Entanglement entropy quantifies the amount of entanglement between degrees of freedom in A and the ones in B.

The scaling of S_α with time is an important diagnostic of quantum chaotic systems: In a quantum quench setup, a quantum chaotic system prepared in a low-entanglement initial state has $S_\alpha(t) \propto t$ [**?**], while a many-body localized system

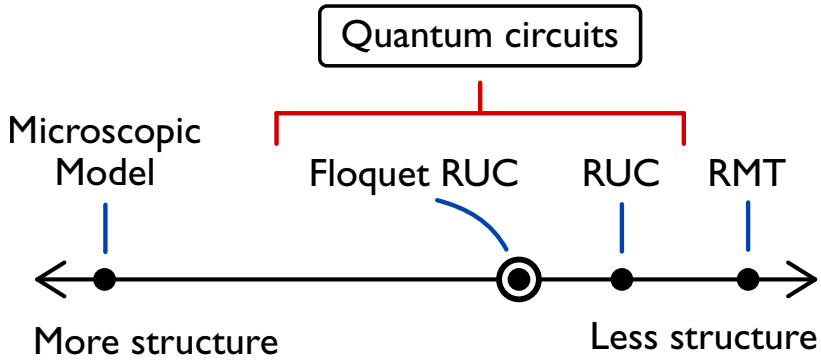


Figure 1.8: A schematic plot of some theoretical models according to the amount of physical structures and features the models retain. This thesis focus on a particular class of quantum circuits, called Floquet random unitary circuits, which are random in space and periodic in time.

has $S_\alpha(t) \propto \ln t$ [?, ?]. Furthermore, the saturation of S_α in late time can be used to quantify the complexity of a given quantum state. A quantum state is said to obey the volume law (area law) if S_α scales with the number of degrees of freedom in the bulk (boundary) of the system, i.e. $S_\alpha \sim L^d$ ($S_\alpha \sim L^{d-1}$). A generic state in a quantum chaotic system obeys the volume law, while every eigenstate for a disordered system in the MBL phase obeys the area law [?]. An important consequence of the behaviour of S_α is that area-law states can be efficientially simulated using numerical tools like the density matrix renormalization group [?, ?].

1.3 Quantum circuits

The phenomena exhibited in an ensemble of random matrices, such as the fluctuations in level statistics, are so commonly seen in nature that RMT is used to effectively define quantum chaos via the BGS conjecture [?] (Sec. 1.2.4). However, in exchange for analytical tractability, RMT has been constructed to leave out important structures of realistic physical systems, in particular, the notion of locality [?]. Most ensembles studied in RMT are invariant under the rotation of basis, but this is not true in physical systems: The Lieb-Robinson bound states that there is an

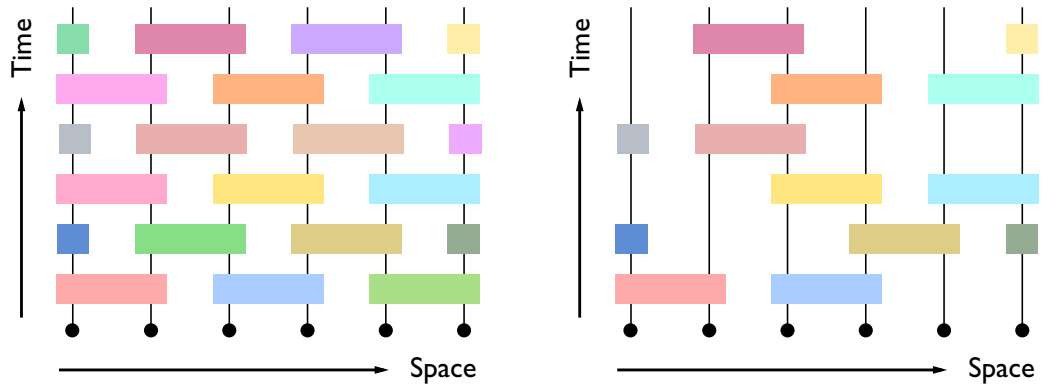


Figure 1.9: Illustrations of RUCs with the brick-wall geometry (left) and a random geometry (right) studied in [**?**, **?**, **?**]. Each site has a q-dimensional Hilbert space, and each rectangle represents an independently-drawn $q^2 \times q^2$ Haar-random unitary.

upper bound on the speed at which information propagates in quantum systems [**?**] (Sec. 1.2.6.1), and hence there exist prefered bases where the local spreading of information is manifest. As an example, consider a 1D spin chain prepared in a low-entanglement state. Under the evolution of a local Hamiltonian, far-apart spins do not interact at sufficiently early time, and hence the description of RMT does not apply. This suggests that there must be a time scale, which we call the many-body Thouless time t_{Th}, before which RMT is not effective [**?**]. An important objective is to construct and solve models which describe the physics in this early time regime.

A quantum circuit is a sequence of quantum unitary gates describing discrete time evolution. When these quantum gates are locally-supported and are drawn from a random matrix ensemble (e.g. CUE), the quantum circuit has a notion of locality and also retains some of the analytical tractibility of RMT (Fig. 1.8). Such a quantum circuit is a minimal model of spatially-extended many-body quantum systems, and provides an ideal tool to explore non-equilibrium quantum dynamics. In the following subsections, we will introduce two classes of quantum circuits as minimal models of spatially-extended many-body quantum systems.

1.3.1 Random unitary circuits

We use the term random unitary circuits (RUC) to refer to quantum circuits (with local unitary gates) that are random in *both* space and time (as opposed to being random only in space). The full randomness of RUC significantly simplifies computations of ensemble averages of observables, and allows exactly solvable results.The early examples of RUCs [**?**, **?**, **?**] are one-dimensional L-site unitary circuits with a single-site Hilbert space dimension q. These circuits consist of 2-site local, Haar-distributed random unitaries placed in geometries as illustrated in Fig. 1.9. As an example, the RUC with the brick-wall geometry (Fig. 1.9 left) is defined by the time evolution operator $\hat{W}(t) = \hat{U}(t)\hat{U}(t-1)\hat{U}(t-2)\dots\hat{U}(1)$

$$\hat{U}(t) = \begin{cases} \bigotimes_{i\in 2\mathbb{Z}} \hat{U}_{i,i+1}(t) & \text{if } t \text{ is even.} \\ \bigotimes_{i\in 2\mathbb{Z}+1} \hat{U}_{i,i+1}(t) & \text{if } t \text{ is odd.} \end{cases} \tag{1.34}$$

where $\hat{U}_{i,i+1}(t)$ is a $q^2 \times q^2$ Haar random unitary matrix acting on sites i and $i+1$.

In 1D, the ensemble average of the OTO commutator over the RUC with the brick-wall geometry defined in Eq. 1.34 satisfies a biased diffusion equation, which allows analytical solution for the spatio-temporal profile of the OTO commutator (Fig. 1.6). A front, defined by the boundary between regions of $\mathcal{C}(x,t) = \mathcal{O}(1)$ and $\mathcal{O}(0)$, specifies a characteristic velocity called the butterfly velocity v_{b}, which is analytically tractable for all q. In general dimension, there exists a mapping between the OTO commutator and a classical droplet growth problem which allows understanding of how the OTO commutator front broadens via the Kardar-Parisi-Zhang (KPZ) universality class [**?**, **?**]. Additionally, the ensemble average of the entanglement entropy of a RUC with random geometry (Fig. 1.9 right) can be shown to obey the KPZ equation in 1D (albeit due to a completely different mechanism). This connection implies that

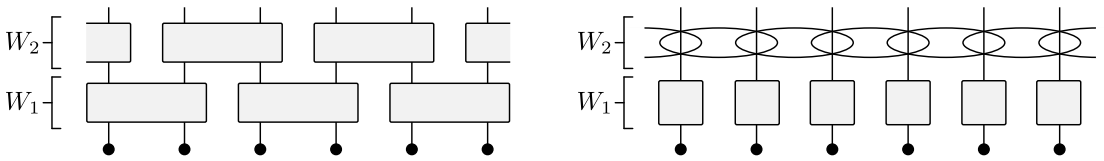


Figure 1.10: Illustrations of Floquet RUCs studied in [**?**, **?**, **?**]. Left: A Floquet circuit acting on q-state spin with $q^2 \times q^2$ Haar-random unitaries in the brick-wall geometry. Right: A Floquet circuit acting on q-state spin consisting one layer of independent single-site rotation operators, and another layer of diagonal 2-gates coupling nearest-neighbouring sites.

the entanglement of this model grows linearly in time, and the fluctuation grows in time with a scaling exponent of 1/3 [**?**].

1.3.2 Floquet random unitary circuits

A step towards a model more realistic than RUCs is to remove the randomness in time (see Fig. 1.8). Importantly, a time-periodic or 'Floquet' random unitary circuit provides an analytically tractable, well-defined spectrum (which is absent in the RUCs), while still retains a relatively simple setting since all conserved quantities, including the energy density, can be removed. The difficulty of analysing Floquet circuits is the computation of the higher moments of random matrices in the ensemble average of observables. The main objective of this thesis is to use such models to probe features of quantum chaotic many-body systems. We will introduce two Floquet random unitary circuits. In a single period of time evolution, both Floquet circuits contain two layers of random matrices, which act on q-state spins arranged with nearest-neighbour coupling on a d-dimensional lattice. For concreteness, we will first describe the models with $d = 1$ and L sites.

The first Floquet circuit, which we call the Floquet random unitary circuit (FRUC), is similar to the RUC in Eq. (1.34) except for the time periodicity [**?**]. Formally, this model is a one-dimensional L-site Floquet unitary circuit generated by Haar-distributed random unitaries with the brick-wall geometry (Fig. 1.10 left).

The circuit is defined by a $q^L \times q^L$ Floquet operator $\hat{W} = \hat{W}_2 \cdot \hat{W}_1$, where

$$\begin{aligned} \hat{W}_1 &= \hat{U}_{1,2} \otimes \hat{U}_{3,4} \otimes \ldots \hat{U}_{L-1,L} \\ \hat{W}_2 &= \mathbb{1}_q \otimes \hat{U}_{2,3} \otimes \hat{U}_{4,5} \otimes \ldots \mathbb{1}_q \end{aligned} . \tag{1.35}$$

As before, each $U_{i,i+1}$ is a $q^2 \times q^2$ random unitary matrix acting on sites i and $i+1$. In the limit $q \to \infty$, the FRUC is analytical solvable. However, quantum information spreads as quickly as it can in this limit. In order to have control over the strength of coupling between sites while keeping the analytical tractability at $q \to \infty$, we introduce another Floquet model.

The second Floquet model, which we call the Floquet random phase circuit (FRPC), consists of one layer of Haar-random 1-site gates, and another layer of diagonal 2-site gates with random phases in the diagonal entries. Formally, we use site labels $i = 1 \ldots L$ and orbital labels $a_i = 1 \ldots q$ on the ith site. The model is defined by a $q^L \times q^L$ Floquet operator $\hat{W} = \hat{W}_2 \cdot \hat{W}_1$ (Fig. 1.10 right). The first layer

$$\hat{W}_1 = \hat{U}_1 \otimes \hat{U}_2 \otimes \ldots \hat{U}_L \tag{1.36}$$

generates independent rotations at each site n, with $q \times q$ Haar-random unitary matrices $\hat{U}_n$. The second layer W_2 couples neighbouring sites and is diagonal in the basis of site orbitals. The phase of the diagonal elements is a sum of terms depending on the quantum states of adjacent sites, so that

$$[W_2]_{a_1,\ldots a_L;a_1,\ldots a_L} = \exp\left(i \sum_i \varphi_{a_i,a_{i+1}} \right) . \tag{1.37}$$

We take each $\varphi_{a_i,a_{i+1}}$ to be an independent Gaussian random variable with mean zero and variance ϵ. To construct a similar model in higher dimensions we use sites $\mathbf{r}$ on a

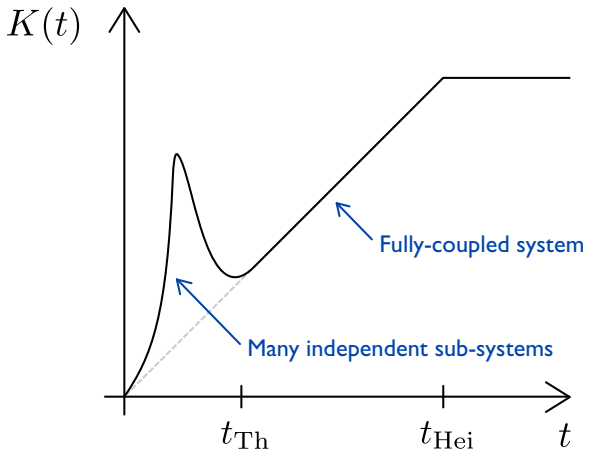


Figure 1.11: Schematic illustration of the behaviour of the spectral form factor for spatially-extended many-body quantum chaotic systems. There exists a many-body Thouless time, t_{Th}, after which the RMT form of the spectral form factor applies (c.f. Fig. 1.5).

hypercubic lattice and take independent contributions $\varphi_{a_{\mathbf{r}},a'_{\mathbf{r}}}$ to the phase of $\hat{W}_2$ from each neighbouring pair of sites, $\mathbf{r}$ and $\mathbf{r}'$.

1.4 Summary of results

Using the two Floquet models described in Sec. 1.3.2, we will provide insights on the dynamical behaviours [?], the spectral statistics [?] and the eigenstate correlation [?] (beyond the ones described by ETH) of spatially-extended many-body quantum chaotic systems. These three results will be presented in Chapter 2, 3 and 4 respectively.

In [?], we focus on the FRUC as a minimal model for spatially-extended many-body quantum chaotic systems. We provide a diagrammatical formalism for computing ensemble averages of observables over such quantum circuits, and show how this approach leads to exact results in the large-q limit. We give results for the spectral form factor, relaxation of local observables, bipartite entanglement entropy growth and operator spreading.

In [**?**], we study spectral statistics in spatially-extended many-body quantum chaotic systems, using the FRPC. Computing the spectral form factor $K(t)$ analytically and numerically, we show that it follows RMT at times longer than a many-body Thouless time, $t_{\rm Th}$ (Fig. 1.11). We obtain a striking dependence of $t_{\rm Th}$ on the spatial dimension d and size of the system. For $d > 1$, $t_{\rm Th}$ is finite in the thermodynamic limit and set by the inter-site coupling strength. By contrast, in one dimension $t_{\rm Th}$ diverges with system size, and for large systems there is a wide window in which spectral correlations are not of RMT form. Additionally, we show numerically that the FRPC exhibits a many-body localization transition and we discuss the behavior of the spectral form factor in the localized phase.

In [**?**], we discuss eigenstate correlations for spatially-extended many-body quantum chaotic systems, in terms of the statistical properties of matrix elements of local observables. While the ETH is known to give an excellent description of these quantities, the phenomenon of scrambling and the butterfly effect imply structure beyond ETH. We determine the universal form of this structure at long distances and small eigenvalue separations for Floquet systems. We use numerical studies of the FRUC to illustrate both the accuracy of ETH and the existence of our predicted additional correlations.

Chapter 2

Solution of a minimal model of many-body quantum chaotic systems

2.1 Introduction

Chaotic many-body quantum systems lie at the focus of efforts to understand the foundations of quantum statistical mechanics [?, ?, ?, ?]. Generic features expected in the dynamics of such systems include rapid equilibration of local observables [?] and ballistic propagation of quantum information, [?] as well as ballistic growth of bipartite entanglement [?, ?]. Recently, random unitary circuits (Sec. 1.3.1) that are random in both space and time have yielded valuable insights into chaotic quantum dynamics [?, ?, ?, ?, ?, ?]. In this chapter, we develop a diagrammatic approach to analyse Floquet random unitary circuits which are random in space but *periodic* in time (Sec. 1.3.2).

More precisely, we study the one-dimensional FRUC defined in Eq. (1.35). The FRUC consists of random local quantum gates acting on a spatially-extended system

with q-state 'spins' at each site. Our key simplification is to treat the large-q limit. We show that quantum dynamics in this system exhibits a range of features that are expected to be characteristic of ergodic many-body quantum systems: correlators of local observables decay rapidly in time and quantum information spreads ballistically, in the sense that the bipartite entanglement of an initial product state grows linearly in time, and the OTOC [**?**, **?**] shows the butterfly effect. Our approach also provides access to the spectral properties of the Floquet operator and we show (on scales much larger than the level spacing) that its eigenvalue correlations are those of the CUE. At a technical level, our calculations are based on the application of diagrammatic techniques developed previously for single-particle problems in mesoscopic physics involving random matrices from the CUE [**?**].

Some features of the large-q limit are non-generic: as for random unitary circuits [**?**, **?**] at large q, the distinction between the velocities associated with entanglement and operator spreading vanishes; and sublinear growth of entanglement, expected at long times in one dimensional disordered systems because of weak links [**?**], is absent.

This chapter is organised as follows. In Sec. 2.2, we summarise the results. In Sec. 2.3, we develop the diagrammatic approach for taking the ensemble average of a given observable. In Sec. 2.4, we sketch the proof of the results presented in Sec. 2.2 using the tools developed in Sec. 2.3. In Sec. 2.5, we give a discussion and an outlook. The technical details of the proofs are described in Appendix A.

2.2 Summary of results

To demonstrate that FRUC has the features expected in a chaotic quantum many-body system, we examine a range of physical properties, as detailed below. Our results for entanglement spreading and for the OTOC are the same as those for random unitary circuits with the same structure as our model, if one takes the large

q limit in previous results [**?**, **?**]. In this context, one of our significant conclusions is that random unitary circuits do indeed share important physical features with deterministic systems. At the same time, our model opens up discussion of the spectral properties of the evolution operator. This has no equivalent for random unitary circuits since they lack any such fixed operator.

In the rest of the thesis, we denote the evolution operator for an integer number t of periods $\hat{W}^t$ by $\hat{W}(t)$. We also may drop the hat of an operator when there is no ambiguity.

2.2.1 Spectral form factor

SFF, $K(t)$, is the Fourier transform of the two-point correlation function of the eigenvalue density (Sec. 1.2.4.2). Our results for SFF show that the Floquet operator for the model has exactly the same eigenvalue correlations in the large q limit as an ensemble of Haar-distributed unitary matrices. This insensitivity to the spatial structure of the system is a striking emergent feature.

More precisely, SFF averaged over the FRUC coincides exactly with the CUE form, $K(t) = |t|$ for $t \neq 0$, in the large q limit at fixed L and t. We stress that this result is a consequence of coupling between all sites, and is not simply a reflection of the properties of individual random matrices $U_{i,i+1}$ in Eq. (1.35). To illustrate the point, consider an alternative model in which the couplings $U_{2n,2n+1}$ on even bonds are replaced with unit matrices $\mathbb{1}_{q^2}$. For this toy system of $L/2$ independent pairs of sites one has much larger fluctuations in eigenvalue density, with $K(t) = |t|^{L/2}$ for $0 < |t| \leq q^2$.

Returning to the original model, it is interesting to speculate on behaviour in regimes other than the one we are able to analyse exactly. At large but fixed q and fixed t, it is natural to expect $K(t)$ to increase with L if L is sufficiently large, since distant parts of the system should be only weakly correlated; results for this regime

will be presented elsewhere in Sec. 3. In the opposite limit, fixing q and L and varying t, the form of $K(t)$ at $|t| \sim q^L$ probes correlations on the scale of the level spacing. We expect these to be of CUE form for all q and L, provided only that $q^L \gg 1$. They should therefore show a transition from $K(t) = |t|$ for $|t| \lesssim q^L$ to $K(t) = q^L$ for $|t| \geq q^L$. The transition to constant $K(t)$ at large t is, however, well-known to be inaccessible in a perturbation expansion in inverse powers of q [**?**, **?**].

2.2.2 Dynamics

We next examine physical properties chosen to reveal both the dynamics of local degrees of freedom and the spreading of quantum information.

2.2.2.1 Local relaxation

A characteristic feature of chaotic dynamics is that local observables relax rapidly towards equilibrium. To probe relaxation in our model we introduce a local operator $O(x)$ representing an observable at site x and obeying $O(x)^\dagger = O(x)$, $\mathrm{Tr}\, O(x) = 0$ and $O(x)^2 = \mathbb{1}_{q^L}$. Let $O(x,t) = W^\dagger(t)O(x)W(t)$. The statistical average for a system with density matrix ρ is $[\ldots]_{\mathrm{av}} = \mathrm{Tr}\,[\rho \ldots]$. In our Floquet model the infinite-temperature density matrix $\rho = q^{-L}\mathbb{1}_{q^L}$ is the natural choice and we denote the normalised many-body trace by $\mathrm{tr} \equiv q^{-L}\mathrm{Tr}$. We will use $\langle\cdot\rangle$ to denote the ensemble average over the FRUC.

One anticipates that $[O(x,t)O(x)]_{\mathrm{av}}$ will relax to the value $[O(x)]^2_{\mathrm{av}}$ (which is zero with this form for $O(x)$) on a microscopic timescale of order the Floquet period. At large q we in fact find complete relaxation within a single period, obtaining for $q \to \infty$ the result

$$\langle \mathrm{tr}[O(x,t)O(x)]\rangle = \delta_{t,0}\,. \tag{2.1}$$

We discuss the leading corrections to this result for finite q and small t in Sec. 2.4.2.

2.2.2.2 Entanglement spreading

We probe entanglement spreading via the time dependence of the ensemble-averaged bipartite entanglement purity (and, more generally, ensemble averages of exponentials of Rényi entropies) for an initial state $|\psi\rangle$ that is a direct product over sites. Specifically, let A be the left half of the system (with site labels $1 \leq n \leq L/2$) and B the right half, and consider the reduced density matrix evolving in time under the Floquet operator $W(t)$,

$$\rho_A(t) = \mathrm{Tr}_B[W(t)|\psi\rangle\langle\psi|W^\dagger(t)]\,. \tag{2.2}$$

We compute the generalized quantum purity $\langle e^{(1-\alpha)S_\alpha(t)}\rangle$ for $\alpha = 2$ and $\alpha = 3$. The purity shows an exponential decay in time until it falls to a value $\mathcal{P}(t) \sim q^{-L/2}$ typical of random states in the many-body Hilbert space. In detail, we obtain at large q

$$\langle e^{(1-\alpha)S_\alpha(t)}\rangle \sim \begin{cases} f_\alpha(t)\; q^{-2(\alpha-1)t} & t \leq L/4 \\ K_\alpha q^{-(\alpha-1)L/2} & t > L/4 \end{cases} \tag{2.3}$$

The function $f_\alpha(t)$ grows exponentially with t, and in particular, we find $f_2(t) = 4^t$ and $f_3(t) \simeq ((4+3\sqrt{2})/2)^{2t}$ for $t \gg 1$. At times $t > L/4$, the Renyi entropies saturate and we conjecture that $K_\alpha = \mathrm{Cat}(\alpha)$, where Cat is the α-th catalan number. The latter result is proven for α up to 5 (see Appendix A.6). This is consistent with the generalized Page formula for bipartite entanglement in random states [**?**][**?**] and with the results from random unitary circuit [**?**].

An interpretation of these results is that the reduced density matrix for the pure initial state spreads at time t over the Hilbert space spanned by basis states at $2t$ sites. As an illustration, suppose that $\rho_A(t)$ has q^{2t} non-zero eigenvalues that are all equal. Then $\mathrm{Tr}_A\rho_A(t) = q^{-2(\alpha-1)t}$, which is consistent with the leading order behaviour of (2.3) for $t \leq L/4$. This demonstrates that the entanglement spreads ballistically with

a velocity at large q that is the same as the naive light-cone velocity, $v = 2$, introduced below in Fig. 2.1. The values of $f_2(t)$ and $f_3(t)$ give information on the distribution of non-zero eigenvalues of $\rho_A(t)$, and it is noteworthy that these two quantities are distinct.

The growth of entanglement found here is similar to that obtained for integrable systems using conformal field theories [**?**, **?**, **?**]. In integrable systems this behaviour is associated with the presence of quasiparticles that travel ballistically; a quite different physical picture is required for ergodic systems.

2.2.2.3 Out-of-time-order correlator

The spreading with time of local operators is characterised by the behaviour of the (ensemble-averaged) OTO commutator (or correlator) in Eq. (1.29), which measures how a local perturbation at site x affects measurements at a later time at the site y. Generally, for short times t and large separations $x - y$, the operators $O(x, t)$ and $O(y)$ commute and $\mathcal{C}(x - y, t)$ is zero, while for large times the OTOC is small and $\mathcal{C}(x - y, t)$ approaches unity. For the FRUC, we obtain at large q a sharp light-cone behaviour

$$\mathcal{C}(x-y,t) = \begin{cases} 0 & |t| < |x-y|/2 \\ \\ 1 & |t| \geq |x-y|/2\,. \end{cases} \tag{2.4}$$

Hence operator spreading occurs with a butterfly velocity that, like the entanglement velocity, is equal to the naive light-cone velocity $v = 2$ in the large q limit. Results on random unitary circuits [**?**, **?**] suggest that all three velocities should be distinct for q finite. From the same comparison, we also expect at finite q that the step function in Eq. (2.4) will broaden.

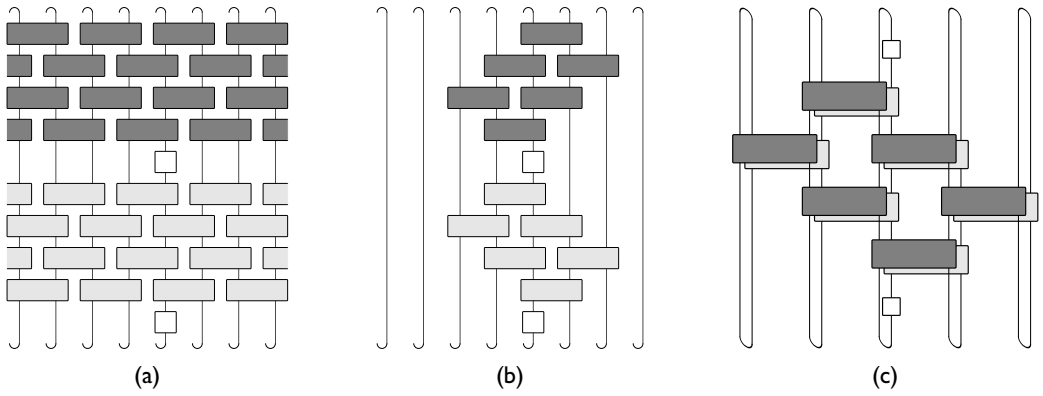


Figure 2.1: Illustration of $\mathrm{Tr}[O(t)O(0)]$ for $t = 2$. Us and $U^\dagger$s are represented by rectangles, respectively shaded in light and dark grey. The local operator O_x is represented by a square. The curled lines at the top and bottom edge indicate closed loops which denote the trace operation. (a): Initial expression. (b): After cancellation of pairs of U with $U^\dagger$ wherever possible. The boundaries of the regions within which Us and $U^\dagger$s remain form lightcones with a velocity $v = 2$ set by the construction of the model. (c): Illustration of $\mathrm{Tr}[O(t)O(0)]$ for $t = 2$ formed by folding Fig. 2.1 (right) so that timelines run upwards for W and downwards for $W^\dagger$.

2.3 Ensemble averaging

We now set out in several steps the general approach that we use to obtain these results.

First, it is useful to extend the notation of Fig. 1.10 left in various ways, so as to represent pictorially the quantities defined in Sec. 2.2. An example for $\mathrm{Tr}[O(x,t)O(x,0)]$ is shown in Fig. 2.1. The vertical timelines of sites join rectangles representing factors of $U_{i,i+1}$ and indicate matrix multiplication. Repeated copies of W denote multiple time steps; $W^\dagger$ is shown as a differently shaded version of W; and local operators appear as squares. The matrix trace is shown by joining the timelines of sites to form closed loops. Finally, product states in the site basis (which do not appear in this example) are shown using circles at the ends of the timelines.

A straightforward simplification in many instances is that some factors of U and $U^\dagger$ cancel, as illustrated in Fig. 2.1b, and the naive light-cone velocity $v = 2$ clearly emerges.

As a second step, it is helpful to fold the pictorial representations, so that while the timelines in W run upwards, those in $W^\dagger$ run downwards, as shown in Fig. 2.1c.

These folded pictures provide a direct depiction of physical quantities but are cumbersome. A simpler representation is possible if we focus on the time evolution of a single site. To this end, and in anticipation of the disorder average, we switch to an alternative notation for $U_{i,i+1}$ and $U^\dagger_{i,i+1}$ in which individual sites appear separately, as shown in Fig. 2.2.

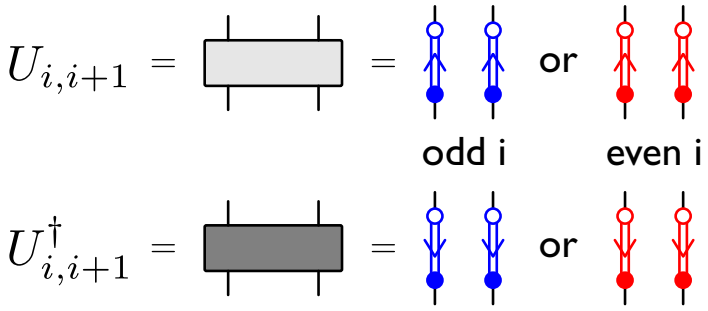


Figure 2.2: Adaptations to diagrammatic notation made in order to show time evolution of an individual site. The shaded rectangles representing $U_{i,i+1}$ and $U^\dagger_{i,i+1}$ are replaced by pairs of double lines, with an arrow directed from the column-label to the row-label of the matrix. To record the distinction between odd and even i, the double lines are blue in the first case and red in the second. This colour convention allows us to represent single-site diagrams without ambiguities (see e.g. Fig. 2.6).

With these preliminaries in place, we can set out a diagrammatic representation for ensemble averages. It is a many-body extension of the one introduced for averages over the CUE by Brouwer and Beenakker [**?**]. It can be applied to an arbitrary observable $f(W)$ but to be definite we illustrate it for $K(t)$ with $t = 2$ and $L = 2$, so that $W(2) = [U_{1,2}]^2$. In general three steps are involved.

(i) The observable $f(W)$ is represented as a collection of single-site diagrams using the notation introduced in Fig. 2.2. For the example of $K(t{=}2)$, one starts from the many-body diagram shown in Fig. 2.3 right and obtains the single-site representation shown in Fig. 2.4 left.

(ii) The ensemble average $\langle f(W)\rangle$ is computed by generating a collection of single-site 'contracted' diagrams $G = \{G_i\}_{i=1}^{L}$ as follows. On each site, filled U-dots are

connected to filled $U^\dagger$-dots of the same color on the same site with a dashed line (a contraction) in all possible ways, and likewise for the empty dots.

Since Us and $U^\dagger$s act on neighbouring pairs of sites, these contractions must be matched: for even i the choice of contractions between blue dots must be the same in the diagrams G_{i-1} and G_i; similarly for the red dots and the diagrams G_i, G_{i+1}. We refer to this as the *bond constraint*.

(iii) Each contracted site diagram G_i gives rise to an algebraic expression $\mathcal{A}(G_i)$, obtained as the product of two factors

$$\mathcal{A}(G_i) = \mathcal{A}_T(G_i)\mathcal{A}_U(G_i) \ . \tag{2.5}$$

These factors are associated with loops of two kinds, called T-loops and U-loops in Ref. [**?**]. The T-loops simply record pairings of matrix labels, and give rise to powers of q in the contribution of a diagram. The U-loops distinguish different contributions from the average of factors of U and $U^\dagger$. Examples of these two types of loop are illustrated in Fig. 2.5.

A T-loop is a closed sequence of alternating single and dashed lines. It carries an index corresponding to one of the q basis states at a site. We generate the contribution associated with each T-loop by summing over its index. This leads to a factor of q for a T-loop of single lines if it does not pass through any operator insertion, or of $\mathrm{Tr}(O_1O_2\dots)$ if the T-loop passes through the operators $\{O_1, O_2, \dots\}$. The overall factor $\mathcal{A}_T(G_i)$ is obtained as the product of the individual factors coming from each T-loop.

A U-loop is a closed sequence of alternating double and dashed lines. The length c of a U-loop is defined as half of the number of double lines it contains. Let $R_i = \{c_k^{(r)}\}_{k=1}^{r_i}$ and $B_i = \{c_k^{(b)}\}_{k=1}^{b_i}$ be the sets of lengths of red and blue U-loops in G_i.

Then from the theory of CUE averages [**?**]

$$\mathcal{A}_U(G_i) = (V_{R_i} V_{B_i})^{1/2} \tag{2.6}$$

where the explicit form of the coefficients $V_{R_i} \equiv V_{c_1 \ldots c_{r_i}}$ and $V_{B_i} \equiv V_{c_1 \ldots c_{b_i}}$ (also known as the Weingarten functions) is given in Appendix A.1. Note that the exponent $1/2$ in (2.6) arises because we distribute the contribution arising from unitary operators equally over the two sites on which the operators act.

The final value of the ensemble average reads

$$\langle f(W) \rangle = \sum_G \prod_i \mathcal{A}(G_i) \tag{2.7}$$

where the sum runs over all contracted diagrams G satisfying the bond constraint.

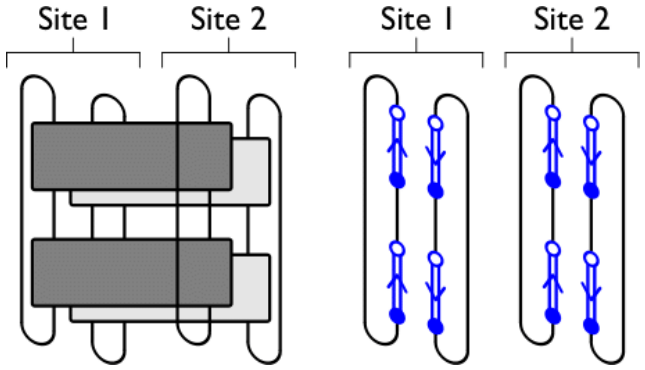


Figure 2.3: Alternative diagrammatic representations of $\mathrm{Tr}[W(t{=}2)]\mathrm{Tr}[W^\dagger(t{=}2)]$, which gives $K(t{=}2)$ after ensemble-averaging, using the notation of the left and right sides of Fig. 2.2.

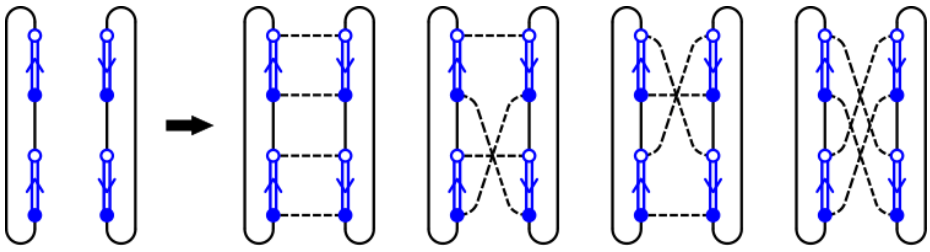


Figure 2.4: Single-site diagrams associated with $\mathrm{Tr}[W(t{=}2)]\mathrm{Tr}[W^\dagger(t{=}2)]$ (left) and its ensemble average $K(t=2)$ (right).

For the example of $\langle K(t{=}2)\rangle$, all possible single-site contracted diagrams are drawn

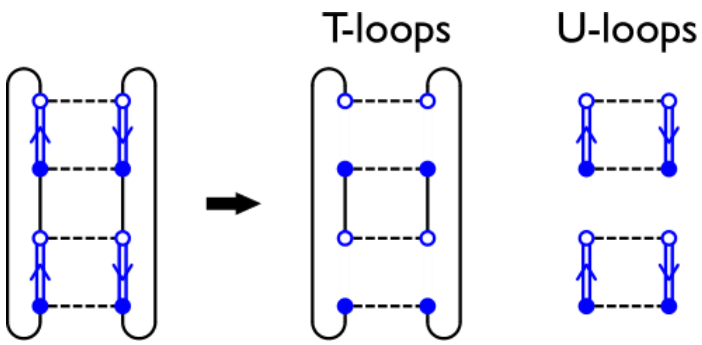


Figure 2.5: The T- and U- loops (right) associated with a contracted diagram for $\mathrm{Tr}[W(t{=}2)]\mathrm{Tr}[W^\dagger(t{=}2)]$ (left in this figure and top middle in Fig. 2.4). The associated algebraic factors are $\mathcal{A}_T(G_i) = q^2$ and $\mathcal{A}_U(G_i) = (V_{1,1})^{1/2}$.

in Fig. 2.4 right. Explicit evaluation of the algebraic expressions for this case leads to

$$\langle K(t=2)\rangle = \left(q^4 V_{1,1} + q^2 V_2 + q^2 V_2 + q^4 V_{1,1}\right) \approx 2\,. \tag{2.8}$$

The factors of q within the bracket are contributions from the T-loops. We have taken the large-q limit on the far right, using $V_{1,1} = (q^4-1)^{-1}$ and $V_2 = -[q^2(q^4-1)]^{-1}$. At large q the first and fourth diagrams are leading order, while the second and third are sub-leading.

The above procedure is exact for any q, but the sum in (2.7) is problematic in general as it may involve an extremely large number of terms. For example, a total of $(t!)^{2(L-1)}$ diagrams contribute to $K(t)$. It is therefore useful to establish which terms dominate in the large-q limit. For large q one has $\mathcal{A}_U(G_i) \sim q^{u_i - n_i}$ where $u_i = r_i + b_i$ is the total number of U-loops and $n_i = \sum_k c_k$ is the number of contractions on the i-th site. Let τ_i be the number of T-loops in G_i that contribute a factor q. Then we have the large-q expansion

$$\prod_i \mathcal{A}(G_i) \sim \prod_{i\in\text{site}} q^{\tau_i + u_i - n_i} \equiv \mathcal{O}(G) \tag{2.9}$$

where we have introduced the order $\mathcal{O}(G)$ and omitted a proportionality constant independent of q. In Appendix A.2, we discuss ways of enumerating the leading order diagrams. As a general rule, since the total number of contractions $\sum_i n_i$ is fixed, we should retain in (2.7) only the diagrams that maximize the total number of T- and U-loops.

A natural approximation at large q is to treat the elements of U as independent Gaussian random variables, so that a standard Wick theorem applies. This approximation corresponds to including all diagrams where all U-loops are of unit length, and omitting all others. We refer to this set as the Gaussian diagrams. As an example, in Fig. 2.4, the first and fourth diagrams on the right hand side are Gaussian. For these diagrams, Eq. (2.9) holds with proportionality constant one; therefore counting the overall number of U- and T-loops is sufficient to obtain the leading contribution of the diagram.

In this section, the leading contributions to all quantities calculated (except for the autocorrelation function of a local observable for $t > 0$) are Gaussian. A procedure that goes beyond the Gaussian approximation is necessary, firstly, for the proof of this statement, and secondly, for future discussion of the sub-leading contributions. Since the number of diagrams contributing to each of the quantities we consider is finite at fixed L and t, our results are exact in the limit $q \to \infty$ with L, t fixed.

2.4 Diagrammatic evaluation of results

We now show how this diagrammatic approach can be used to generate the results given in Sec. 2.2. We sketch the main ideas here, deferring formal proofs to Appendix A.

2.4.1 Spectral form factor

Consider the spectral form factor $K(t)$ introduced in Eq. (1.18). Applying the procedure described in Sec. 2.3 (and generalising the example given for $L = 2$ and $t = 2$ in Fig. 2.4), we obtain for $L > 2$ a many-body diagram consisting of single-site diagrams as shown in Fig. 2.6a. Here each timestep in $W(t)$ contributes with two unitaries, leading to $4t$ dots divided into four types – blue or red, and empty or filled.

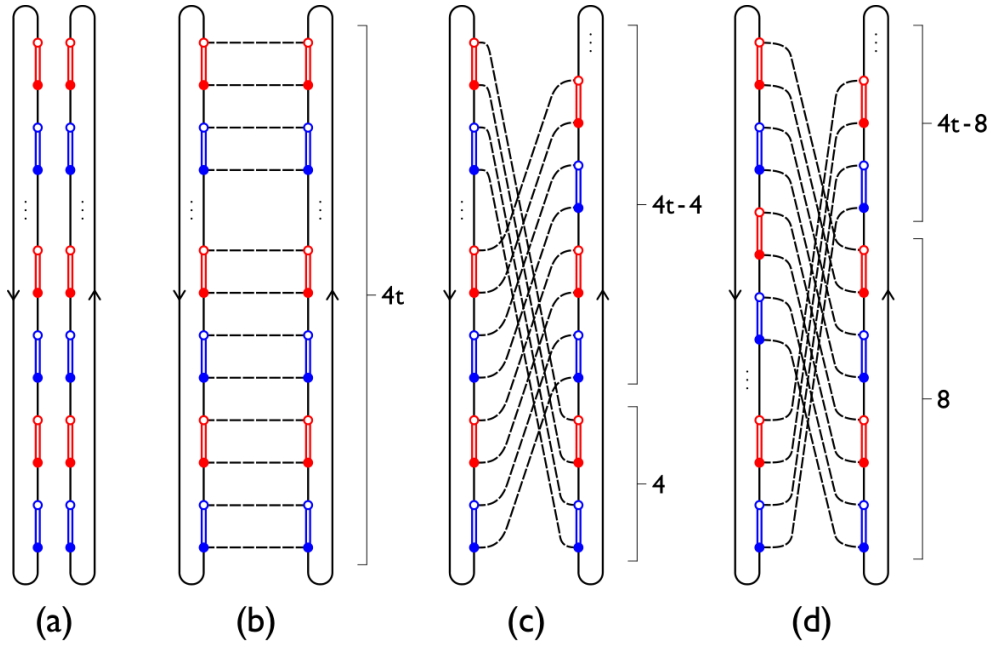


Figure 2.6: (a): The site diagram associated with $\mathrm{Tr}[W(t)]\mathrm{Tr}[W^\dagger(t)]$. It is colour coded as follows: for an odd site i, the blue dots and double lines are contributions from $U_{i,i+1}$ or $U^\dagger_{i,i+1}$ and the red ones are from $U_{i-1,i}$ or $U^\dagger_{i-1,i}$. For an even site, this coding is reversed. (b), (c) and (d): Three examples from a total of t leading order diagrams for $K(t)$ at $t > 0$.

Next we consider ensemble-averaging this diagram, making all possible contractions. On a single site, one can easily check that one of the diagrams with the maximum number of loops is, for example, the site diagram in Fig. 2.6b. Since this diagram is Gaussian and $\tau_i = u_i = 2t$ and $n_i = 4t$, its contribution for large q is simply 1. There are t equivalent diagrams of this kind, obtained by cyclically shifting the right dots with respect to the left ones, as shown in Fig. 2.6c and Fig. 2.6d. Additionally, once

one of these configurations has been chosen on the site i, the bond constraint forces all other sites to be in the same configuration in order to maximise the number of loops. All other diagrams are smaller by powers of q for $q \to \infty$. In consequence we get the result $K(t) = |t|$. A proof of this statement is given in Appendix A.3.

2.4.2 Relaxation of local observables

Contributions to the autocorrelation function $\mathrm{tr}\,[O(x,t)O(x)]$ are generated by contractions of the site diagrams shown in Fig. 2.7a and 2.7b. The leading contribution G_i at a site $i \neq x$ is from a contraction of the form shown in Fig. 2.7c. However, if this contraction is made at every site $i \neq x$, then because of the bond constraint it also applies at site x and yields $\mathcal{A}(G_x) \propto \mathrm{Tr}\, O_x = 0$ in Fig. 2.7d. An example of an alternative contraction, for which $\mathcal{A}(G_x) \neq 0$, is shown in Fig. 2.7e. With such a choice at $i = x$, the bond constraint imposes contractions at nearby sites $i \neq x$ that are sub-leading in q.

We have also (symbolically) computed the leading non-zero contributions to the autocorrelation function for large q at small values of t. We find

$$\langle [O(x,t)O(x)]_{\mathrm{av}} \rangle = \begin{cases} 1 & \text{for } t = 0 \\ 0 & \text{for } t = 1\,. \\ q^{-7} & \text{for } t = 2\,. \\ 16q^{-11} & \text{for } t = 3\,. \end{cases} \tag{2.10}$$

These results are interesting for two reasons. First, the equivalent quantity for time evolution with a random unitary circuit is identically zero at all $t \neq 0$. The results hence expose a difference between our Floquet model and random unitary circuits. The finite relaxation rate at finite q in the Floquet model is consistent with expected generic behaviour, whereas complete relaxation for any $t \neq 0$ is likely to

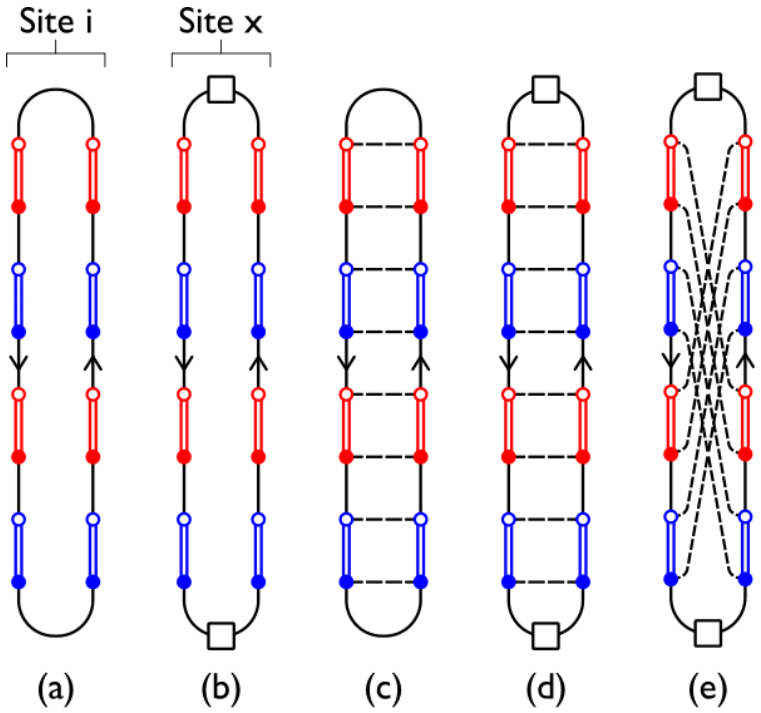


Figure 2.7: (a) and (b): Site diagrams associated with $[O(x, t{=}2)O(x)]_{\rm av}$ at sites $i \neq x$ and sites $i = x$ respectively. Color coding is as in Fig. 2.6 . (c): The leading contraction of the site diagram for $x \neq i$. (d) and (e): Two alternative contractions of the site diagram for $[O(x, t{=}2)O(x)]_{\rm av}$ at site x. (d) gives a contribution $\mathcal{A}(G_x) \propto \mathrm{Tr}\, O_x = 0$. (e) has $\mathcal{A}(G_x) \neq 0$ but forces similar contractions on adjacent sites via the bond constraint, and these vanish as $q \to \infty$.

be a special feature of random unitary circuits. Second, and quite separately, the dominant contributions arise from non-Gaussian diagrams: for example, at $t = 3$ the largest Gaussian term is $2q^{-9}$, but is cancelled by non-Gaussian contributions.

2.4.3 Purity and Rényi entropies

We now show that the large-q calculation of the purity can be reduced to counting domain wall (DW) configurations with positive weights, in a problem analogous to one from classical statistical mechanics. Related ideas apply (albeit more elaborately) to the evaluation of averages of the exponential of the Rényi entropy $S_\alpha(t)$ for general positive integer α and we discuss the case $\alpha = 3$ in Appendix A.6. Domain structure similar to what we derive here also appears in recent treatments of random unitary

circuits [**?**, **?**] and it is striking to find it as an emergent property of our Floquet model.

The main steps in our procedure are summarised in Fig. 2.8. We wish to average $\mathrm{Tr}_A\left[\rho_A(t)^\alpha\right]$ for $\alpha = 2$. Using the conventions of Fig. 2.1, Eq. (1.32) has the pictorial representation shown in Fig. 2.8a. Since each $\rho_A(t) = W^\dagger(t)\left|\psi\right\rangle\left\langle\psi\right|W(t)$, we have four sectors, containing $W(t), W^\dagger(t), W(t)$ and $W^\dagger(t)$ respectively. It is convenient to fold this diagram, as discussed in Sec. 2.3 and Fig. 2.1. This procedure leads to a folded representation containing four layers, as shown in Fig. 2.8b top. The folded site diagrams in regions A and B are shown in Fig. 2.8b bottom left. Note in particular how the timelines of sites in the regions A and B connect differently at the top of these diagrams, because of the structure of traces in (1.32). After averaging, it turns out that the leading contributions come from contractions of the U's and $U^\dagger$'s that are brought to lie in a stack on top of each other by the folding operation. We call a contraction of this type *local*. Such a stack of unitaries is indicated with a large blue box in Fig. 2.8b top. In the evaluation of the purity (where two U's and two $U^\dagger$'s are involved) there are two possible local contractions (Fig. 2.8b bottom right).

An intuitive explanation of the fact that only local contractions contribute for $q \to \infty$ is that any contraction between two dots in distant blocks would necessarily lead to a longer loop; as the total loop length is fixed, this implies a smaller number of loops and a lower order according to (2.9). This statement is proved in Appendix A.5.

Given the restriction to local contractions, a further simplification of the diagrammatic representation is possible. It is no longer necessary to represent the unitaries within a stack individually. Instead we can simply depict the stack, using a label to indicate the type of local contraction. We label the two types of local contraction that appear in a calculation of the purity A and B, because they involve the same types of pairing as are induced by the trace structure in regions A and B

of the system. The diagrammatic notation applied to one stack is shown in Fig. 2.8b bottom right. The same notation is used for a larger system in Fig. 2.8c.

We prove in Appendix A.5 that the order of a diagram with only local contractions is given by $q^{-h_{AB}}$, where h_{AB} is the number of segments of horizontal wall of length one lattice unit between an A and a B block. Such walls are shown with horizontal red lines in Fig. 2.8c. In this framework, the problem of finding the leading contributions admits a simple geometrical interpretation: they are represented by the set of minimal-length DW diagrams that separate the A and B contractions. Given the fixed boundary conditions for the blocks on the top of the diagram, a DW must connect the top centre to either the side or the bottom of the diagram (Fig. 2.8c).

For $t \leq L/4$, a minimal-length DW can only connect the top centre to the bottom edge of the diagram. Since there are a total of $2t$ rows, the minimal h_{AB} is $2t$, and the order is q^{-2t}. Moreover, there are two choices (for the DW to go left or right) below every row, so the number of leading order diagrams is 2^{2t}. For $t > L/4$, the lengths of the DW-s are minimized when they connect the top centre and the side of the diagram with the shortest possible paths. This implies that there are only two leading order diagrams: those where the DW is directed exclusively towards either the left or the right. For these cases, $h_{AB} = L/2$ and the order is $q^{-L/2}$.

In summary, Gaussian diagrams give the leading behaviour at large q:

$$\langle e^{-S_2(t)} \rangle \sim \begin{cases} 2^{2t} q^{-2t} & t \leq L/4 \\ 2q^{-L/2} & t > L/4 \end{cases} . \tag{2.11}$$

Subleading terms eliminate the discontinuity in (2.11) at $t = L/4$. For larger α, one can repeat the construction of Fig. 2.8. Each block has now $\alpha!$ possible states, corresponding to the possible local contraction inside a block of α U's and α $U^\dagger$'s. So, generically the problem reduces to counting, but for large α the procedure quickly becomes problematic. The case $\alpha = 3$ is discussed in Appendix A.6.

2.4.4 Out-of-time-order correlator

Consider the diagrammatic representation of the OTOC defined in Eq. (1.29). After the cancellation of Us with $U^\dagger$s wherever possible, we can distinguish two alternative scenarios. For $t < |x-y|/2$, all the unitary matrices are cancelled and we simply have $\mathrm{tr}[O(x,t)O(y)O(x,t)O(y)] = \mathrm{tr}(O(x)^2)\mathrm{tr}(O(y)^2) = 1$, independently of the realisation. Substituting the OTOC in (1.29), we see that the commutator vanishes. This is consistent with the fact that the light-cone spreading from x with velocity $v = 2$ has not yet reached the operator in y. Conversely, for $t \geq |x-y|/2$ there is a region of unitary operators that cannot be cancelled.

Calculation of the OTOC for $t \geq |x-y|/2$ is shown in Fig. 2.9 left using a folded diagram. The diagram contains four layers of Ws, as for the purity, and we employ the block representation introduced in Sec. 2.4.3. Similarly to Sec. 2.4.3, it can be shown that the leading order diagrams necessarily involve only local contractions. Moreover, the trace structure of OTOC sets boundary conditions along the top of the diagram that act as A-blocks, and along the bottom that act as B-blocks. From this one would expect that the leading order diagrams are minimal-length DWs that cross the diagram horizontally, separating an upper domain of As from a lower domain of Bs (Fig. 2.9 right). These diagrams however vanish, because they involve factors of either $\mathrm{tr}\, O(x) \equiv 0$ or $\mathrm{tr}\, O(y) \equiv 0$. In Appendix A.7, we prove that the leading contributions to the OTOC for $t \geq |x-y|/2$ go to zero for $q \to \infty$, and hence Eq. (2.4) is recovered in the large-q limit.

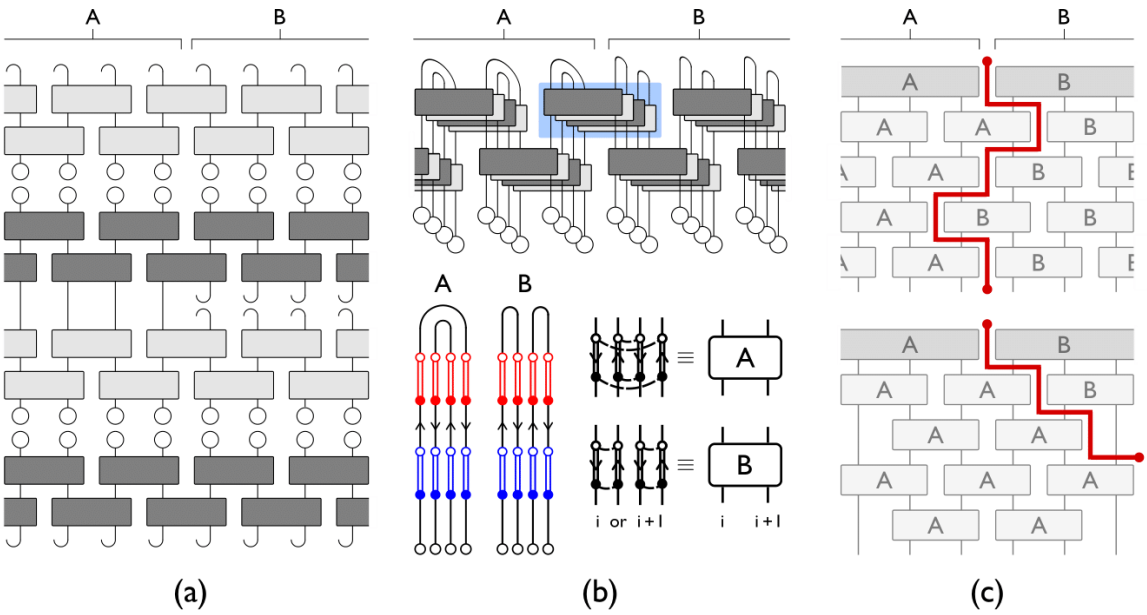
2.5 Discussion and outlook

In summary, we have introduced a minimal random-matrix model with extended spatial structure to study the chaotic Floquet dynamics of a many-body quantum system. We have presented a diagrammatic technique to compute several quantities

using a systematic and controlled expansion in the inverse of the local Hilbert space dimension q. There are some obvious and interesting directions for additional investigations using the techniques we have set out. First, in contrast with random unitary circuits, our model has a well-defined Floquet operator, opening the possibility for the study of its spectral properties. It seems likely that further work in this direction will be useful, going beyond our evaluation of the spectral form factor in the random matrix regime. Second, the results we have presented are averages over an ensemble of systems. It would be useful to understand the magnitude of sample-to-sample fluctuations, by evaluating quantities such as $\langle (e^{-S_\alpha(t)})^2 \rangle - \langle e^{-S_\alpha(t)} \rangle^2$. More ambitiously, it would be appealing to use higher order terms in the $1/q$ expansion to search for the expected differences between the naive light-cone velocity, the entanglement-spreading velocity and the butterfly velocity, and to investigate broadening of the step in the OTOC given in (2.4) for the large-q limit.

There are also several generalisations. Our model and the techniques we have developed can be naturally extended to higher dimensions. Analogous models could also be developed for the other symmetry classes in random matrix theory. In the context of quantum transport, it would be interesting to incorporate the presence of conserved quantities, by modifying the local structure of the Floquet operator, as has been done recently for random quantum circuits [**?**, **?**].

Finally, and speculatively, it is possible that an understanding of the ergodic phase in our model for chaotic many-body systems may play a role analogous to the treatment of a diffusive metal in the theory of disordered conductors, and provide a starting point for a theory [**?**] of the many-body localisation transition. [**?**]


A
B
A
B
A
B

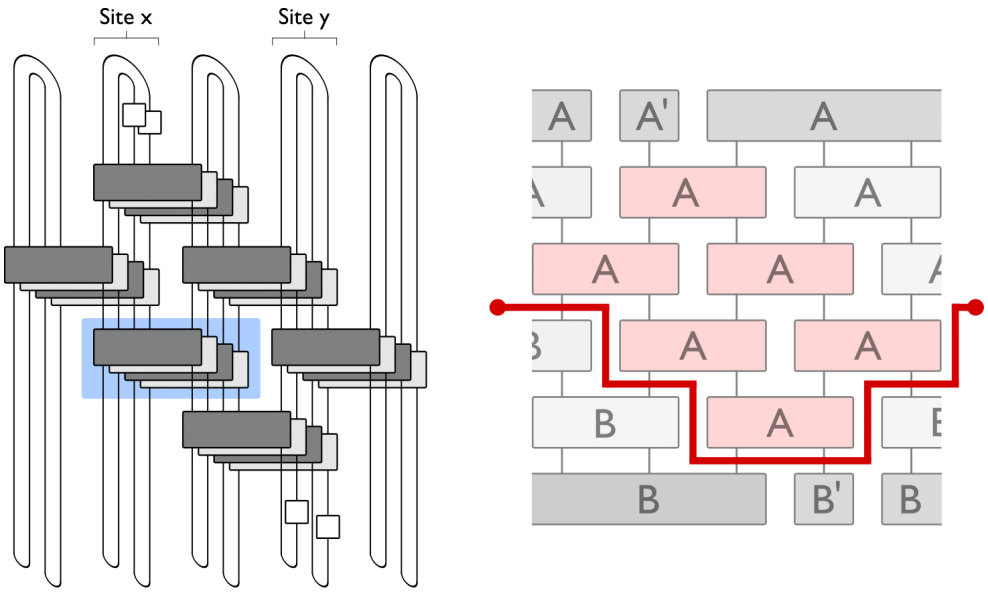


Figure 2.9: Diagrammatic representation of OTOC. Left: Folded diagram for $\mathrm{tr}[O(x,t)O(y)O(x,t)O(y)]$ with $|x-y| = 2$ and $t = 2$. The blue box highlights four unitary operators, which can be represented in the block representation in a similar way to the ones in Fig. 2.8c. Right: An apparent minimal-length horizontal DW diagram that vanishes due to $\mathrm{tr}\, O(y) \equiv 0$. The red blocks are unitary pairs that can not be annihilated. The dark grey blocks represent the boundary conditions. A' represents an effective contraction A (Fig. 2.8c) with operators along the loops, and similarly for B'.

Chapter 3

Spectral statistics of quantum chaotic many-body systems

3.1 Introduction

Spatially extended systems with local Hamiltonians offer a context in which it is natural that there should be limits on the applicability of RMT, since the combination of spatial structure and locality implies a preferred basis in Hilbert space, which is explicitly excluded from the theory. This is well understood for single-particle models of mesoscopic conductors in the diffusive regime. Here, characteristic scales are set by the Thouless time t_{Th}, the time taken for a particle to explore the accessible phase space, and its energy counterpart $E_{\mathrm{Th}} \equiv \hbar/t_{\mathrm{Th}}$ [**?**]. With diffusion constant D and linear size L, the time for a particle to cross such a system is L^2/D, so that $E_{\mathrm{Th}} = \hbar D/L^2$. An energy window of width E_{Th} contains many levels in a large system with dimension $d > 2$, since the spacing between energy levels varies as L^{-d}. Spectral statistics follow RMT on scales much smaller than E_{Th}, but have a different (although also universal) form on scales much larger than E_{Th} [**?**].

The aim in this chapter is to examine how spectral statistics are influenced by spatial dimension and system size in chaotic many-body systems with interactions that are local in space. We treat Floquet systems, both because they are convenient for our approach and because their lack of locally conserved densities is expected to result in particularly simple dynamics [**?**, **?**]. In the spirit of RMT, we study models drawn from an ensemble and compute their average properties. We treat systems without time-reversal symmetry. Important complementary results have been obtained recently for time-reversal symmetric systems within the framework of periodic orbit theory [**?**], while previous numerical work [**?**] on the ergodic phase in weakly disordered spin chains has identified a Thouless time growing with system size.

The focus of our discussion is the behaviour of the SFF (1.18) associated with the Floquet operator W, which generates time evolution over one cycle for a periodically driven quantum system. The SFF is related to the Floquet operator via

$$K(t) = \langle [\mathrm{Tr}\, W(t)][\mathrm{Tr}\, W^{\dagger}(t)] \rangle \,, \tag{3.1}$$

where we use $W(t)$ to denote the t-th power of W. For a system without spatial structure or time-reversal symmetry, W is modelled by the CUE, which is an ensemble of random unitary $N \times N$ matrix drawn from the Haar distribution. The SFF averaged over the CUE is given in Eq. (1.19). The linear variation of $K(t)$ with t for $0 < t \leq N$ is a consequence of spectral rigidity, and the saturation time $t = N$ is set by the inverse level spacing.

We define the Thouless time to be the time-scale beyond which $K(t)$ has RMT form. Consider a many-body system consisting of L^d chaotic grains with Hilbert space dimension q for each grain. If the grains are uncoupled one has $K(t) = t^{L^d}$ for $0 < t \leq q$. If the grains are weakly coupled it is natural to expect that the

coupling is effective only at long times, so that $K(t) \gg t$ for $0 < t \ll t_{\rm Th}$ and $K(t) = t$ for $t_{\rm Th} \ll t \leq q^{L^d}$, as illustrated in Fig. 1.11. In the following we define a simple model of this kind, show that it exhibits just this behaviour, and determine the dependence of $t_{\rm Th}$ on dimension and system size. We use analytical calculations for large q and general d, and numerical simulations for small q and $d = 1$. We also present qualitative arguments in support of the idea that our main results are generic.

We study the FRPC defined in Eq. (1.36). This model is distinguished from the FRUC defined in Eq. (1.35) and discussed in Ch. 2 in having two separate parameters: The single-site Hilbert space size q and the variance ε of the diagonal phases in Eq. (1.37). This brings the advantage for analytical work that one can use large q to control calculations, but retain variable coupling between sites [1]. Sites are independent for $\varepsilon = 0$ and are maximally coupled for $\varepsilon \gg 1$. It is natural to expect two phases: a many-body localised (MBL) phase [**?**, **?**, **?**, **?**] for $\varepsilon < \varepsilon_c(q)$ and an ergodic phase [**?**] for $\varepsilon > \varepsilon_c(q)$. We are concerned here with behaviour in the ergodic phase; we believe (see below) that in one dimension: (i) $\varepsilon_c(q) \to 0$ as $q \to \infty$, (ii) the model is MBL for all ε at $q = 2$, and (iii) $\varepsilon_c(3) \approx 0.25$. In numerical studies of the ergodic phase we use $q = 3$ and $\varepsilon = 1$.

3.2 Mapping to the classical Potts model

It is possible to evaluate $K(t)$ exactly for fixed t and ε in the limit $q \to \infty$, via a mapping to a Potts model. Here we first summarise the results and then we present the derivation. In one dimension (with periodic boundary conditions) we find

$$K(t) = (t-1)(1-e^{-\varepsilon t})^L + [1 + (t-1)e^{-\varepsilon t}]^L \,. \tag{3.2}$$

[1] Behaviour at times $t < t_{\rm Th}$ in the FRUC is hard to access as it is sub-leading in a $1/q$ expansion.

This form can be simplified in the regime of most interest, $t \gg 1$ and $L \gg 1$, giving

$$K(t) \sim \begin{cases} t^{L/\xi(t)} & t \ll t_{\rm Th} \\ t & t \gg t_{\rm Th}\,, \end{cases} \tag{3.3}$$

with

$$\xi(t) = \frac{\ln t}{\ln[1+(t-1)e^{-\varepsilon t}]} \sim \frac{\ln t}{t} e^{\varepsilon t} \tag{3.4}$$

(where the asymptotic form is for $e^{\varepsilon t} \gg t$) and

$$t_{\rm Th} = \frac{\ln L}{\varepsilon}\,. \tag{3.5}$$

The behaviour of $K(t)$ at times $t \ll t_{\rm Th}$ has a clear interpretation: the spectral fluctuations are the same as if the system consisted of $L/\xi(t)$ uncoupled pieces. The size $\xi(t)$ of each piece diverges very rapidly with t, and the Thouless time $t_{\rm Th}$ is the time at which $\xi(t)$ reaches the system size L.

In higher dimensions $d > 1$, we obtain for $t \gg 1$ and $\varepsilon \ll 1$ (but εt arbitrary)

$$K(t) = \begin{cases} (te^{-d\varepsilon t})^{L^d} & t \le t_{\rm Th} \\ t & t \ge t_{\rm Th} \end{cases} \tag{3.6}$$

where the Thouless time is the larger of the two solutions to $t_{\rm Th}e^{-d\varepsilon t_{\rm Th}} = 1$. Hence for $d > 1$ there is a fixed value for $t_{\rm Th}$, which is independent of system size and is large if the inter-site coupling ε is small.

We now turn to the derivation of our analytic results, Eqns. (3.3–3.6), which are based on an evaluation of Eq. (3.1) for the FRPC in Eq. (1.36)at large q. Consider first the average on W_1, and in particular, the Haar unitary U_n at site n. The factors

involved have the form

$$\begin{aligned}\big\langle [U_n]_{a(1),a(2)} [U_n]_{a(2),a(3)} \dots [U_n]_{a(t),a(1)} \times \\ \times [U_n]^*_{b(1),b(2)} [U_n]^*_{b(2),b(3)} \dots [U_n]^*_{b(t),b(1)} \big\rangle \,.\end{aligned} \tag{3.7}$$

The leading contributions to this average are the ones in which the indices $b(1), b(2) \dots b(t)$ are a cyclic permutation of the indices $a(1)$, $a(2) \dots a(t)$ [**?**, **?**, **?**]. Their average at leading order is q^{-t}; corrections and other contributions are smaller by inverse powers of q. In the large-q limit we hence need to consider only these cyclic permutations, which can be specified by the relative shift s, with $a(r) = b(r+s)$ for $r = 1, 2 \dots t$, where r and $r+s$ are counted mod t. Summing over values for $\{a(r)\}$ at fixed s generates a factor of q^t, cancelling the factor of q^{-t} from the average. The shift takes the values $s = 1, 2 \dots t$ and serves to label at each site the dominant contributions that remain after averaging on W_1.

Next consider the average on W_2, and specifically the contributions to the phase in (1.37) arising from a particular pair of neighbouring sites, n and n', for the leading terms that are selected via the average on W_1. Denoting indices on U_n by $a(r)$ and those on $U_{n'}$ by $a'(r)$, and the shifts by s and s', this phase contribution is

$$\Phi_{n,n'} = \sum_{r=1}^{t} \big(\varphi_{a(r),a'(r)} - \varphi_{a(r+s),a'(r+s')} \big) \,. \tag{3.8}$$

For $s = s'$, terms cancel in pairs and $\Phi_{n,n'}$ vanishes. Conversely, for $s \neq s'$ at large q and fixed t, all except a fraction $\mathcal{O}(q^{-1})$ of the possible assignments for $\{a(r)\}$ and $\{a'(r)\}$ leave $2t$ independent terms in $\Phi_{n,n'}$. As a result, $\langle e^{i\Phi_{n,n'}} \rangle$ has the value 1 if $s = s'$, and $e^{-\varepsilon t}$ if $s \neq s'$.

Combining these results, we see that $K(t)$ at large q is given *exactly* by the partition function of a classical t-state ferromagnetic Potts model, on the same lattice as in the original many-body quantum system. This partition function is a sum over

configurations in which the shifts at each site independently take one of t possible states, with factors in the 'Boltzmann weight' from each coupled pair of sites that are 1 or $e^{-\varepsilon t}$, according to whether the sites of the pair are in the same or different states.

In $d = 1$ it is straightforward to evaluate the partition function using a transfer matrix, yielding Eq. (3.2). For $d > 1$, we note that the main interest is in behaviour at $t \gg 1$ and that the t-state ferromagnetic Potts model in $d > 1$ has an ordering transition that is strongly discontinuous at large t [**?**]. In the disordered phase ($e^{-\varepsilon t}$ close to 1) the state of each site fluctuates almost independently of its neighbours, while in the ordered phase nearly all sites occupy the same state. The two phases give the two contributions to Eq. (3.6).

3.3 Numerical results

As mentioned above, since the model is in the MBL phase for all ϵ at $q = 2$ (see Appendix B.2), the numerical studies of the ergodic phase is studied at $q = 3$. Our numerical results for $q = 3$ are obtained with three complementary methods. We use (i) exact diagonalisation (ED) of W to obtain $K(t)$ at all t for $L \leq 6$. Since it is faster to act with the quantum circuit on a vector than it is to do ED, there are alternatives that can treat larger systems. We use: (ii) Monte Carlo (MC) to compute $\mathrm{Tr}\, W(t)$ by evaluating $\langle u|W(t)|u\rangle$ for randomly chosen vectors $|u\rangle$, giving access to $L \leq 10$ at times of most interest ($|t| \leq 500$); and (iii) a transfer matrix (TM) acting in the space direction, giving access to very large systems ($L \leq 100$) but only for short times ($|t| \leq 14$). With each method we average over a large number $\mathcal{N}$ of realisations: $\mathcal{N} \sim 10^5$ for ED; $\mathcal{N} \sim 10^6$ for MC; $\mathcal{N} \sim 10^3$ for TM. Our numerical results for $q = 2$ are obtained using ED with $\mathcal{N} \sim 10^5$.

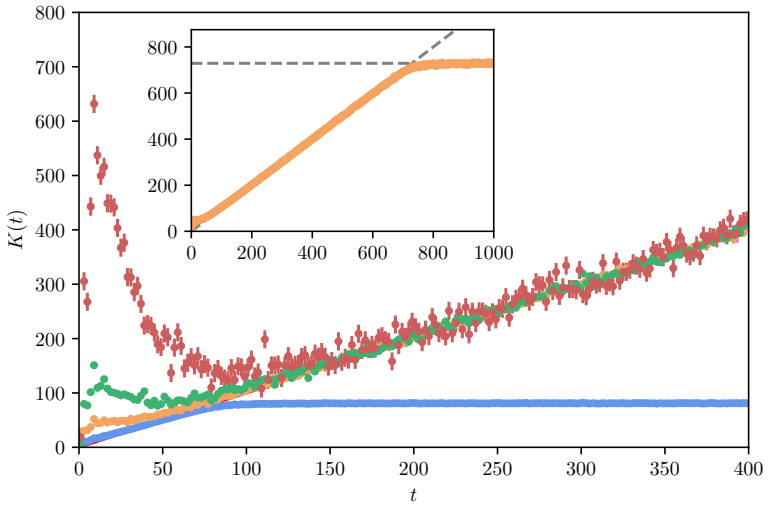


Figure 3.1: $K(t)$ at small t, showing deviations from RMT form that grow with L. Data for $L = 4$, 6, 8 and 10 (from bottom to top). Inset: $K(t)$ vs t for $L = 6$.

The behaviour of $K(t)$ is shown in Fig. 3.1 for $q = 3$, $\varepsilon = 1$ [2]. The inset gives an overview of how $K(t)$ approximates the RMT form given in Eq. (1.19). Departures from this are largest at early times and grow with increasing system size, as illustrated in the main panel of Fig. 3.1. To interpret these deviations, we adapt Eq. (3.4) to finite system size and express spectral fluctuations in terms of the length scale $\xi_L(t) = (L \ln t)/\ln K(t)$. As we demonstrate in Fig. 3.2, $\xi_L(t)$ appears to be independent of L at times sufficiently short that $\xi_L(t) \ll L$. It grows rapidly with increasing t and saturates at $\xi_L(t) = L$ for t large (but less than q^L). The timescale for saturation is the Thouless time; it increases rapidly with L over the available range of system sizes. We believe these numerical results provide a good indication that qualitative behaviour throughout the ergodic phase in $d = 1$ is similar to what we have obtained analytically at large q, although (as we discuss below) the specific functional form of $\xi_L(t)$ in Fig. 3.2 appears not to be very close to that in Eq. (3.4).

[2] $K(t)$ shows small period $\Delta t = 2$ oscillations. In Fig. 3.1 we display data only for odd t. Even-t data show similar results. Both sets are included in Fig. 3.2.

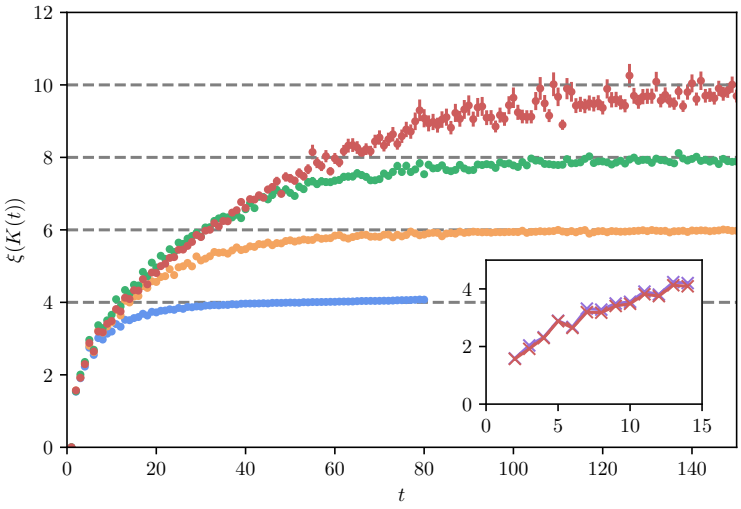


Figure 3.2: $\xi_L(t)$ vs t. Main panel: $L = 4$, 6, 8 and 10 (from bottom to top). Inset: $L = 10$ (red) and $L = 100$ (purple) at short times.

We close with a discussion of the phase diagram of the model as a function of ε for $q = 2$ and 3. We use the well-established diagnostic computed from the ratio of eigenphase spacings: let θ_{n-1}, θ_n and θ_{n+1} be three successive eigenphases, and define $r = \min\{\theta_n - \theta_{n-1}, \theta_{n+1} - \theta_n\}/\max\{\theta_n - \theta_{n-1}, \theta_{n+1} - \theta_n\}$ [**?**]. Then $\langle r \rangle$ takes different characteristic values in the two phases. In Fig. 3.3, we provide clear numerical evidence for a critical point at $\varepsilon_c(q = 3) \approx 0.25$. For $q = 2$, behaviour of $K(t)$ and $\langle r \rangle$ (see Appendix B.2) indicate that there is only an MBL phase.

The behaviour of $K(t)$ is quite different in the MBL phase. Whereas in the ergodic phase $K(t)$ reaches its limiting value of q^L at a time $t = q^L$ set by the inverse level spacing, in the MBL phase $K(t)$ approaches q^L at a time that remains finite as $L \to \infty$ (see Appendix B.2).

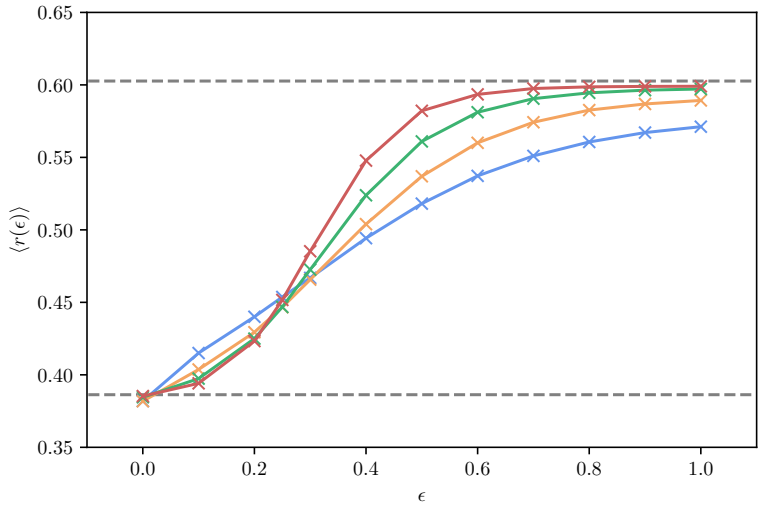


Figure 3.3: Identification of MBL and ergodic phases: $\langle r \rangle$ vs ε for $q = 3$ with system sizes $L = 4, 5, 6, 7$. Upper and lower horizontal lines indicate the values expected in an ergodic [**?**] and an MBL phase [**?**], respectively.

3.4 Discussion and outlook

An important question is whether this large-q behaviour describes more broadly ergodic many-body Floquet systems without time-reversal symmetry. We believe that our solution in fact suggests an appealing and potentially general picture, as follows. Note first that an expansion of $[\mathrm{Tr}\, W(t)][\mathrm{Tr}\, W^\dagger(t)]$ can be expressed for general W as a sum over terms arising from the product of two t-step orbits in the space of many-body states, one from expansion of $\mathrm{Tr}\, W(t)$ and the other from $\mathrm{Tr}\, W^\dagger(t)$. Contributions in which one orbit is a cyclic permutation of the other are always real and positive, while other contributions may have any phase. It is therefore natural to anticipate that orbits paired in this way will dominate under many circumstances. Just as with periodic orbit theory for the quantisation of low-dimensional chaotic systems [**?**], or diffusons in mesoscopic conductors [**?**], we expect these paired orbits to give the RMT form for $K(t)$ at $t < N$.

In a spatially extended system, a clear alternative to a global pairing of orbits is that orbits are locally paired in this way, but with a cyclic permutation that varies between regions separated by domain walls. The simplifying features of our model at large q make this picture exact and restrict domain walls to run only in the time direction. A more general treatment should include local disruptions to the pairing, and domain walls with locations that fluctuate in both space and time. Equivalence to a t-state Potts model may survive if these additional fluctuations are not qualitatively important, and provided the statistical cost of domain walls remains proportional to their $d-1$ dimensional area.

Domain walls between pairings, similar to the ones we discuss here, have been proposed previously in discussions of entanglement spreading in random unitary circuits [**?**, **?**, **?**], and an equivalent construction emerged in our study of entanglement in Floquet systems in Sec. 2.

While the spirit of our approach and aspects of our results have much in common with a recent evaluation [**?**] of $K(t)$ for a Floquet spin chain using periodic orbit theory, there are also important differences. In particular, the significance of locality and dimensionality, and the notion of domain walls separating different pairings of cycles seem specific to the present work. The logarithmic scaling of the Thouless time obtained in [**?**] appear via a different mechanism, which in outline is as follows. Periodic orbit theory yields $K(t) = (2t/\beta)\sum_a P_{aa}(t)$ for $0 < t \ll N$, where $\beta = 1$ or 2 in systems with or without time-reversal symmetry. Here $P_{ab}(t)$ is the probability within the diagonal approximation for propagation in t time steps between states a and b from the many-body Hilbert space. It is given by $P_{ab}(n) = [T^n]_{ab}$ with $T_{ab} = |W_{ab}|^2$. Let the eigenvalues of T be $\lambda_1, \lambda_2 \ldots$, with $|\lambda_1| \geq |\lambda_2| \geq \ldots$. Unitarity of W ensures that $\lambda_1 = 1$. RMT behaviour follows if $\lambda_2 = 0$, and the corrections of [**?**] arise because the subleading eigenvalues of T are not zero. In our model $\lambda_2 \sim \mathcal{O}(q^{-1})$ and so corrections of this type are absent for $q \to \infty$. We note that corrections to

RMT similar to those of Ref. [**?**] have recently been found in the SYK and other models [**?**]; we think it is likely that they arise by the same mechanism as in [**?**], which (in contrast to ours at large q) is dimension-independent.

By contrast, many-body systems with a locally conserved density that relaxes diffusively with diffusion constant D are expected [**?**, **?**] to have $t_{\rm Th} \sim L^2/D$, as in the singe-particle case. We expect ergodic time-independent Hamiltonians to belong to this category, in consequence of their conserved energy density.

The exponential divergence of $\xi(t)$ with t at large q is apparently more rapid than the growth shown for $q = 3$ in Fig. 3.2. We expect at finite q that rare weak links in a disordered one-dimensional system [**?**] change the growth of $\xi(t)$ at long times from exponential to power-law. A weak link arises in our model between sites n and $n + 1$ if the coupling phase $\varphi_{a_n,a_{n+1}}$ has approximately the separable form: $\varphi_{a_n,a_{n+1}} = \tilde{\varphi}_{a_n} + \tilde{\varphi}_{a_{n+1}} + \mathcal{O}(\delta)$. This condition imposes $(q-1)^2$ constraints on the entries of $\varphi_{a_n,a_{n+1}}$. It is therefore satisfied in the ensemble to an accuracy $\delta \ll 1$ with probability $\propto \delta^{(q-1)^2}$. We expect the value of δ^2 will play a similar role to that of ε in Eq. (3.2), so that links of strength δ are ineffective until a time $t \sim \delta^{-2}$, implying $\xi(t) \lesssim t^{(q-1)^2/2}$ for large t. This upper bound is compatible with our analytical results, since the exponent diverges for $q \to \infty$. The bound appears to rise faster with t than our data at $q = 3$, indicating either large finite-size effects or the existence of another, more effective, mechanism for the formation of weak links.

A number of important points remain open. First, it is unclear how or whether our definition of a Thouless energy in terms of the spectral form factor is related to alternative definitions involving properties of matrix elements [**?**, **?**, **?**, **?**]. Second, we expect that rare weak links in a disordered one-dimensional system [**?**] change the growth of $\xi(t)$ at long times from exponential to power-law, and it would be interesting to investigate this in detail. More broadly, it will be valuable if the description of many-body quantum dynamics in terms of paired orbits can be developed further.

Chapter 4

Eigenstate correlation, thermalization and the butterfly effect

4.1 Introduction

The eigenstate thermalization hypothesis (ETH) links the properties of eigenvectors for many-body systems to statistical mechanics and the dynamics of equilibration [?, ?, ?]. It constitutes a widely accepted expression of the notion of ergodicity for many-body quantum systems [?, ?]. By design, the ETH omits any spatial structure present in the underlying system. Our aim in this chapter is to understand universal features of eigenfunction correlations in ergodic many-body systems that follow from spatial structure and lie outside the ETH.

A direct characterisation of the dynamics of quantum information is provided by the butterfly effect [?, ?, ?]. In the framework of quantum mechanics, this phenomenon concerns the influence of a perturbation induced by the operator $\hat{Y}$ on later measurements of $\hat{X}$. This is quantified by the value of the OTO commutator

$\mathcal{C}(\ell, t)$ defined in Eq. (1.29) with $\hat{O}(x,t) \equiv \hat{X}(t)$, $\hat{O}(y,0) \equiv \hat{Y}(0)$ and $\ell \equiv x - y$. An important recent insight [?] is that non-zero $\mathcal{C}(\ell, t)$ implies correlations in matrix elements of operators beyond those captured by the ETH. We show here that these correlations acquire a specific universal form for pairs of widely-separated local operators in spatially extended systems. Moreover, since the time-scale for propagation of quantum information is long when ℓ is large, these additional correlations may be arbitrarily sharp in energy, in contrast to those of the ETH.

We focus on Floquet systems because they constitute the simplest class. More generally, conservation laws are reflected in correlations at large distances and long times, and the simplest systems are ones with no conserved densities. To escape conservation of energy density, it is necessary to consider evolution with a time-dependent Hamiltonian, and for there to be a fixed evolution operator this time dependence should be periodic.

A convenient way to construct models with time-dependent evolution operators is by using unitary quantum circuits. These have yielded valuable insights into chaotic quantum dynamics both for systems with an evolution operator that is stochastic in time [?, ?, ?] and for Floquet systems [?, ?, ?]. In particular, these studies have confirmed the existence of two regimes for $\mathcal{C}(\ell, t)$, distinguished by the sign of $v_B|t| - \ell$, where the *butterfly velocity* v_B characterises the speed at which operators spread in space. We use Floquet random unitary circuits in the following for numerical simulations.

4.2 ETH and relaxation

We start by recalling the formulation of the ETH and its connection to the autocorrelation function of an observable. Consider a chaotic many-body Floquet system with local interactions and Hilbert space dimension N. Let $\hat{W}$ be the evolution

operator for one period, with eigenstates $|\alpha\rangle$ and eigenphases E_α. According to the ETH, the matrix elements of a local Hermitian operator $\hat{X}$ have the form [**?**]

$$X_{\alpha\beta} \equiv \langle\alpha|\,\hat{X}\,|\beta\rangle = \bar{X}\delta_{\alpha\beta} + N^{-1/2}h(\Delta_{\alpha\beta})R^X_{\alpha\beta} \tag{4.1}$$

where $\Delta_{\alpha\beta} = E_\alpha - E_\beta$ modulo 2π. In this expression, $\bar{X}$ is the value to which the expectation of $\hat{X}$ relaxes at long times [**?**, **?**, **?**], $h(\omega)$ is a smooth function of ω, and $R_{\alpha\beta}$ are Gaussian random variables with zero mean and unit variance, which are complex and independent for each pair $\alpha > \beta$, and real and independent for each $\alpha = \beta$. Hermiticity of $\hat{X}$ implies that $h(\omega)$ is real and symmetric, and that $R^*_{\alpha\beta} = R_{\beta\alpha}$. Without loss of generality, we consider traceless operators so that $\bar{X} = 0$. It is then useful to define

$$F(\omega) = N^{-1}\left\langle \sum_{\alpha\beta} |X_{\alpha\beta}|^2 \delta(\Delta_{\alpha\beta} - \omega) \right\rangle \tag{4.2}$$

with the eigenstate average $\langle\cdot\rangle$ either effected by broadening the delta function, or taken over an ensemble of statistically similar systems. Using (4.1) and the mean level spacing $\Delta = 2\pi/N$, we write $F(\omega) \equiv (2\pi)^{-1}h(\omega)^2$. $F(\omega)$ characterizes relaxation of the (integer t) autocorrelation function[1], since

$$[X(t)X]_{\rm av} = {\rm tr}[X(t)X] = \int_0^{2\pi} {\rm d}\omega\, e^{\imath\omega t} F(\omega) \equiv {\rm tr}[X^2] f(t)\,, \tag{4.3}$$

where the thermal average appropriate for a chaotic Floquet system is the infinite-temperature one, with $[\ldots]_{\rm av} = N^{-1}\,{\rm Tr}[\ldots] \equiv {\rm tr}[\ldots]$. Decay of the autocorrelation function on a microscopic relaxation timescale t_R is encoded in $f(t)$, which satisfies $f(0) = 1$ and $f(t) \to 0$ for $t \gg t_R$.

[1]The δ-function is smeared on the scale of level spacing, which is exponentially small in system size. So Eq. (4.3) is exact in the thermodynamic limit.

4.3 Generic form of four-point correlators

Let $\hat{X}$ and $\hat{Y}$ be local observables acting near the points x and y, with $\ell \equiv |x-y|$. In analogy with Eq. (4.2), we introduce the correlator of four matrix elements

$$G(\omega_1,\omega_2,\omega_3) = N^{-1}\Big\langle \sum_{\alpha\beta\gamma\delta} X_{\alpha\beta}Y_{\beta\gamma}X_{\gamma\delta}Y_{\delta\alpha} \\ \delta(\Delta_{\alpha\beta}-\omega_3)\delta(\Delta_{\beta\gamma}-\omega_2)\delta(\Delta_{\gamma\delta}-\omega_1)\Big\rangle . \quad (4.4)$$

If one assumes [following Eq. (4.1)] that the matrix elements of $\hat{X}$ and $\hat{Y}$ are uncorrelated random variables, then individual terms $X_{\alpha\beta}Y_{\beta\gamma}X_{\gamma\delta}Y_{\delta\alpha}$ are $\mathcal{O}(N^{-2})$ with random phase, and only the term $\alpha=\beta=\gamma=\delta$ survives the average in Eq. (4.4), implying $G(\omega_1,\omega_2,\omega_3)\sim\mathcal{O}(N^{-2})$. In fact, a sum rule shows that $X_{\alpha\beta}Y_{\beta\gamma}X_{\gamma\delta}Y_{\delta\alpha}$ has a coherent $\mathcal{O}(N^{-3})$ component, as well as $\mathcal{O}(N^{-2})$ fluctuations (see Appendix C.1 and also Ref. [**?**]). We will show that for large ℓ this coherent component is concentrated on the terms in which the two matrix elements of $\hat{X}$ (and also those of $\hat{Y}$) are between pairs of states with almost opposite eigenphase differences. Specifically, the condition for $X_{\alpha\beta}Y_{\beta\gamma}X_{\gamma\delta}Y_{\delta\alpha}$ to make a large contribution to $G(\omega_1,\omega_2,\omega_3)$ is that $(E_\alpha-E_\beta)\approx -(E_\gamma-E_\delta)$, implying also $(E_\beta-E_\gamma)\approx-(E_\delta-E_\alpha)$.

To understand the form of $G(\omega_1,\omega_2,\omega_3)$ we switch to the time domain and consider the OTO commutator $\mathcal{C}(\ell,t)\equiv\frac{1}{2}\mathrm{tr}|[\hat{X}(t),\hat{Y}]|^2$ (see also Sec. 1.2.6.2), written as

$$\mathcal{C}(\ell,t) = \mathrm{tr}[\hat{Y}^2\hat{X}^2(t)] - \mathrm{tr}[\hat{X}(t)\hat{Y}\hat{X}(t)\hat{Y}] . \quad (4.5)$$

The second term on the right-hand side is the OTOC [**?**, **?**]. $\mathcal{C}(\ell,t)$ vanishes for short times t and large separations ℓ, while for large times the OTOC is small and $\mathcal{C}(\ell,t)$ approaches $\mathrm{tr}(\hat{X}^2)\mathrm{tr}(\hat{Y}^2)$. Correspondingly, the OTOC has the form $\mathrm{tr}[\hat{X}(t)\hat{Y}\hat{X}(t)\hat{Y}] = \mathrm{tr}(\hat{X}^2)\mathrm{tr}(\hat{Y}^2)k_\ell(\ell/v_B-|t|)$, where $k_\ell(\tau)$ steps between $k_\ell(\tau)=1$

for τ large and positive, and $k_\ell(\tau) = 0$ for τ large and negative. The width $\Delta\tau$ of the step satisfies $\Delta\tau \ll v_B\ell$ for large ℓ [**?**, **?**].

We want to connect this behaviour with the statistical properties of matrix elements. We start by introducing a generalised OTOC

$$\mathrm{tr}[X(t_3)Y(t_2)X(t_1)Y] \equiv \mathrm{tr}(X^2)\mathrm{tr}(Y^2)g(t_1,t_2,t_3)\,. \tag{4.6}$$

This reduces to the standard OTOC for $t_1 = t_3 \equiv t$ and $t_2 = 0$. We argue that the relation

$$g(t_1,t_2,t_3) \approx f(t_3{-}t_1)f(t_2)k_\ell(\ell/v_B{-}|t_1|) \tag{4.7}$$

holds for $\ell \gg v_B t_R$, where for simplicity we take the autocorrelation function $f(t)$ of $\hat{X}$ and $\hat{Y}$ to be the same.

A simple justification is as follows (for details, see Appendix C.2). We consider three regimes. In (i) $|t_2| \gg t_R$ and/or $|t_3 - t_1| \gg t_R$. In (ii) and (iii) $|t_2| \lesssim t_R$ and $|t_3 - t_1| \lesssim t_R$. In addition, in (ii) $\ell - v_B|t_1 - t_2| \gg \Delta\tau$, while in (iii) $\ell - v_B|t_1 - t_2| \ll -\Delta\tau$. In (i) the left side of (4.7) is zero because of scrambling (App. C.2), as is $f(t_3 - t_1)f(t_2)$ on the right side. In (ii) $[Y(t_2), X(t_1)]$ is small in norm and we are dealing with averages taken approximately simultaneously at x and y, which can be factorised. Hence $\mathrm{tr}[X(t_3)Y(t_2)X(t_1)Y] \approx \mathrm{tr}[X(t_3)X(t_1)]\mathrm{tr}[Y(t_2)Y]$ and $g(t_1,t_2,t_3) \approx f(t_3{-}t_1)f(t_2)$; since $k_\ell(\ell/v_B{-}|t_1|) = 1$ in (ii), Eq. (4.7) follows. In (iii) we can factorise $\mathrm{tr}[X(t_3)Y(t_2)X(t_1)Y] \simeq \mathrm{tr}[X(t_3)]\mathrm{tr}[Y(t_2)X(t_1)Y] = 0$, with corrections that vanish in the limit $|t_3 - t_1|/t_R \gg 1$. In this regime $k_\ell(\ell/v_B{-}|t_1|) = 0$, so again Eq. (4.7) is satisfied.

Corrections to Eq. (4.7) are expected to be parametrically small except near the butterfly front: the regime excluded from (i) - (iii), in which $|t_2| \lesssim t_R$, $|t_3 - t_1| \lesssim t_R$ and $|\ell/v_B{-}|t_1|| \lesssim \Delta\tau$. This has a width in t_1 that is much narrower at large ℓ than the main scale ℓ/v_B.

Clearly $G(\omega_1, \omega_2, \omega_3)$ and $g(t_1, t_2, t_3)$ and are related by Fourier transform, obtained by summing over the times t_1, t_2, t_3. The corrections to (4.7) affect only a vanishing fraction of contributions for $\ell \gg v_B t_R$. From this, we deduce

$$G(\omega_1, \omega_2, \omega_3) \overset{\lim}{=}_{\ell \to \infty} F(\omega_2) F(\omega_3) K_\ell(\omega_1 + \omega_3)\,, \tag{4.8}$$

where we have introduced the Fourier transform

$$K_\ell(\omega) = \frac{1}{2\pi} \sum_t k_\ell(\ell/v_B - |t|) e^{-i\omega t}\,. \tag{4.9}$$

Our discussion of the form of $k_\ell(t)$ implies that $K_\ell(\omega)$ is maximum at $\omega = 0$ and has a width in frequency of order v_B/ℓ. At large ℓ, since $\Delta\tau \ll \ell/v_B$, we can represent $k_\ell(\tau)$ as a step function and obtain the scaling form

$$\lim_{\ell \to \infty} \frac{1}{\ell} K_\ell(u/\ell) = \frac{\sin(u/v_B)}{2\pi u} \tag{4.10}$$

dependent only on the butterfly velocity of the model.

Eqns. (4.8) and (4.10) constitute our main theoretical results. They apply to a pair of operators acting at points separated by $\ell \gg v_B t_R$. In this limit they show that non-Gaussian correlations of matrix elements, which are not modelled by the ETH, have universal structure in frequency. This structure appears on a much finer scale (v_b/ℓ) than the one $(1/t_R)$ relevant for the Gaussian correlations that are represented by the ETH.

4.4 Numerical results

To test these ideas in a computational study, we consider the one-dimensional L-site FRUC in Eq. 1.35, which consists of Haar-distributed random unitaries and acts

on q-state quantum 'spin' at each site. This model has no conserved quantities or discrete symmetries. As shown in Ch. 2, many dynamical quantities can be computed analytically for $q \to \infty$: in this limit the autocorrelation function decays to zero in a single Floquet period ($t_R \to 0$) and the OTOC exhibits a light-cone with $v_B = 2$ and no broadening of the front. At finite q, the Floquet random circuit provides an ideal setting to investigate the general phenomenology of Eqns. (4.8) and (4.10).

We focus on $q = 2$ where the space of single-site operators is spanned by Pauli operators $\hat{\sigma}^j_\alpha$, with $\alpha = x, y, z$ and $j = 1, \ldots, L$. We consider system sizes $L = 4, 6, \ldots, 12$ and perform the full diagonalization of the unitary matrix $\hat{W}$. We first study the statistics of the matrix elements $X_{\alpha\beta}$ and the function $F(\omega)$ for the operator $\hat{X} = \hat{\sigma}^1_z$, using a closed chain in order to minimise boundary effects. The short-time behavior of the autocorrelation function can be computed analytically [**?**] giving $\langle X(t)X\rangle = 1$, 0, 6.67×10^{-3} and 3.87×10^{-3}, for $t = 0$, 1, 2 and 3. Hence in this model t_R is short and $F(\omega)$ is almost constant. For this reason, we neglect the dependence of $h(\omega)$ on ω and compute the combined probability distributions of all off-diagonal matrix elements, and of all diagonal elements. As shown in Fig. 4.1, 4.2 and 4.3, ETH gives an outstandingly accurate description for both quantities. (For similar results in a Hamiltonian system, see e.g. Ref. [**?**, **?**])

Next we turn to the four-point correlators and test the predictions of Eqns. (4.8) and (4.10). To maximise the separation $\ell = L - 1$ at a given L, we choose two operators acting on sites at opposite ends of an open chain:

$$\hat{X} = \hat{\sigma}^1_z \,, \quad \hat{Y} = \hat{\sigma}^L_z \,. \tag{4.11}$$

An overview of the data for $G(\omega_1, \omega_2, \omega_3)$ is given in Fig 4.4. For the largest accessible system size, $L = 12$, in each realization we sample 10^8 contributions to each ω bin. Additionally, we average $G(\omega_1, \omega_2, \omega_3)$ over around 700 realizations. The data show

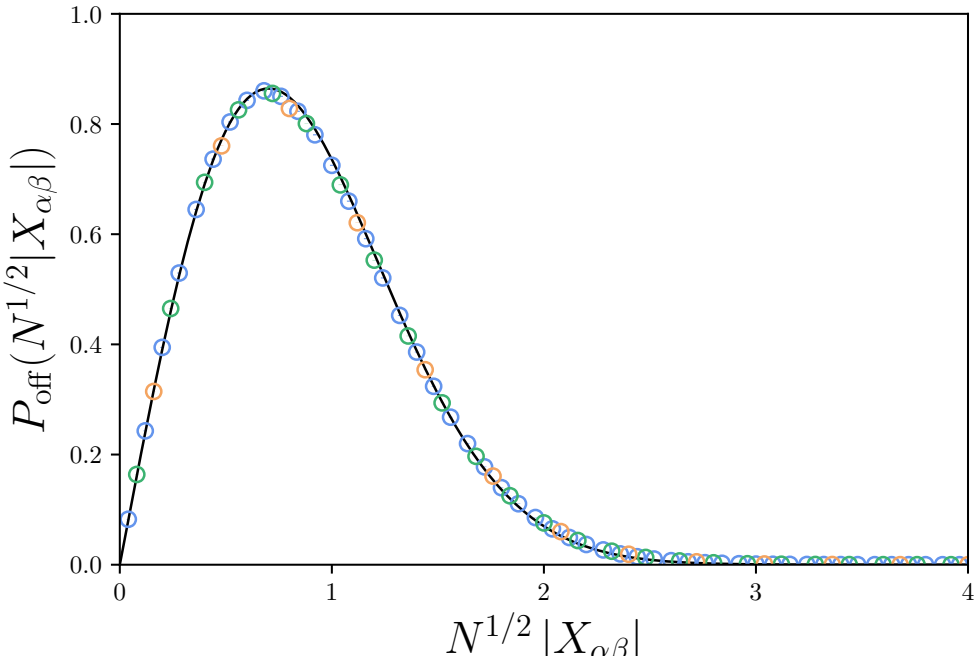


Figure 4.1: Scale-collapsed probability distribution $P_{\rm off}(N^{1/2}|X_{\alpha\beta}|)$ of the modulus of off-diagonal elements $X_{\alpha,\beta}$ of a local operator for the FRUC with $N = 2^L$. Points: data for $L = 6, 8, 10$ in blue, green, yellow respectively. Line: complex Gaussian distribution, as expected from the ETH.

the expected narrow maximum near the plane $\omega_1 + \omega_3 = 0$. For a quantitative analysis, we project $G(\omega_1, \omega_2, \omega_3)$ onto two orthogonal lines. First, we have as an identity (taking $\omega_1 + \omega_3 - \omega \bmod 2\pi$)

$$K_\ell(\omega) = \int_{[-\pi,\pi]^3} \mathrm{d}\omega_1 \mathrm{d}\omega_2 \mathrm{d}\omega_3 \, \delta(\omega_1 + \omega_3 - \omega) G(\omega_1, \omega_2, \omega_3) \, .$$

Second, we define

$$J(\omega_2) = \int_{[-\pi,\pi]^2} \mathrm{d}\omega_1 \mathrm{d}\omega_3 \, G(\omega_1, \omega_2, \omega_3) \, . \tag{4.12}$$

From Eq. (4.8) we expect $J(\omega) \approx F(\omega)$.

Results for both functions are presented in Fig 4.5, and match excellently the expectations we have described. The data in the main panel show a perfect collapse of the central peak for all accessible system sizes, in agreement with the scaling form

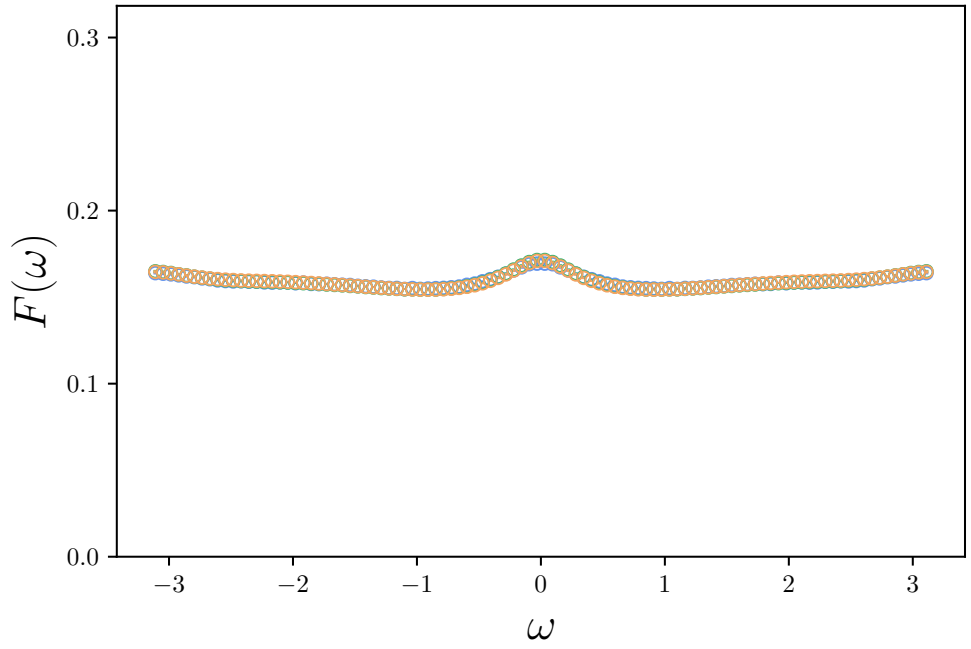


Figure 4.2: $F(\omega)$ vs ω for the FRUC with $L = 6, 8, 10$ in blue, green, yellow respectively.

of Eq. (4.10). The left inset shows a fit of the central peak in $K_\ell(\omega)$ to the Fourier transform of the step function $\Theta(|\ell/v_B - t|)$. Since t takes only integer values, the fit yields a range of possible values for the butterfly velocity: from $L = 10$, we obtain $v_B \in [1.125, 1.286]$. This range includes the value for a random quantum circuit, $v_B = 2(q^2 - 1)/(q^2 + 1)$ or $v_B = 1.2$ at $q = 2$ [**?**, **?**]. The deviations of the data from the fitting function away from the central peak are due to the diffusive broadening of the step in the OTOC (for these system sizes $\Delta\tau \sim 1$).

The right inset of Fig 4.5 shows $J(\omega)$ vs ω. In this case data for all system sizes collapse *without* rescaling ω with ℓ, as anticipated from Eq. (4.8) but in contrast to behaviour for $K_\ell(\omega)$. We expect in addition from Eq. (4.8) that $J(\omega) = F(\omega)$. In fact, the peak in $J(\omega)$ near $\omega = 0$ is much more pronounced than is shown for $F(\omega)$ in Fig. 4.1. The discrepancy arises from different choices of boundary conditions: periodic for Fig. 4.1, open for Fig. 4.5. Viewed in the time domain, decay of $f(t)$

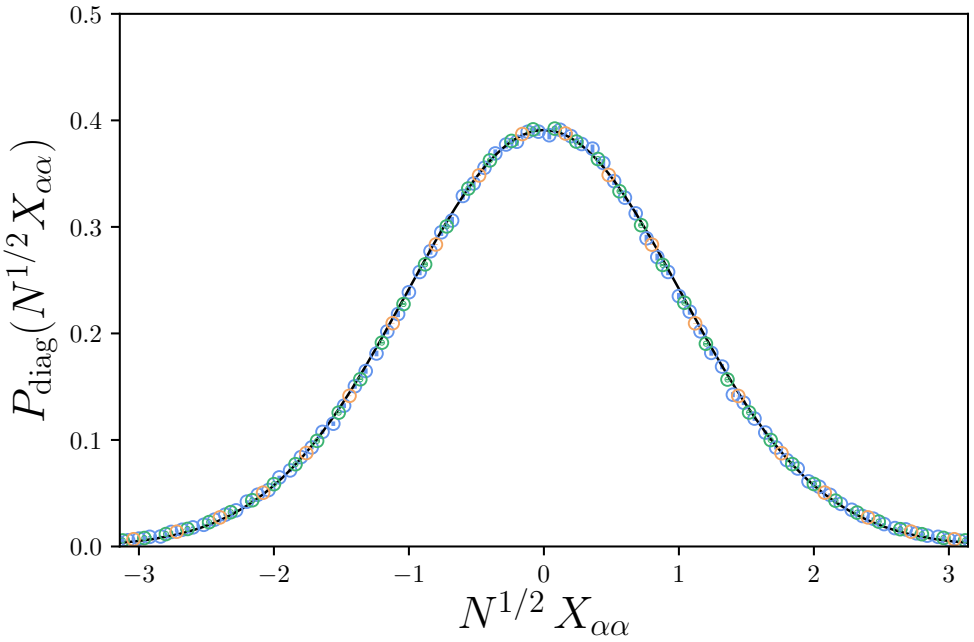


Figure 4.3: Scale-collapsed probability distribution of the diagonal elements $P_{\mathrm{diag}}(N^{1/2}X_{\alpha\alpha})$ for the FRUC. Points: data for system sizes $L = 6, 8, 10$ in blue, green, yellow respectively. Line: real Gaussian distribution, as expected from ETH.

is slower for an operator at the end of an open chain than with periodic boundary conditions, because its spreading is hindered. Fig. 4.6 shows that $F(\omega)$ for an operator at the end of an *open* chain has a very similar form to $J(\omega)$.

Finally, and crucially, we show support for our main result in Fig 4.7. The product form given in Eq. (4.8) indeed provides a very accurate representation of $G(\omega_1, \omega_2, \omega_3)$.

4.5 Discussion and outlook

It is natural to ask about the behaviour of other correlators. Within the Floquet model we have described, non-zero correlators must have even numbers of operators acting at each site, since odd powers vanish under the ensemble average. The only two-point correlator is hence $\mathrm{tr}[\hat{X}(t)\hat{X}]$. Besides the generalised OTOC, there is a second four-point correlator, with the form $\mathrm{tr}[\hat{X}(t_3)\hat{X}(t_2)\hat{Y}(t_1)\hat{Y}]$. This correlator

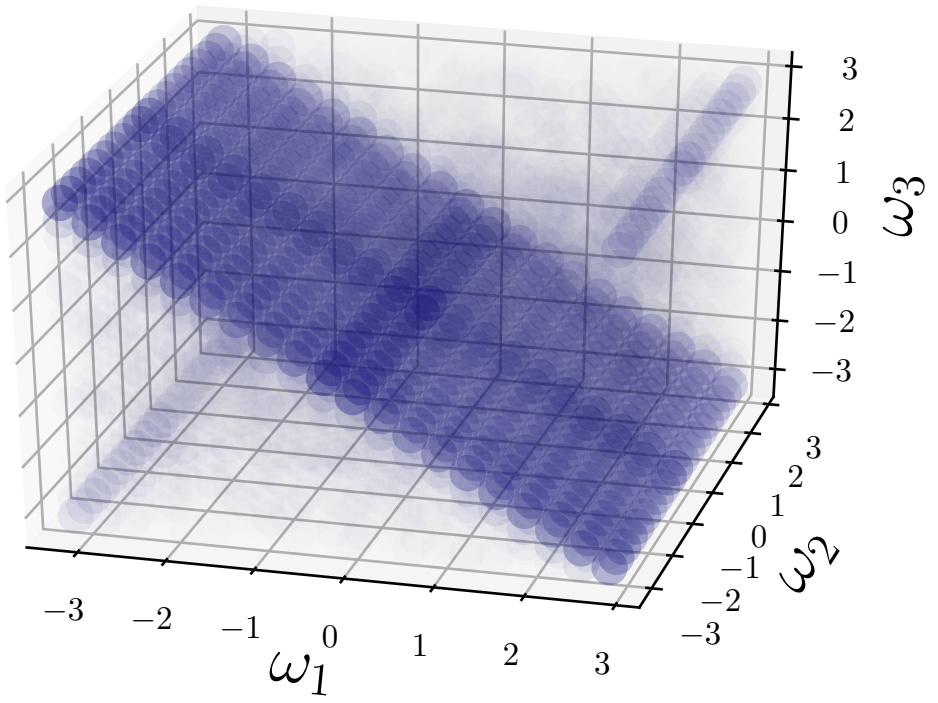


Figure 4.4: Histogram of $G(\omega_1, \omega_2, \omega_3)$ as a function of ω_1, ω_2 and ω_3, for $L = 12$ with 20 bins along each axis. Larger values of $|G(\omega_1, \omega_2, \omega_3)|$ are shown with heavier shading.

has no long-time structure and therefore no small-frequency features. It is captured for large ℓ by the ETH, since it factorises in this limit as $\mathrm{tr}[\hat{X}(t_3)\hat{X}(t_2)]\mathrm{tr}[\hat{Y}(t_1)\hat{Y}]$. Hence $G(\omega_1, \omega_2, \omega_3)$ is unique in its sharp ω-space structure.

We expect the phenomenology we have described to be very generic, as it arises from fundamental features of chaotic dynamics in spatially extended systems. In particular, our conclusions will also hold in higher spatial dimensions. In addition, although we have treated the simplified context of Floquet systems, we expect our conclusions to apply with some caveats in the presence of conserved quantities. To be specific, consider a system with a time-independent Hamiltonian $\hat{H}$ and energy as the only conserved density, and examine matrix elements of operators between eigenstates of $\hat{H}$. In this case, the appropriate thermal average at inverse temperature β is $\langle\cdot\rangle_\beta \equiv \mathcal{N}^{-1}\,\mathrm{Tr}[\,\cdot\, e^{-\beta\hat{H}}]$. A consequence, as for the standard ETH, is that all spectral correlators, including the functions F, G and K_ℓ, as well as v_B, acquire a smooth

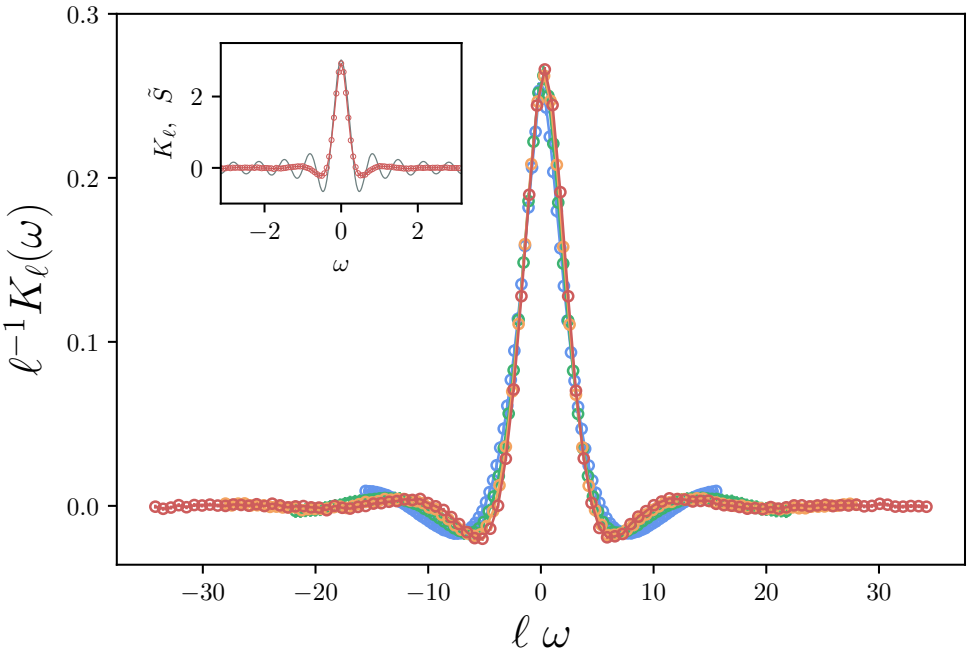


Figure 4.5: Main panel: $\ell^{-1}K_\ell(\omega)$ vs $\ell\omega$ for $L = 6, 8, 10, 12$ in blue, green yellow and red respectively. Left inset: $K_\ell(\omega)$ vs ω (red) compared with Fourier transform $\tilde{S}$ of the step function $\Theta(|\ell/v_b - t|)$ (grey) for $L = 12$.

temperature dependence. Following [**?**, **?**], we expect that for operators $\hat{X}$ and $\hat{Y}$ that do not couple to the conserved charge, our conclusions will hold unchanged. On the other hand, if $\hat{X}$ or $\hat{Y}$ couple to the energy density, both the on-site relaxation in (4.3) and the OTOC in (4.5) will present power-law tails. This slow dynamics may affect [**?**] the separation of scales $\ell \gg v_B t_R$ that we exploited in deriving Eq. (4.7) and we leave further analysis for future studies.

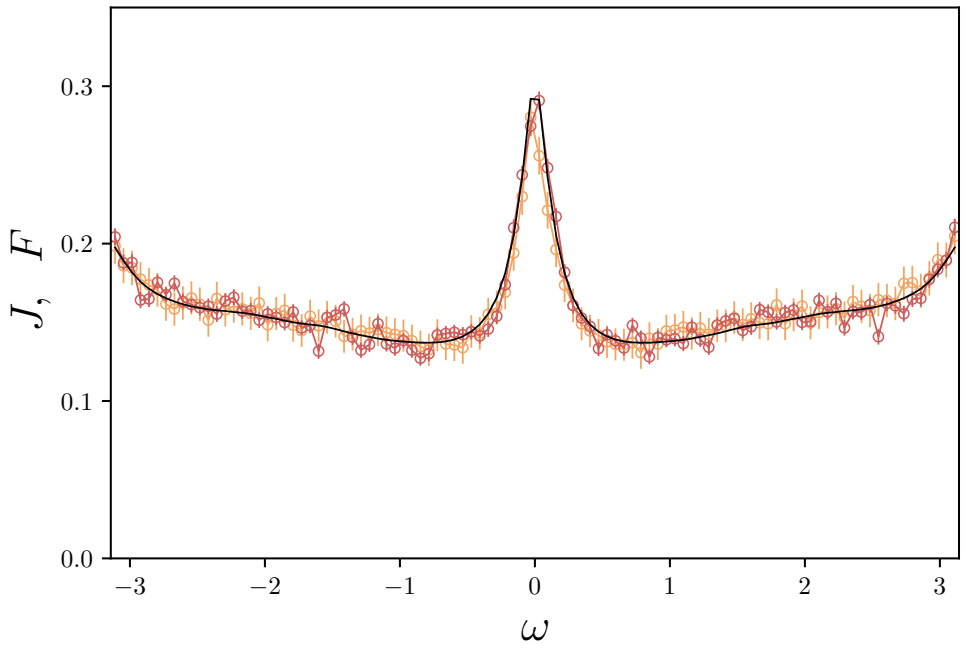


Figure 4.6: $J(\omega)$ vs ω for $L = 10, 12$ (yellow and red) compared with $F(\omega)$ vs ω for $\hat{X}$ acting on a site at the end of an open $L = 12$ chain (black).

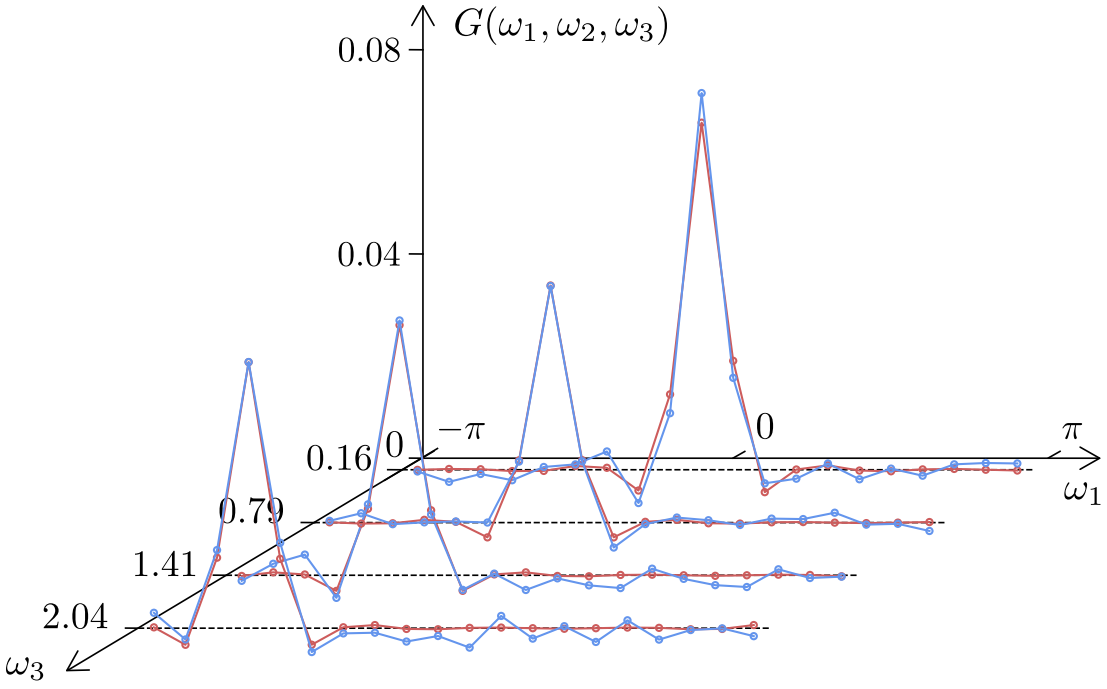


Figure 4.7: To test Eq. 4.8, we plot with offsets $G(\omega_1, \omega_2, \omega_3)$ (blue) and $F(\omega_2)F(\omega_3)K_\ell(\omega_1 + \omega_3)$ (red) vs ω_1 for $L = 12$ at $\omega_2 = -1.73$. Plots for other values of ω_2 and ω_3 show similar agreement.

Chapter 5

Summary and outlook

In this thesis, we have studied the signatures of chaotic quantum dynamics in spatially-extended systems beyond the RMT description by analysing two Floquet random unitary circuits as minimal models. These Floquet circuits are random in space but periodic in time, and consist of local quantum gates that act on a q-state 'spin' at each site. In Ch. 2, we formulate a diagrammatical approach for computing ensemble averages of observables over random unitary circuits, and derive exact results for the FRUC (1.35) in the large-q limit. We show that quantum dynamics in this system exhibits a range of features that are expected to be characteristic of ergodic many-body quantum systems: correlators of local observables decay rapidly in time and quantum information spreads ballistically, in the sense that the bipartite entanglement of an initial product state grows linearly in time, and the OTOC shows the butterfly effect. The diagrammatic formulation leads to several natural future directions. One can attempt to obtain the higher order corrections in the $1/q$ expansion, and also to look at fluctuations of the observables like the quantum purity. Furthermore, the diagrammatical technique can be used to analyse FRUC in higher dimensions and FRUC from the different symmetry classes of the RMT. In the context of quantum transport, it would be interesting to incorporate the presence of

conserved quantities, by modifying the local structure of the Floquet operator, as has been done recently for random quantum circuits [**?**, **?**]. Lastly and most ambitiously, one can attempt to construct an analogous diagrammatic formulation to analyse the corresponding random Hamiltonian problem.

In Ch. 3, we study spectral statistics in spatially extended chaotic quantum many-body systems, using the FRPC (1.36). Computing the spectral form factor $K(t)$ analytically and numerically, we show that it follows the RMT form at times longer than a many-body Thouless time, t_{Th}. We obtain a dependence of t_{Th} on the spatial dimension d and size of the system. For $d > 1$, t_{Th} is finite in the thermodynamic limit and set by the inter-site coupling strength. By contrast, in one dimension t_{Th} diverges with system size, and for large systems there is a wide window in which spectral correlations are not of RMT form. Furthermore, our Floquet model FRPC exhibits a many-body localization transition and we discuss the behavior of the spectral form factor in the localized phase. An important extension of this work is to provide an analytical computation of $K(t)$ in Floquet random unitary circuits with conserved quantities, which has been argued and numerically shown to be characterized by $t_{\mathrm{Th}} \sim L^2$ [**?**]. Another exciting direction is to investigate the MBL-ergodic transition exhibited in random circuits like the FRPC, especially from the the ergodic phase of the transition.

In Ch. 4, we discuss eigenstate correlations for ergodic, spatially extended many-body quantum systems, in terms of the statistical properties of matrix elements of local observables. While the ETH is known to give an excellent description of these quantities, the phenomenon of scrambling and the butterfly effect imply structure beyond ETH. We determine the universal form of this structure at long distances and small eigenvalue separations for Floquet systems. We use numerical studies of a Floquet quantum circuit to illustrate both the accuracy of ETH and the existence of our predicted additional correlations. A future direction is to extend the

analysis to higher point correlators of operators at two or multiple spatial locations, which may shed light on the joint probability distribution of the matrix elements of these operators. Furthermore, the addition of conserved quantities will change the behaviour of on-site relaxation in (4.3) and the OTOC in (4.5). This slow dynamics [**?**] may affect the separation of scales $\ell \gg v_B t_R$ that we exploited in deriving Eq. (4.7), and we leave this open problem for future investigation.

Appendix A

Appendices of Chapter 2

A.1 Recursive formula for $V_{c_1,c_2,\ldots,c_u}$

The coefficient $V_{c_1,\ldots,c_k}$ appearing in Eq. (2.6) obeys the recursion relation [**?**, **?**, **?**]

$$\begin{aligned}\delta_{c_1,1} V_{c_2,\ldots,c_k} = N V_{c_1,\ldots,c_k} + \sum_{p+q=c_1} V_{p,q,c_2,\ldots,c_k} \\ + \sum_{j=2}^{k} c_j V_{c_1+c_j,c_2,\ldots,c_{j-1},c_{j+1},\ldots,c_k} \,.\end{aligned} \tag{A.1}$$

where $V_\varnothing \equiv 1$ and $N = q^2$ is the dimension of the unitary group from which the Haar-distributed unitary operators are drawn.

A.2 Enumeration of leading order diagrams

In the following, we describe two methods for efficiently enumerating the leading order diagrams for the physical quantities we have computed. The contraction addition method described in App. A.2.1 can be used to eliminate sub-leading single-site diagrams efficiently, which is particularly useful if the many-body diagram of interest has the same site-diagrams across all sites (e.g. the spectral form factor). The domain

wall (DW) approach described in App. A.2.2 allows us to obtain an upper bound to the order, a global property of a diagram, by making only local calculations between neighbouring domains. We apply the ideas from App. A.2.1 in App. A.3, A.4 and A.7, and those from App. A.2.2 in App. A.5 and A.7.

The foundation for both these methods is Eq. (2.9), which gives the order $\mathcal{O}(G)$ of a diagram G as a product of factors $q^{\tau_i+u_i-n_i}$ from each site. As the numbers τ_i of T-loops and u_i of U-loops contribute to the order in the same way, we do not need to distinguish between T- and U-loops in the calculation of order discussed below.

A.2.1 Method of contraction-addition

An ensemble-averaged many-body diagram consists of L site diagrams labelled by i, each with a number n_i of contractions. The idea of this approach is that, given a site diagram, we can first remove all the contractions, and then re-construct the diagram by adding contractions one at a time. The order can be evaluated by considering the effect of each contraction-addition. The crucial point is that the procedure is independent of the sequence of contraction-additions. Each addition either leaves the order in q unchanged (if it increases both $\tau_i + u_i$ and n_i by one), or reduces the order (if the addition increases only n_i, or reduces $\tau_i + u_i$ and increases n_i). A convenient sequence (one that contains order-reducing contraction-additions in the first few steps) can therefore be used to eliminate sub-leading diagrams efficiently.

To be more precise, given a diagram G, we consider the single-site configuration G_i on site i. We choose a sequence of diagrams $\{G_i^{(0)}, \ldots, G_i^{(n_i)}\}$, such that $G_i^{(0)}$ has no contractions, $G_i^{(m+1)}$ is obtained from $G_i^{(m)}$ by adding one contraction, and $G_i^{(n_i)} = G_i$. The overall order is then

$$\mathcal{O}(G) = \prod_{i \in \text{site}} \mathcal{O}(G_i^{(0)}) \prod_{m=1}^{n_i} \Delta_i^{(m)} \,. \tag{A.2}$$

Here, $\Delta_i^{(m)} = \mathcal{O}(G_i^{(m)})/\mathcal{O}(G_i^{(m-1)})$ is the change in the order when one contraction is added.

As we have established that we do not need to distinguish between T- and U-loops here, each contracted site diagram can be represented as a collection of loops, using the same notation for both types of loop. The same representation can also be used for each intermediate $G_i^{(m)}$ despite the fact that the notion of distinct T- and U-loops may not apply to $G_i^{(m)}$. The addition of a contraction has the effect either of merging two loops into a single longer one, or of breaking one loop into two. To see this, recall the prescription for construction of loops in a single-site configuration G_i that is implied by Fig. 2.5. It can be expressed as follows. Start at any point on a single (for T-loops) or double (for U-loops) line; follow the direction along this line; when a dashed line is encountered, go to the other end of the dashed line and continue along the single or double line in the same sense; repeat until the starting point is reached: the path traced is a loop. Addition of an extra contraction to this prescription simply re-routes the paths of the two loop segments that meet the contraction from either side. Moreover, since the two ends of the dashed line depicting a contraction are attached either to two separate loops or to two different portions of the same loop, we can evaluate $\Delta_i^{(m)}$ omitting all information except what concerns the one or two loops involved in the contraction. Once one focuses on the relevant details in this way, there are only eight distinct contraction-addition scenarios. We list them all in Fig. A.1, using a single unbroken line to denote generic loops. A minor complication is that it is necessary to distinguish loops that pass through one or two operators representing local observables from ones that do not, since these operators may also affect the weight of a diagram.

We provide a simple example of how this approach to determining the order of a site diagram works in Fig. A.2.

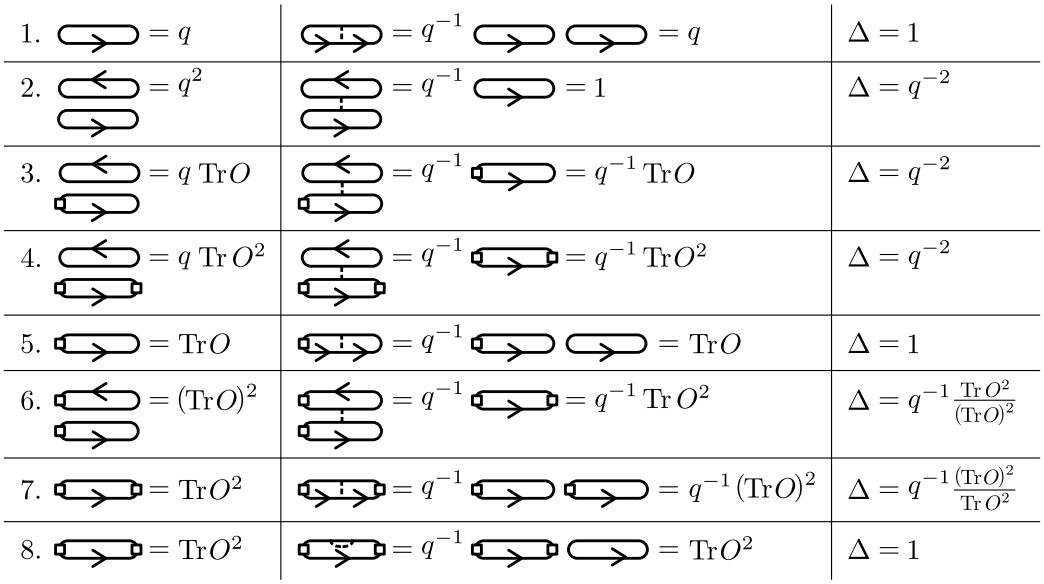


Figure A.1: Enumeration of all distinct ways in which a contraction may be added to a site diagram. Columns, from left to right, are as follows. (i) Eight distinct combinations of one or two loops, before addition of a contraction, with associated contributions to $\mathcal{O}(G_i^{(m-1)})$. Three types of loop appear, containing zero, one or two local operators O indicated using open squares. (ii) The same after adding a contraction, shown as a dashed line, and re-drawn purely as loops, with associated contributions to $\mathcal{O}(G_i^{(m)})$. (iii) Values of $\Delta^{(m)}$ arising from each contraction, obtained as the ratio of contributions in columns (ii) and (i).

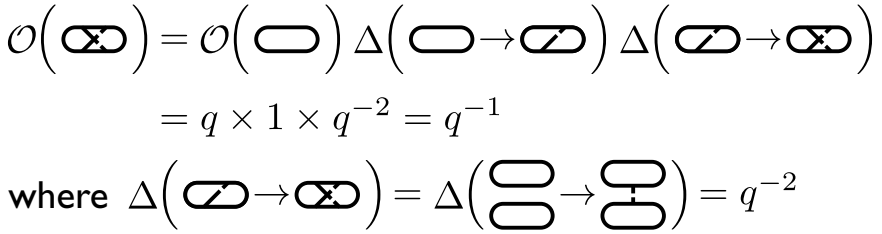


Figure A.2: An example of order determination of a diagram using the method of contraction-addition. Arrows giving an orientation to loops are omitted for clarity.

A.2.2 Domain wall approach

In Sec. 2.4.3 we set out a way of considering contributions to some quantities of interest, in terms of space-time domains within which contractions are all of the same type. The power of this approach lies in the fact that one can associate a bound on the diagram's order with each DW between two neighbouring domains. This allows us to calculate a bound on the diagram's order, a global property, by making

only local calculations between neighbouring domains. We explain details here, using for concreteness the 2nd Rényi entropy (see Sec. 2.4.3) and referring to the block representation introduced in App. A.5.1 and Fig. A.3.

First, we rewrite the order of a diagram G in terms of loops. We define the length c_k of a loop k as half of the number of non-dashed lines it contains. We make the convention that single lines at the top edge (where W and $W^\dagger$ are multiplied) are counted twice, so that lengths are always integer numbers (e.g. at the top edge of Fig. 2.4 there are four single lines in each single-site diagram). This generalises the definition given in Ch. 2.3 to both U-loops and T-loops. We also define the total length $l_t = \sum_k c_k$ where the sum runs over all loops. Then the order of a diagram in (2.9) can be re-written

$$\mathcal{O}(G) = q^{l_t - n} \prod_{k \in \text{loops}} \Gamma_{c_k} \,, \tag{A.3}$$

where $\Gamma_c = q^{1-c}$ and $n = \sum_i n_i$ is the total number of contractions. The values of l_t and n are fixed by the observable of interest. In particular, for the 2nd Rényi entropy $l_t = n$.

The intuition behind Eq. (A.3) is as follows. Since a given diagram has a fixed number of length segments, its order is high (low) when there are many short (a few long) loops. The pre-factor $q^{l_t - n}$ represents the theoretical maximum order when all length segments are used to form 1-loops. Γ_c is the cost associated with a loop of length c, and its value decreases as c increases. For example, Γ_1 has value 1 since 1-loop is the shortest possible loop. Γ_2 has value q^{-1} because one could have formed two 1-loops (giving a factor of q^2 in Eq. (2.9)) instead of one 2-loop (giving a factor of q).

Next, we rewrite the order of a diagram in terms of boundaries that intersect the loops. We define a *boundary* as a *horizontal* segment of unit lattice spacing that separates two blocks (for example, the red lines in Fig. A.5 top), so that each block has four boundaries (except for the blocks representing the trace structure at the upper

edge, e.g. zero-th row in Fig. A.5 top). Every loop instersects two such boundaries per unit length. To each boundary w, we can therefore associate a cost

$$\mathcal{C}(w) = \prod_{\substack{k \in \text{loops} \\ k \nmid w}} \Gamma_{c_k}^{1/2c_k} \tag{A.4}$$

where k labels the loops that the boundary w intersects, and c_k is the corresponding loop length. In this way, the order of a diagram G is expressed in terms of the cost of each boundary, so that

$$\mathcal{O}(G) = q^{l_t - n} \prod_{w \in \text{walls}} \mathcal{C}(w) \ . \tag{A.5}$$

Since $\Gamma_1 = 1$, loops of unit length do not contribute to $\mathcal{O}(G)$. We obtain an upper limit on the cost of a boundary by assuming longer loops to have length not more than $c_k = 2$. This leads to

$$\mathcal{C}(w) = \prod_{k \nmid w, c_k \geq 2} \Gamma_{c_k}^{1/2c_k} \leq q^{-n_w/4} \tag{A.6}$$

where n_w is the number of loops crossing the boundary w with length longer than 1. Referring to examples in Fig. A.5, $\mathcal{C}(w)$ for the top sub-figure is bounded by (and equal to) q^{-1} with $n_w = 4$, and $\mathcal{C}(w)$ for the bottom sub-figure is bounded by $q^{-3/4}$ with $n_w = 3$. As we will see, a costly boundary (one with $n_w > 0$) is always sandwiched between blocks with different contractions. It is therefore natural to call such a boundary a *domain wall* (DW). With minor modifications, this method can also be applied to diagrams that contain local operators.

A.3 Spectral form factor

Here we use the method of contraction-addition (App. A.2.1) to enumerate the leading order diagrams for $\langle K(t)\rangle$. In Eq. (A.2) we have $n_i = 4t$ and $\mathcal{O}(G_i^{(0)}) = q^2$. There are only two relevant contraction-addition scenarios illustrated in Fig. A.1: (i) An intra-loop addition (item 1 in figure), where the two legs of the new contraction line land on the same loop. Then $\Delta = q^0$ according to Eq. (2.9) because $\tau + u$ and n both increase by one. (ii) An inter-loop addition (item 2 in figure), where the two contraction legs land on two different bare loops. Since the two loops merge into a single bigger loop due to the new contraction, $\tau + u$ decreases by one, and n increases by one. So $\Delta = q^{-2}$.

The many-body diagram for $K(t)$ comprises site diagrams before contraction as in Fig. 2.6a. For $t = 0$ we have $K(t) = q^{2L}$ since $W(0) = \mathbb{1}_{q^L}$. To compute the large–q limit of $K(t)$ for $t > 0$, we first note that there are diagrams with multiple contractions that are $O(1)$, such as Fig. 2.7c. This is in fact a highest order diagram for $t > 0$ according to Eq. (A.2), because there must be at least one inter-loop contraction-addition which is associated with $\Delta = q^{-2}$ per site, and because, from Fig. A.1, the later contraction-additions can be made without increasing the order of the diagram. So any diagrams with order smaller than $O(1)$ are sub-leading.

There are t leading order site diagrams on site i, by the following argument. Using the fact that the order determination is independent of the sequence of contraction-addition, we choose to contract on site i the (filled and un-filled) blue dots on the top layer from left to right. The first filled blue dot can be contracted with any one of the t filled blue dots on the bottom layer. This inter-loop contraction costs q^{-2}. In order to obtain a leading diagram, the later contractions must all be of $O(1)$, i.e. intra-loop contractions. A general feature of an $O(1)$ contraction is that it must partition a bigger loop into two smaller loops, such that the q factor associated with the extra loop (since τ or u increases by one) cancels the q^{-1} factor of the contraction (since

n increases by one) (see Fig. A.1). Furthermore, on each of the two smaller loops, there must be equal numbers of un-contracted blue dots on the top and bottom layer. Otherwise, there will be an inter-loop contraction which will render the diagram sub-leading. It is straightforward to see that there is a unique choice of contraction of the second blue dot that satisfies this requirement. Similarly, there are unique choices for the rest of the blue dots on this site. In order to not incur further cost on site i, each red dot on the top layer must be contracted with the only other red dot on the same loop on the bottom layer. So there are unique choices for the red dots as well.

Due to the bond constraint, the $(i+1)$-th site diagrams inherit the choice of either the blue or red dot contractions on site i. We can repeat the above analysis site-by-site and conclude that there are t leading order diagrams of $O(1)$ for $t > 0$ (Fig. 2.6b,c and d).

Lastly, each of these t diagrams is translated algebraically to the factor 1, simply observing that it is Gaussian and for each site $\tau_i + u_i = n_i$ in (2.9). In other words, for $t > 0$, $K(t) = t$, and we have arrived at Eq. (1.19).

A.4 Relaxation of local observables

Here we prove Eq. (2.1). For $t = 0$, the calculation is straightforward since $W(0) = \mathbb{1}_{q^L}$. For $t = 1$, there is only one configuration at each site because there is only one pair of dots of each kind. Since we have chosen $\operatorname{Tr} O_x = 0$, the algebraic term associated with this diagram vanishes. For $t > 1$, we use the same argument as in App. A.3 to show that every possible diagram has an order that vanishes as $q \to \infty$. In the formulation of contraction-addition (App. A.2.1), we have $n_i = 4t$ and $\mathcal{O}(G_i^{(0)}) = 1$. On site x, we choose to first contract the blue dot on the bottom left of the diagram (Fig. 2.7b). This bottom left blue dot cannot be contracted with the bottom right blue dot non-trivially since $\operatorname{Tr} O_x$ is zero. However, if this bottom

left blue dot is contracted with any other blue dots, it will partition a bigger loop into two smaller loops, each of which has an unequal number of dots from Us and $U^\dagger$s. This implies that there will be at least one addition of an inter-loop contraction with $\Delta \propto q^{-1}$ (item 6 in Fig. A.1). Since all other contraction-additions can only further reduce the order according to Fig. A.1, we have $\mathcal{O}(G) < q^{-1}$ for any diagram G associated with $\langle [O(x,t)O(x)]_{\text{av}} \rangle$ when $t > 1$.

A.5 2nd Rényi entropy

The diagramatic representation used in Fig. 2.8c requires a straightforward extension when it is empolyed in the presentation of detailed proofs, and we start by describing this extension. It arises for the following reason. The rectangles of Fig. 2.8c represent local contractions for a stack of two U's and two $U^\dagger$'s. Each contraction involves linking both open dots with open dots, and closed dots with closed dots. To allow for the possibility that different pairings are made for open dots and for closed dots, each rectangle appearing in Fig. 2.8c is divided horizontally into two in this Appendix.

A.5.1 Block representation of quantum purity

In detail, we introduce the *block representation* as follows. Beginning from the folded representation introduced in Sec. 2.4.3, we consider a stack of four unitary operators (blue box in Fig. 2.8). We use Fig. 2.2 to represent each unitary operator in terms of dots and double lines. A *block* is defined as a region within this box that encloses only filled (or only empty) dots. In this way, to each stack of four unitaries, we associate two blocks containing respectively filled and empty dots (so that, the four-legged symbol in the bottom right of Fig. 2.8b corresponds to two blocks in Fig. A.3 bottom). For $\langle \exp[-S_\alpha(t)] \rangle$, there are $4t$ rows of such blocks, and drawing each of them as an empty rectangle leads to the representation in Fig. A.3.

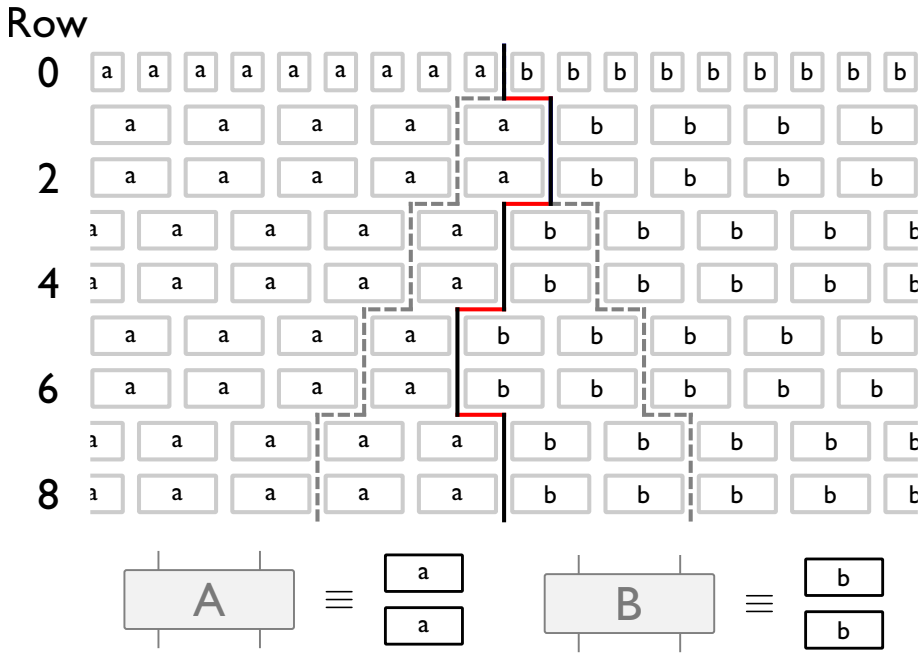


Figure A.3: Top: The block representation of a leading DW diagram for $\langle \exp[-S_2(t)] \rangle$. The top row (the zero-th row) denotes the effective blocks that represent the structure of traces in sub-regions A and B (Fig. 2.8b bottom left). The dashed line represents a light cone outside of which all unitary pairs can be annihilated as described in Fig. 2.1. The red line represents costly boundaries (between blocks of different contraction types, see Appendix A.2.2 and Table A.1). Bottom: The correspondence between blocks and the symbols used in the bottom right of Fig. 2.8b.

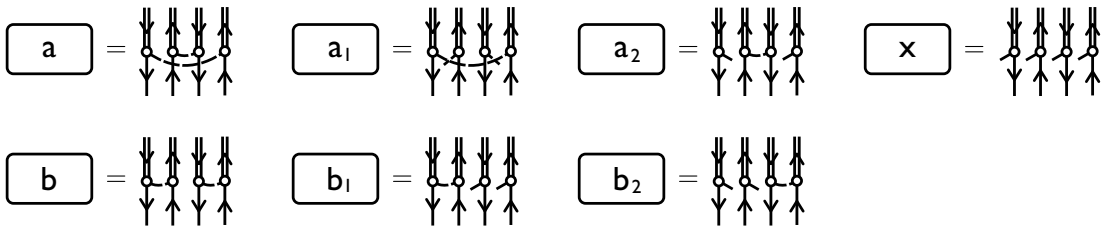


Figure A.4: Contractions in a portion of a site diagram for $\langle \exp[-S_2(t)] \rangle$, showing all seven possible block types.

We categorize the possible contractions of the dots within a block into seven types $\mathcal{T} = \{a, b, a_1, a_2, b_1, b_2, x\}$. As explained in the main text, a and b only involve local contractions (within the block), while x involves only non-local contractions. The other types are of mixed local and non-local character, and are defined in Fig. A.4. An upper bound $\omega(c, c')$ for the cost of the boundary between two neighbouring block

configurations $c, c' \in \mathcal{T}$ is shown in Table A.1. Two examples of the evaluation of $\omega(c, c')$ are illustrated in Fig. A.5 using the method introduced in Appendix A.2.2.

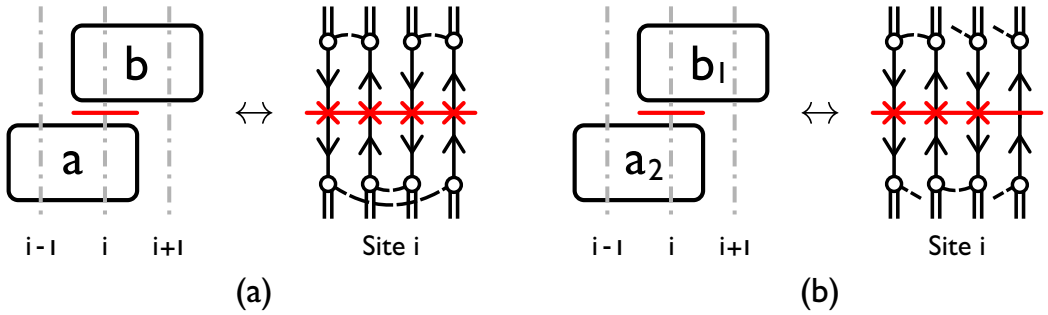


Figure A.5: Examples of contractions in a portion of a site diagram for $\langle \exp[-S_2(t)] \rangle$. Left sides of (a) and (b): two neighbouring blocks along site i, shown in the space-time plane with the time axis vertical. Right sides of (a) and (b): equivalent site diagrams with the time axis vertical; open-ended dashed lines are contracted non-locally with an external block. Red lines represent sections of boundary (of unit length in the left-hand pictures). (a) right: the boundary crosses four times a loop of length at least 2 at the red crosses, so $\omega(a, b) = q^{-1}$. (b) right: The boundary has three costly crossings, so $\omega(b_1, a_2) = q^{-3/4}$.

ω	a	b	a_1	a_2	b_1	b_2	x
a	q^0	q^{-1}	$q^{-1/2}$	$q^{-1/2}$	q^{-1}	q^{-1}	q^{-1}
b		q^0	q^{-1}	q^{-1}	$q^{-1/2}$	$q^{-1/2}$	q^{-1}
a_1			q^0	q^{-1}	$q^{-3/4}$	$q^{-3/4}$	$q^{-1/2}$
a_2				q^0	$q^{-3/4}$	$q^{-3/4}$	$q^{-1/2}$
b_1					q^0	q^{-1}	$q^{-1/2}$
b_2						q^0	$q^{-1/2}$
x							q^0

Table A.1: Upper bounds for the cost associated with the boundaries between the seven possible types of block contraction. The matrix is symmetric and so only the upper triangle is written explicitly.

A.5.2 Evaluation of quantum purity

We discuss diagrams for $\langle \exp[-S_2(t)] \rangle$ in terms of different block pairings. We first fix our convention as follows. We label the rows of blocks from the top as in Fig. A.3. We refer to the boundaries immediately above the p-th row of blocks as the p-th row of boundaries.

Due to the simplification illustrated in Fig. 2.1, pairs of U and $U^\dagger$ can be cancelled outside of the light cone originating from the sub-system boundary (shown with dashed lines in Fig. A.3). Alternatively, instead of cancelling them, it is equivalent to assume that the blocks on the far left and far right have respectively a- and b-contractions, as long as we remain in the large-q limit. Consistently, this choice implies costless boundaries according to Table A.1. Therefore, in particular, a configuration for any given odd row of boundaries can be parametrised as in Fig. A.6, and we denote this as $(ad_1d_2d_3\dots d_kb)_{\text{wall}}$ with variables $d_1 \neq a$, $d_k \neq b$, and $d_i \neq d_{i+1}$ for $i = 1, \dots, k-1$. a, b and d_i represent (connected) domains of blocks with the same type of contractions. Note that for every change of domain, there is a DW associated with a factor of q^{-m} with $m > 0$.

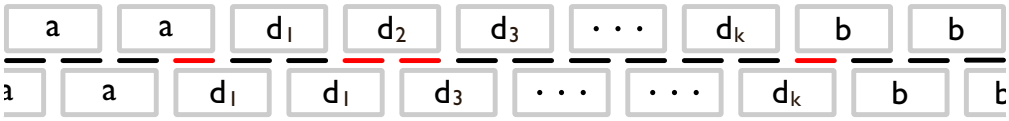


Figure A.6: A generic configuration of an odd row of boundaries denoted as $(ad_1d_2d_3\dots d_kb)_{\text{wall}}$. Costly boundaries (DWs) are drawn in red. Costless boundaries are drawn in black.

We claim the following for the leading diagrams. (i) Each odd row of walls has the form $(ab)_{\text{wall}}$. (ii) Each even row of walls is sandwiched between two rows of blocks with identical configurations. (iii) The leading diagrams have order q^{-2t}.

An example of order q^{-2t} can be found by constructing a single DW dividing two domains of blocks with contraction a and b (Fig. A.3), such that on the odd rows of boundaries, the order is $\omega(a, b) = q^{-1}$, and on the even rows of boundaries the order is 1. So any diagram with order lower than q^{-2t} is sub-leading.

To prove these statements, we note that an odd row $(ab)_{\text{wall}}$ has only one DW segment with cost q^{-1}. Conversely, by using the costs in Table A.1, it is easy to verify that any row configuration $(ad_1d_2d_3\dots d_kb)_{\text{wall}}$ with $k \geq 1$ always has an order

strictly smaller than q^{-1}. Note that the order of a row with $k \geq 2$ is straightforwardly smaller than q^{-1} since each wall costs at least $q^{-1/2}$.

An even row of walls that is sandwiched by two rows of blocks with different configurations is associated with an order of q lower than 1 because there is a costly wall sandwiched by two blocks of different types (see Appendix A.5.1).

Leading diagrams are obtained maximising the order on odd and even rows, thus proving (i) and (ii). Statement (iii) follows trivially from statements (i) and (ii). Finally, (ii) implies that these diagrams are Gaussian (see Ch. 2.4) and translate into positive algebraic factor. Hence, we have recovered Eq. 2.11.

A.6 3rd and higher Rényi Entropies

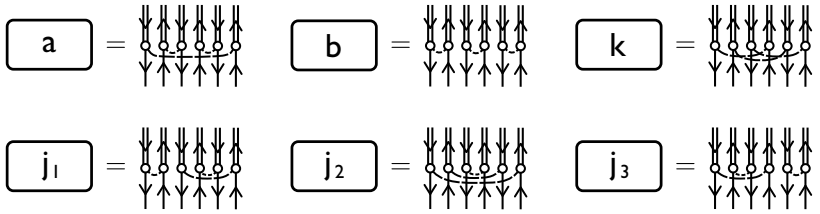


Figure A.7: The six local contractions for a block appearing in $\langle \exp[-S_3(t)] \rangle$ with the same notation as the one in Fig. A.4.

We can also represent the leading contributions to $\langle \exp[-2S_3(t)] \rangle$ by using a block representation . An extra feature in this case compared with $\alpha = 2$ is that there are six possible types of local contraction within a block. We label these a, b, k, and j_i for $i = 1, 2, 3$ (Fig. A.7). The blocks at the top edge of the diagram are fixed to be of type a and b by the structure of traces in $\exp[-S_3(t)]$.

Repeating the approach for $\alpha = 2$, we find that leading diagrams only involve local contractions. Equivalent statements to (i), (ii) and (iii) in Appendix A.5.2 apply. For (i), we find that the leading order odd rows of boundaries have order q^{-2}, and they are of the forms $(ab)_{\text{wall}}$ or $(aj_ib)_{\text{wall}}$. All other odd row configurations $(ad_1d_2d_3 \ldots d_kb)_{\text{wall}}$ are associated with factors smaller than q^{-2}. For $k > 4$, this is trivial because each

wall costs at least $q^{-1/2}$. For $1 \leq k \leq 4$, we enumerate all cases using symbolic computation to complete the proof. Statement (ii) for $\alpha = 3$ is the same as the one for $\alpha = 2$, and (iii) follows trivially for time $t \leq L/4$. An example of a leading order $[O(q^{-4t})]$ diagram is given in Fig. A.9.

The main difference with respect to $\alpha = 2$ is that the leading contributions also include diagrams with regions of j_i-contractions, as well as regions of a- and b-contractions. We classify the leading diagrams at t by the width r of the j_i-region on the bottom row of blocks. To count the number of leading diagrams, we use an inductive approach from time t to $t+1$. Every leading diagram at $t+1$ can be generated from a leading diagram at t by adding four rows of blocks at the bottom of the diagram at t. A newly-added even row must have a configuration identical to the one above. A newly-added odd row has configuration depending on the one above according to the following rules (Fig. A.8). For each even row in which the width of the j_i-region is zero, there are five possible configurations for the odd row below: two with width 0 and three with width 1. For each even row with width $r > 0$, there are four possible configurations for the odd row below, two with width r, one with width $(r-1)$ and one width $(r+1)$. An example of a leading diagram is given in Fig. A.9.

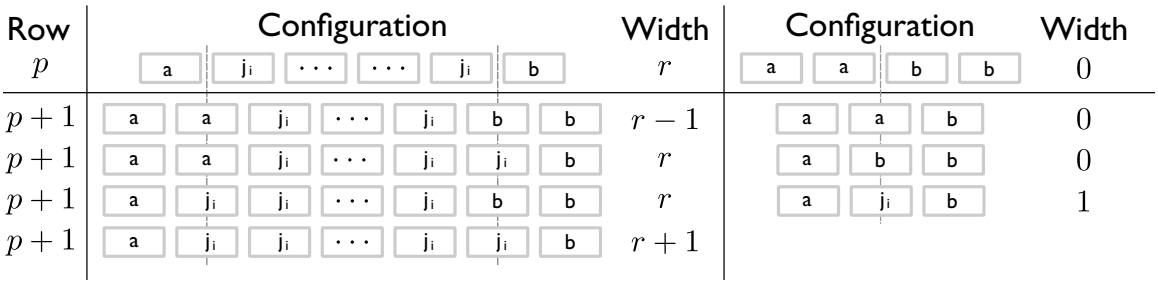


Figure A.8: The recursive rules for enumerating the $p+1$-th row of the leading order diagrams given the p-th row of the leading order diagram. These rules are derived from the fact that, in a leading diagram, the difference between the DW positions at even row p and odd row $p+1$ is exactly one lattice spacing.

We can write this recurrence relation in matrix form, by introducing a vector $\mathbf{v}(p) = (v_0(p), v_1(p), \dots)^T$ where $v_r(p)$ denotes the number of diagrams with total

number of rows p that have a j_i-region of width r in the last row. The degeneracy $D(t)$ can be obtained by summing up the components of $\mathbf{v}(t)$. These in turn can be found by acting $2t$ times with a transfer matrix representing the recursive rules on the vector $\mathbf{v}(t=0) = (1, 0, 0, \dots)^T$.

$$D(t) = \begin{bmatrix} 1 & 1 & \cdots \end{bmatrix} \begin{bmatrix} 2 & 1 & & & \\ 3 & 2 & 1 & & \\ & 1 & 2 & 1 & \\ & & 1 & 2 & \ddots \\ & & & \ddots & \ddots \end{bmatrix}^{2t} \begin{bmatrix} 1 \\ 0 \\ 0 \\ \vdots \end{bmatrix} \sim \left(\frac{4+3\sqrt{2}}{2} \right)^{2t} . \tag{A.7}$$

On the right side of this expression we have used the fact that, for $1 \ll t < L/4$, $D(t)$ is dominated by the largest eigenvalue of the transfer matrix.

For $t > L/4$, there are five leading order diagrams. The first two have ab DW directed only towards the left or the right. The other three diagrams have only j_i-contractions within the light-cone region (dashed lines in Fig. A.9), with the aj_i and j_ib DW-s directed only towards the left and the right respectively After translating these diagrams into algebraic terms, we obtain (2.3) for $\alpha = 3$.

For higher Rényi entropies, we can prove for $\alpha = 4$ that leading diagrams consist of local contractions only, and that $K_4 = \mathrm{Cat}(4)$ in Eq. 2.3. If we assume the analogous statements about local contractions for $\alpha > 4$, we can apply the above approach and show that $K_\alpha = \mathrm{Cat}(\alpha)$ up to $\alpha = 10$.

A.7 Evaluation for OTOC

Here we prove that the OTOC, $\langle \mathrm{tr}[O(x,t)O(y)O(x,t)O(y)] \rangle$, vanishes at large q for $t \geq |x-y|/2$. We employ the analogous block representation introduced in App. A.5.1

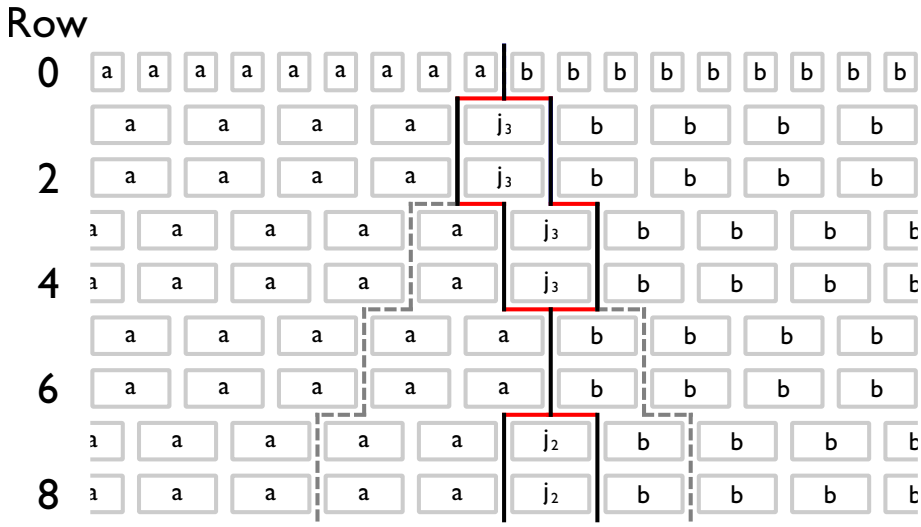


Figure A.9: A leading order DW diagram in the block representation for $\langle \exp[-2S_3(t)] \rangle$ in the large–q limit. The order is given by $q^{-2h_{ab}-h_{aj_i}-h_{j_ib}}$ where $h_{c_1c_2}$ counts the horizontal walls between c_1- and c_2-contractions in red.

of the main text. Using the contraction-addition method described in Appendix A.2, the order of a diagram can be written as in Eq. (A.2) with $\mathcal{O}(G_i^{(0)}) = 1$.

We choose to contract blocks of Us and $U^\dagger$s bond-by-bond from the left to the right in Fig. 2.9 . For the left-most bond, there are always two blocks of filled and empty dots for all $t \geq x/2$. For each of these blocks there are two choices of contraction: A or B. A choice of contraction-A in one of the two blocks can be followed by other contractions in two alternative ways. Either all other blocks within its upward light cone (in this case a stripe of blocks) have A-contractions: this results in a factor $\propto (\mathrm{Tr}\, O)^2 = 0$ at site x, due to contraction-addition of type seven in Fig. A.1. Alternatively there is a q^{-1} cost due to at least one inter-loop contraction-addition of type two, three or six in Fig. A.1. Similarly, the choice of contraction-B would give a vanishing contribution because of the operator in y. These arguments are illustrated in Fig. A.10. So we have shown that all diagrams have an order bounded by q^{-1} for $t \geq |x-y|/2$. By contrast, for $t < |x-y|/2$ all Us and $U^\dagger$s can be cancelled, leaving only $\langle \mathrm{tr}[O(x)^2]\mathrm{tr}[O(x)^2] \rangle = 1$.

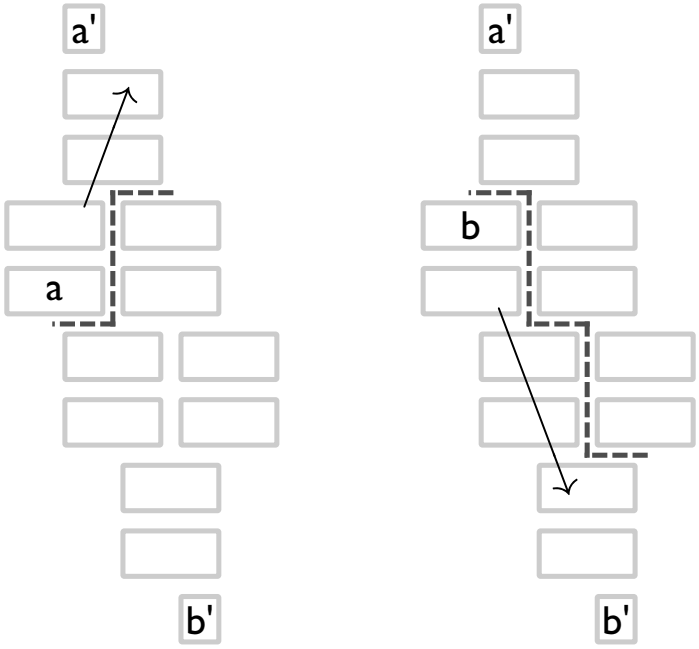


Figure A.10: A partially contracted diagram for the OTOC at $t = 2$ in the block representation. The choice of an A-contraction (or a B-contraction) of blocks on the left-most bond forces blocks in the upper (lower) light cone (dashed lines) to have the same type of contraction. Otherwise, the diagram has an order bounded by q^{-1}.

Appendix B

Appendices of Chapter 3

B.1 Spectral form factor for the Floquet random unitary circuit.

Here we present numerical results for $K(t)$ and $\xi(t)$ in the FRUC defined in Eq. (1.35). We use ED to calculate $K(t)$ and $\xi_L(t) = \log(t)/(L \log K(t))$ for $q = 2$ and $4 \leq L \leq 14$, taking the number of realizations $\mathcal{N} \sim 10^3$. The data for $K(t)$ (Fig. B.1) show a clear deviation from the RMT behaviour for early time. The behaviour of $\xi(t)$ in this model (Fig. B.2) is similar to that for the model discussed in the main text.

B.2 Numerical results for $K(t)$ and $\langle r \rangle$ for the many-body localized phase at $q = 2$

Using ED with $\mathcal{N} \sim 10^5$ realizations, we compute $K(t)$ and $\langle r \rangle$ in Fig. B.5. Both $K(t)$ and $\langle r \rangle$ show a clear deviation from expected RMT forms and suggest that there is only an MBL phase (see Ch. 3 for discussion).

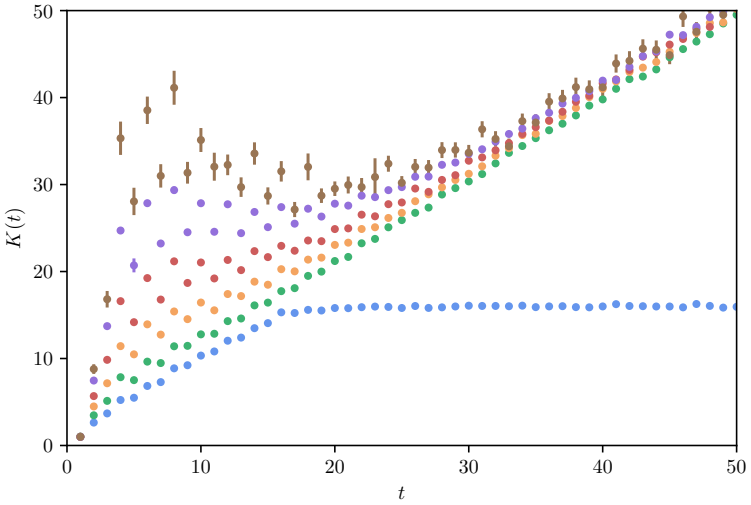


Figure B.1: $K(t)$ at small t, showing deviations from RMT form that grow with L. Data for $L = 4, 6, \ldots, 14$ (from bottom to top).

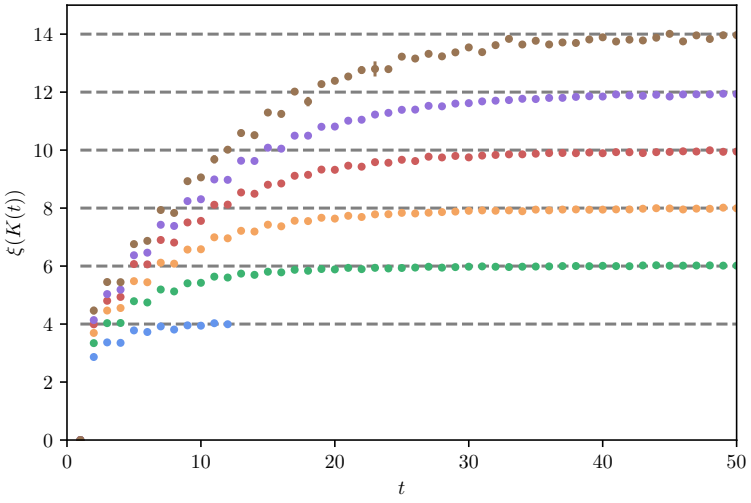


Figure B.2: $\xi_L(t)$ vs t for $L = 4, 6, \ldots, 14$ (from bottom to top).

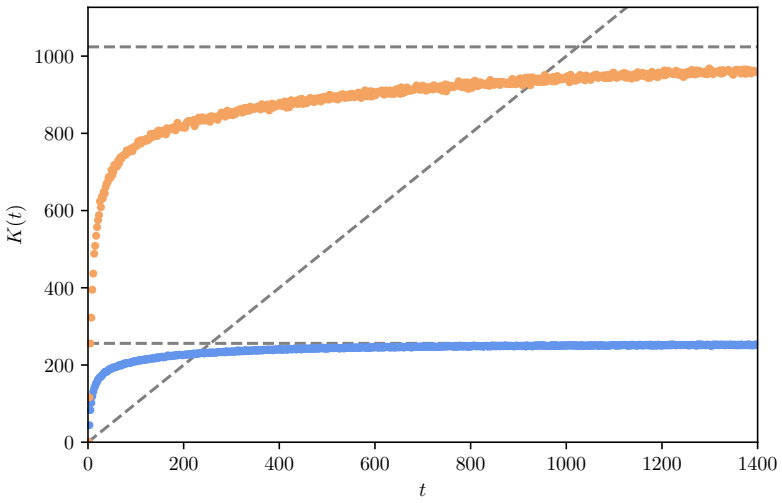


Figure B.3

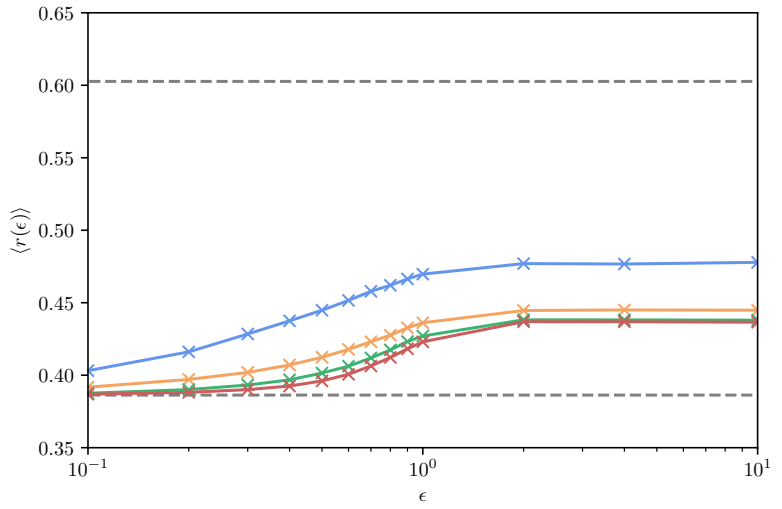


Figure B.4

Figure B.5: On the left, $K(t)$ vs t in the MBL phase for $q = 2$ and $\varepsilon = 1$ for $L = 8$ and 10. On the right, $\langle r\rangle$ vs ε for $q = 2$; $L = 4, 6, 8$ and 10, from top to bottom.

Appendix C

Appendices of Chapter 4

C.1 Computation of $G(\omega_1, \omega_2, \omega_3)$ under the standard hypothesis of ETH for the matrix elements of $\hat{X}$ and $\hat{Y}$

Here we analyse the order of contributions in $G(\omega_1, \omega_2, \omega_3)$ that would be expected if the matrix elements of $\hat{X}$ and $\hat{Y}$ were described by the ETH in Eq. 4.1. Substituting Eq. (4.1) into (4.4) with $\overline{X} = \overline{Y} = 0$, one can introduce the random variable

$$\mathcal{G}(\omega_1, \omega_2, \omega_3) = N^{-3} h(\omega_3) h(\omega_2) h(\omega_1) h(\omega_1 + \omega_2 + \omega_3) \sum_{\alpha\beta\gamma\delta} R^X_{\alpha\beta} R^Y_{\beta\gamma} R^X_{\gamma\delta} R^Y_{\delta\alpha} \delta(\Delta_{\alpha\beta} - \omega_3) \delta(\Delta_{\beta\gamma} - \omega_2) \delta(\Delta_{\gamma\delta} - \omega_1) \quad \text{(C.1)}$$

with $G(\omega_1, \omega_2, \omega_3) \equiv \langle \mathcal{G}(\omega_1, \omega_2, \omega_3) \rangle$. If the matrix elements of $\hat{X}$ and $\hat{Y}$ were independent gaussian random variables, one would have simply

$$\left\langle R^X_{\alpha\beta} R^X_{\gamma\delta} \right\rangle = \delta_{\alpha\delta} \delta_{\beta\gamma} \ , \qquad \left\langle R^Y_{\beta\gamma} R^Y_{\delta\alpha} \right\rangle = \delta_{\alpha\beta} \delta_{\delta\gamma} \quad \text{(C.2)}$$

and hence the average

$$G(\omega_1,\omega_2,\omega_3) \equiv \langle \mathcal{G}(\omega_1,\omega_2,\omega_3)\rangle = N^{-2}[h(0)]^4\delta(\omega_3)\delta(\omega_2)\delta(\omega_1)\ . \tag{C.3}$$

Under this hypothesis, $\mathcal{G}(\omega_1,\omega_2,\omega_3)$ is a random variable, whose behavior is characterised by its fluctuations. Indeed, by considering the $\mathcal{O}(N^4)$ terms in the sum where all indexes are different $\alpha \neq \beta \neq \gamma \neq \beta$ (other contributions are easily seen to be subleading in N), it follows from the central limit theorem that the variance of $\mathcal{G}(\omega_1,\omega_2,\omega_3)$ scales as

$$\mathrm{Var}[\mathcal{G}(\omega_1,\omega_2,\omega_3)] = \mathcal{O}(N^{-2})\,. \tag{C.4}$$

Eqs. (C.3) and (C.4) would imply that $\mathcal{G}(\omega_1,\omega_2,\omega_3)$ vanishes in the thermodynamic limit $N\to\infty$. Consider, however, the sum rule

$$\int_{[-\pi,\pi]^3} \mathrm{d}\omega_1\mathrm{d}\omega_2\mathrm{d}\omega_3\,\mathcal{G}(\omega_1,\omega_2,\omega_3) = N^{-1}\sum_{\alpha,\beta,\gamma,\delta} X_{\alpha\beta}Y_{\beta\gamma}X_{\gamma\delta}Y_{\delta\alpha} = \mathrm{tr}\big(\hat{X}^2\hat{Y}^2\big) = 1 \tag{C.5}$$

This shows that the hypothesis of independence between matrix elements of $\hat{X}$ and $\hat{Y}$ cannot be correct. In particular, $X_{\alpha\beta}Y_{\beta\gamma}X_{\gamma\delta}Y_{\delta\alpha}$ must have a coherent contribution of $\mathcal{O}(N^{-3})$ which, after averaging, dominates the incoherent fluctuation in (C.4). A quantitative determination of this contribution is one of the main results of our work, given in Eq. (4.8) of the main text.

C.2 Factorization of $G(\omega_1,\omega_2,\omega_3)$

As discussed in the main text, the four-point correlator introduced in Eq. (4.4) is related to $g(t_1,t_2,t_3)$ by the Fourier transform

$$G(\omega_1,\omega_2,\omega_3) = \frac{1}{(2\pi)^3}\sum_{t_1,t_2,t_3} e^{\imath(\omega_1 t_1+\omega_2 t_2+\omega_3 t_3)} g(t_1,t_2,t_3) \tag{C.6}$$

where the sum is over the set of integers $(t_1, t_2, t_3) \in \mathbb{Z}^3$. Here, we show that $G(\omega_1, \omega_2, \omega_3)$ can be computed exactly in the limit $\ell \gg v_B t_R$ by replacing $g(t_1, t_2, t_3)$ with the factorised form in Eq. (4.7). We denote the corrections to (4.7) by

$$r(t_1, t_2, t_3) = |g(t_1, t_2, t_3) - g_{\text{approx}}(t_1, t_2, t_3)| \,, \tag{C.7}$$

$$g_{\text{approx}}(t_1, t_2, t_3) = f(t_3 - t_1) f(t_2) k_\ell(\ell/v_B - |t_1|) \,. \tag{C.8}$$

We set $\ell_{12} = \ell - |t_1 - t_2| v_B$ and $\ell_{23} = \ell - |t_3 - t_2| v_B$ and consider the possible regimes.

To estimate $r(t_1, t_2, t_3)$, we discuss operator spreading using the notation of [**?**]. For simplicity, we focus on the $q = 2$ case, the generalisation to higher q being straightforward. We denote Pauli operators acting on site i as $\hat{\sigma}_i^\mu$ with $\mu = 1, 2, 3$ and use $\hat{\sigma}_i^0$ for the identity operator. We introduce Pauli strings as products of single-site Pauli operators $\hat{\mathcal{S}} = \prod_i \hat{\sigma}_i^{\mu_i}$. Then we can expand each Heisenberg operator as

$$\hat{X}(t) = \sum_{\mathcal{S}} c_X^{\mathcal{S}}(t) \hat{\mathcal{S}} \,, \qquad \hat{Y}(t) = \sum_{\mathcal{S}} c_Y^{\mathcal{S}}(t) \hat{\mathcal{S}} \,. \tag{C.9}$$

Note that Pauli strings form an orthonormal basis, since $\text{tr}(\hat{\mathcal{S}}^\dagger \hat{\mathcal{S}}') \equiv q^{-L} \,\text{Tr}(\hat{\mathcal{S}}^\dagger \hat{\mathcal{S}}') = \delta_{\mathcal{S}\mathcal{S}'}$. Because $\text{tr}(X^2) = \text{tr}(Y^2) = 1$, unitarity implies

$$\sum_{\mathcal{S}} |c_X^{\mathcal{S}}(t)|^2 = 1 \,, \qquad \sum_{\mathcal{S}} |c_Y^{\mathcal{S}}(t)|^2 = 1 \,. \tag{C.10}$$

As the total weight of Pauli strings remain normalised, one can interpret their weight as a probability distribution. Two crucial features of a given string are the positions of its left and right ends: the left-most and right-most sites i on which a Pauli operator σ_i^μ with $\mu = 1, 2$ or 3 appears, rather than the identity. We use as guidance results on operator spreading known for random circuits that are stochastic in time. It has been shown [**?**, **?**] at $t \gg t_R$ that nearly all strings contributing to $\hat{X}(t)$ have their left end close to $x - v_B t$ and their right end close to $x + v_B t$. The broadening of the fronts at

$x \pm v_B t$ is diffusive in one dimension [**?**, **?**] and generically sub-ballistic. Between its left and right ends, a typical string has Pauli operators (as opposed to the identity) at a finite fraction of sites. We assume that similar behaviour also applies in spatially extended chaotic systems more generally. Using Eq. (C.9) we have

$$g(t_1, t_2, t_3) = \mathrm{tr}[X(t_3)Y(t_2)X(t_1)Y] = \sum_{\mathcal{S},\mathcal{S}',\mathcal{S}''} c_X^{\mathcal{S}''}(t_3) c_Y^{\mathcal{S}'}(t_2) c_X^{\mathcal{S}}(t_1) \mathrm{tr}(\mathcal{S}''\mathcal{S}'\mathcal{S}Y) \ . \tag{C.11}$$

The average $\mathrm{tr}(\mathcal{S}''\mathcal{S}'\mathcal{S}Y)$ is unity if the product of operators σ_i^μ from the four strings $\mathcal{S}''$, $\mathcal{S}'$, $\mathcal{S}$ and Y gives the identity at every site i; otherwise it is zero.

The typical form of these four strings is shown schematically in Fig. C.1. The dominant contributions to $g(t_1, t_2, t_3)$ arise from sets of strings in which all three of the following conditions are met: (i) the left and right ends of $\mathcal{S}''$ coicide with those of $\mathcal{S}$; (ii) $\mathcal{S}'$ coincides with Y; and (iii) the site y is not situated between the left and right ends of $\mathcal{S}$.

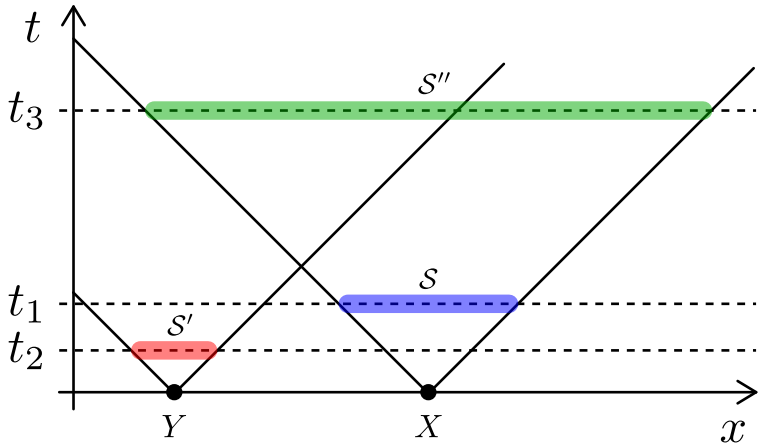


Figure C.1: Sketch of the spreading of operators $X(t_1)$ (blue), $Y(t_2)$ (red) and $X(t_3)$ (green). Most of the weight in the expansion (C.9) is concentrated in strings which have a support growing ballistically with time at the butterfly velocity v_B.

To formalise this approach, we introduce the total weight of Pauli strings laying to the left of site i as

$$R_X(i,t) \equiv \sum_{\mathcal{S} \,|\, \mathrm{RHS}(\mathcal{S}) < i} |c_X^{\mathcal{S}}(t)|^2 \tag{C.12}$$

where RHS($\mathcal{S}$) labels the right end of the Pauli string $\hat{\mathcal{S}}$. The operator $\hat{X}$, initially localised at the site x, spreads ballistically at velocity v_B and one expects at large times [**?**, **?**]

$$R_X(i,t) \sim 1 - \mathcal{C}(\ell = |i-x|, t) = \begin{cases} 0 & i \ll x + v_B t \\ \\ 1 & i \gg x + v_B t \end{cases} . \tag{C.13}$$

with corrections that decrease with the distance $|i - x - v_B t|$ from the front.

We discuss (4.7) in separate steps, according to the values of ℓ_{12} and ℓ_{23}. Consider first $|\ell_{12}|$ and $|\ell_{23}|$ small, and assume for definiteness diffusive front broadening with diffusion constant D. Then we expect deviations from the factorised form (4.7) for $|\ell_{12}| \lesssim O(\sqrt{D\ell/v_B})$ (or $|\ell_{23}| \lesssim O(\sqrt{D\ell/v_B})$), because in this case the ends of strings $\mathcal{S}'$ and $\mathcal{S}$ (or $\mathcal{S}'$ and $\mathcal{S}''$) are close. However, because of relaxation arising from scrambling, $r(t_1, t_2, t_3)$ can be $O(1)$ only if $|t_1 - t_3| \lesssim O(t_R)$ and $t_2 \lesssim O(t_R)$. Upon integration, this gives a contribution from $r(t_1, t_2, t_3)$ of size $O(t_R^2\sqrt{\ell})$ to $G(\omega_1, \omega_2, \omega_3)$, which for large ℓ is parametrically smaller than the contribution described in the main text.

Next we examine the regimes where $|\ell_{12}|$ and $|\ell_{23}|$ are both large and consider the possible cases. When ℓ_{12} and ℓ_{23} are both large and positive, the operators $X(t_1)$ and $Y(t_2)$ in (4.6) commute and the expectation value factorises. We have $g(t_1, t_2, t_3) = g_{\text{approx}}(t_1, t_2, t_3) = f(t_1 - t_3)f(t_2)$ and so $r(t_1, t_2, t_3) = 0$ identically.

In the other cases, it is easy to convince oneself that for a generic system both $g_{\text{approx}}(t_1, t_2, t_3)$ and $g(t_1, t_2, t_3)$ are simultaneously small. To be specific, consider the case when $\ell_{12} > 0$ and $\ell_{23} < 0$, both being large in absolute value. Clearly, $g_{\text{approx}}(t_1, t_2, t_3)$ vanishes for $|t_1 - t_3| \gg t_R$ because of the factor $f(t_3 - t_1)$. To estimate $g(t_1, t_2, t_3)$ we use Eq. (C.11), taking terms in the sum for which $\text{tr}(\mathcal{S}''\mathcal{S}'\mathcal{S}Y) = 1$. Because of (C.13), most of the weight of the operator $X(t_1)$ is concentrated in strings

with support spread throughout the interval $[x - v_B t_1, x + v_B t_1]$. However, in the regime under consideration, $t_3 \gg t_1$, and so non-vanishing contributions to (C.11) come from atypical strings $\mathcal{S}''$ which are anomalously short (see Fig. C.1). More explicitly, we restrict the sum over the strings $\mathcal{S}''$ which overlap with $\mathcal{S}$ and $\mathcal{S}'$

$$\begin{aligned} |g(t_1, t_2, t_3)| &= \left| \sum_{\mathcal{S}, \mathcal{S}'} \sum_{\mathcal{S}'' \text{overlap}} c_X^{\mathcal{S}''}(t_3) c_Y^{\mathcal{S}'}(t_2) c_X^{\mathcal{S}}(t_1) \right| \\ &\leq \left(\sum_{\mathcal{S}'' \, \mathrm{RHS}(\mathcal{S}'') < x + v_B t_1} |c_X^{\mathcal{S}''}(t_3)|^2 \right)^{1/2} \left(\sum_{\mathcal{S}, \mathcal{S}'} |c_X^{\mathcal{S}}(t_1)|^2 |c_Y^{\mathcal{S}'}(t_2)|^2 \right)^{1/2} \\ &= R_X(x + v_B t_1, t_3). \end{aligned}$$

where we used Cauchy-Schwartz inequality and the definition (C.12). So, because of (C.13), $g(t_1, t_2, t_3)$ is small in this regime. The other regimes can be addressed in a similar way.